SAPIENZA
UNIVERSITÀ DI ROMA

SEMICONDUCTOR QUANTUM DOTS FOR PHOTONIC QUANTUM REPEATERS

Facoltà di Scienze Matematiche Fisiche e Naturali
Dipartimento di Fisica
Corso di laurea in Dottorato di Ricerca in Fisica - XXXV Ciclo

Julia Neuwirth
Matricola 1894169

Relatore
Prof. Rinaldo Trotta

Correlatore
Prof. Fabio Sciarrino

Nov. 2019-2022

Abstract

Current information exchange is based on optical fibers and satellite communication via free-space links, where security is provided by mathematical complexity. However, it could potentially be threatened by paradigm shifts in computing technology. Encryption techniques using quantum key distribution based on entangled photons would allow for theoretical full secure communication. The very same platform, entangled photons, can also be employed as a core element to establish multi-node secure communication—a concept known as quantum network. For these reasons, entangled photon sources might be the core of future quantum networks for secure communication.

In this thesis, I study GaAs/AlGaAs quantum dots as entangled photon sources. After giving a general overview on the fundamentals of photonic quantum networks and GaAs droplet-etched quantum dots, I mainly focus on two aspects of the development of this technology. First, limits of the source performance as entangled photon sources and second, applications of entangled photons from quantum dots for secure communication. The prior includes degrading effects of entanglement in these quantum dots, especially based on multiphoton emission and optical Stark effect induced by the particular entangled-photon generation technique, resonant two-photon excitation. The experimental results demonstrate that multiphoton emission is negligible under practical conditions, which is supported by a probabilistic model. The finite excitation laser pulse duration in resonant two-photon excitation, on the other hand, induces an optical Stark effect. The measurements in this thesis support the theoretical predictions and an entanglement reduction by increasing excitation laser pulse length is observed experimentally. If some conditions are met, GaAs/AlGaAs quantum dots emit highly entangled photons, which are utilized in the second part of this thesis by applying them in entanglement-based quantum key distribution protocols. The demonstrations range from the first implementation of quantum dots as entangled photon sources for secure communication in fiber and free-space, to a continuous secret key exchange over three days. The second test case, in particular, tackles the challenges of real-life applications such as sunlight and mild rain. At the end, I provide a brief outlook on how to use entangled photons from GaAs/AlGaAs quantum dots to transfer information from one node of a network, namely a quantum repeater, to another by proposing an experiment called remote quantum teleportation.

Keywords: semiconductor quantum dots, entangled photons, quantum key distribution, quantum repeater, quantum networks

Contents

List of Figures

List of Tables

List of Acronyms

APD	Avalanche Photo Diode
BS	Beam Splitter
BSM	Bell State Measurement
DBR	Distributed Bragg reflector
FSS	Fine Structure Splitting
HBT	Hanburry Brown and Twiss
HOM	Hong-Ou-Mandel
LDE	Local Droplet Etching
NF	Notch Filter
OTP	One-Time-Pad
PBS	Polarizing Beam Splitter
QBER	Quantum Bit Error Rate
QD	Semiconductor Quantum Dot
QKD	Quantum Key Distribution
QUBIT	Quantum Bit
SPDC	Spontaneous Parametric Down Conversion
TPE	Two-Photon Excitation
VBG	Volume Bragg Grating
X	Exciton
XX	Biexciton

Chapter 1

Introduction

Modern information exchange based on optical communication is fundamental in present society, ranging from financial, or medical data to information related to critical infrastructures. Current security standards rely on the computational complexity of one-way functions [1], which, for example, are based on prime factorization of large numbers, as the Rivest-Shamir-Adleman (RSA) scheme. This mathematical problem, however, could be solved efficiently by future quantum computers using Shor´s algorithm, which drastically reduces the computation time [2]. For this reason, intrinsically secure encryption techniques that are based on quantum mechanics and exchange a cryptographic key, as *Quantum Key Distribution (QKD)*, are investigated. *QKD* is a method of establishing a random bit string, securely shared between authenticated parties, which is then applied to encrypt the message. When a *One-time-pad (OTP)* scheme is applied for data encryption, full theoretical security is possible [3, 4], because, compared to the classical analogy, which is protected by computational complexity, *QKD* is protected by the laws of quantum mechanics. In a nutshell, instead of establishing a cryptographic key of classical bits, the key is shared via *Quantum Bits (qubits)*. Any attempt to gain information on the cryptographic key requires measuring the *qubits*, which introduces errors into the key [5]. Thus, the communicating parties detect any eavesdropper already during key generation and can discard the corresponding bit string from the key. This approach promises stronger security by protecting data against eavesdropping.

Qubits are possible in many physical realizations, such as electrons [6, 7] or microwave photons [8]. But the most obvious technology platform for communication is based on optical photons. Photons move fast, they hardly interact with their environment, which leads to unmatched coherence properties [9], and provide the possibility to encode information in various degrees of freedom, for example, polarization, time-bin, energy, path, phase, or orbital angular momentum [10]. Additionally, by using optical photons we can exploit the already vastly developed communication systems based on optical fibers and satellites.
The bottleneck for long-distance communication is the scaling of the error probability with the length of the channel that connects transmitter and receiver. In optical fibers, for example, the probability for photon absorption and depolarization grows exponentially with the length of the fiber [11]. The detrimental effect can be even more severe for properties such as entanglement [12]. Therefore, a number of trials, which grows exponentially with distance, for a successful transmis-

sion is needed. In classical communication, these problems are solved using signal repeaters along the channel, which amplify the signal and restore it to its original shape and intensity. This is more complex for quantum signals (*qubits*). The no-cloning theorem [5] prohibits to get an independent and identical copy of an arbitrary unknown quantum state. Consequently, alternative restoring methods for *qubits* are needed for long-distance communication. At best this method is both, compatible with *QKD* protocols and a potential building block for quantum networks. The idea of quantum repeaters was born. A quantum repeater is a technology that enables the distribution of quantum signal among distant and uncorrelated nodes without suffering from unbearable signal losses. It relies on entanglement resources, projective measurements and, arguably [13–15], quantum memories.

The entanglement resource should provide two photons, which are entangled with each other. Entanglement is the existence of a non-classical non-local correlation in a degree of freedom between two objects. For example, entangled photons in polarization share a non-local correlation in their polarization state. This means, knowing the polarization of one photon of an entangled photon pair discloses the polarization of the second photon. These entanglement resources are then placed on nodes of the network, sending one photon of the entangled photon pair to one receiver and sending the second photon of the entangled photon pair to another receiver. When placing the node between the two receiving parties, this allows to double the distance between the communicating parties. Instead of receivers we can again place nodes, which have their own entanglement resource. This concept would allow to build a network of individual nodes. These nodes can be linked by transferring the entanglement from the first node to the second node, using an operation known as entanglement swapping [16]. One photon from each entangled-photon pair is used to implement a projective measurement via photodetectors. This operation projects the entanglement onto the remaining two photons, which have never interacted before. Using this technique and assuming all steps, entangled photon generation and entanglement swapping to be perfect (100 % efficient), theoretically, entanglement between photons can be passed on to any point in the network without compromising the advantage of using a quantum signal. But, this strategy does not increase the transmission probability of the photons through the whole network. The photon losses still scale exponentially with the passed distance, as would be the case of no nodes and one photon traveling the same distance. Adding quantum memories to the quantum repeater allows to store the entanglement in one node and time its distribution. For example, in case a swapping operation failed on one node, the other node stores the entanglement until entanglement swapping is restored in the adjacent node. The quantum memories would allow for a communication time that grows polynomial instead of exponential with transmission distance [17].

This simple concept of nodes with entanglement resources, projective measurements and quantum memories would allow to build up a quantum network. More precisely this framework would allow to share a *qubit* over arbitrary distances by keeping its quantum nature. Furthermore, this concept of sharing entangled *qubits* is also compatible with entanglement-based *QKD* protocols. Combining these two concept would enable to share a cryptographic key over arbitrary distances.

In order to make the technology advantageous high demands are posed on the basic hardware

blocks. The core of the hardware block is an entanglement resource with the following requirements: a high entangled photon pair emission efficiency (preferably on demand), with a very high degree of entanglement and for the projective measurements a high photon indistinguishability [18]. The state-of-the-art entangled photon pair source for photon-based entanglement experiments are sources based on parametric down conversion [19]. These sources provide nearly maximally entangled photons, but with a non-zero probability of emitting more than one entangled photon-pair per excitation pulse [20]. Consequently, when raising the number of entangled photons, increasing the brightness of the source, also the multipair emission probability increases [21]. This limits the technological potential of these sources, it reduces the achievable cryptographic key rate in *QKD* [22, 23] and introduces errors in the projective measurements [24]. For these reasons, alternative entanglement resources have been investigated in the last two decades. Solid-state-based quantum emitters, for example, generate nearly on demand [25] entangled photons in polarization via the biexciton-exciton cascade [26], with a high degree of entanglement, an extremely low multiphoton emission probability [27, 28] and photon indistinguishabilty [29, 30]. Hence, *Semiconductor Quantum Dots (QDs)* provide all the desired characteristics for the application. Additionally, wavelength-tunability makes them easily interfaced with other sources [31], as well as the first preliminary experiments have demonstrated the potential to interface *QDs* with quantum memories [32]. These features hold great promise for the construction of solid-state-based quantum networks ensuring cryptographic key exchange by entanglement distribution.

Over the last couple of years, these advantageous features have been exploited to demonstrate the feasibility of *QDs* as the hardware of quantum networks. Experiments on quantum teleportation, which means transferring a quantum state onto one photon of an entangled photon pair even at distance, demonstrates the applicability of *QDs* as potential entanglement resources for quantum repeaters [33]. This scheme is even applicable with non-perfect entangled photons [34]. This was extended by the demonstration of entanglement swapping, the procedure needed for quantum repeater operation [35]. However, there is still a lot to understand. Entanglement in as-grown *QDs* can reliably achieve values above 90 % [36], up to a current record value of 97 % [37] in terms of fidelity to a perfectly correlated photon pair. But entanglement degrading effects are still not fully probed. Hence, entanglement generation, evaluation and improvement techniques still need to be investigated and new, improved sources need to be developed. Even though a lot of pioneering work for quantum repeater concepts have been performed using *QDs*, up to now the works never exceeded proof-of-principles, especially not involving multiple sources. One research path, which has not been explored closely is using *QDs* as sources for *QKD* protocols. Relatively few *QKD* protocols based on *QDs* have been performed, especially on entangled photons and in outside-the-lab conditions.

In this thesis, I discuss one potential source of entangled photons, namely GaAs/AlGaAs *QDs*, their strengths and weaknesses for the application as entangled photon sources in quantum communication. This includes an in-depth study on entanglement degrading effects in *QDs*, focusing on multipair emission. Additionally, I briefly address other potential entanglement degrading effects

based on entanglement generation techniques in *QDs*. I also demonstrate the first implementation in fiber and free-space entanglement-based *QKD* in an out-of-the-lab scenario. This is extended to a free-space optical communication for three days straight, demonstrating the potential for real-world applications. Finally, the thesis concludes with a summary and an elaborate outlook on the road ahead. I discuss potential next steps going from two communicating parties towards the establishment of a quantum network.

This thesis is structured in the following way:
Chapter two discusses the background of quantum networks, based on solid-state quantum emitters. Special attention is given to *QKD* and quantum repeaters with their basic principles. The next chapter, chapter three, introduces entangled photon generation using *QDs*. It begins by answering the questions what are *QDs* and how to model them, and finishes with the discussion on how entanglement generation is applicable in these nanostructures. Chapter four summarizes the most common measurement techniques used in this thesis. Chapter five focuses on the entanglement degrading effects that limit GaAs/AlGaAs *QDs* to the currently non-perfect entanglement. The next chapter, chapter six, discusses the results obtained for *QKD* based on *QDs*. The last chapter, chapter seven, summarizes the work conducted in this thesis and provides an outlook on the challenges ahead to go towards quantum repeaters and to improve the figures of merit of the source to make them suitable in terms of efficiency for applications outside of the laboratory.

Chapter 2

Fundamentals of photonic quantum networks

Current classical communication decyphers messages based on public-key cryptography protocols. Attacks, as man-in-the-middle attacks, where the attacker has secretly inserted themselves between the two communicating parties, listens and possibly alters the communication, are currently prevented by authentication certificates issued by trusted certificate authorities.

Other attacks, as brute force attacks, where the attacker tries to crack the password by random trials, are currently prevented by very long computation times to crack strong passwords or long encryption keys, which exploit the difficulty of prime number factorization. However, Shor´s algorithm states that the advantage of prime number factorization will vanish with the computational advantage of quantum computers [2]. For this reason, new cryptography schemes are developed, moving from secure keys generated from single binary bits, 0 or 1, to *Quantum Bits (qubits). Qubits* rely on the rules of quantum mechanics and are represented by their wave function $|\psi\rangle$ in a complex Hilbert space. As a result, the *qubit* could be in both states, logical 0 or logical 1, at the same time. This extends the limited calculation method of binary operations to the superposition of states [38]. The superposition of both states, $|0\rangle$ and $|1\rangle$, of the *qubit*, $|\psi\rangle$, can be expressed in the Dirac notation as following:

$$|\psi\rangle = \alpha\,|0\rangle + \beta\,|1\rangle = \begin{pmatrix} \alpha \\ \beta \end{pmatrix} \tag{2.1}$$

with α and β, the amplitude complex coefficients, constrained by the normalization condition $|\alpha|^2 + |\beta|^2 = 1$. A measurement on the *qubit* projects $|\Psi\rangle$ on the measurement basis $|0\rangle$ and $|1\rangle$ with the probability of $|\alpha|^2$ and $|\beta|^2$. Visualization of the *qubit* state is given by the *Bloch sphere* (see Figure 2.1). For this, we re-write the *qubit* as a *Bloch vector*, defined as:

$$|\psi\rangle = \cos\frac{\theta}{2}\,|0\rangle + e^{i\phi}\sin\frac{\theta}{2}\,|1\rangle = \begin{pmatrix} \cos\frac{\theta}{2} \\ e^{i\phi}\sin\frac{\theta}{2} \end{pmatrix}, (0 \leq \theta \leq \pi, 0 \leq \phi \leq 2\pi) \tag{2.2}$$

When the *qubit* is in state $|0\rangle$ or $|1\rangle$, it corresponds to the North pole ($\theta = 0$) or South pole ($\theta = \pi$) of the sphere. All other values of θ correspond to superimposed states.

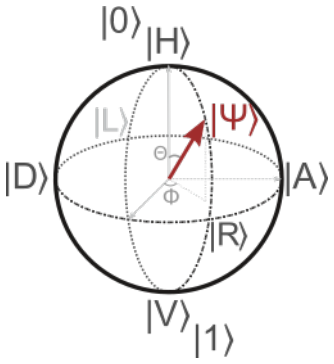

Figure 2.1. Bloch sphere representation of a *qubit*.

When measuring single *qubits*, as defined in Eq. (2.1), the wavefunction collapses and the state will be projected on one of the measurement outcome states with the given probability. But, until the *qubit* is measured, the exact state of the *qubit* is uncertain. This uncertainty of the exact state of the *qubit* can be exploited to encrypt messages using prepare-and-measure *QKD* protocols. Details to the protocol structure are explained in Section 2.1.1. In contrary to the prepare-and-measure *QKD*-protocol family are entanglement-based *QKD* protocols. There, two *qubits*, which are entangled with each other, are exploited to establish an encrypted key. Entanglement between *qubits* is achieved by extending the concept of single *qubit* to composite *qubit* systems, put together by multiple *qubits*. The composite system is constructed by the tensor product of the state-spaces of the individual components. Considering N *qubit*-systems, each prepared in the state $|\psi_i\rangle$, then the total state is $|\psi_1\rangle \otimes |\psi_2\rangle \otimes ... \otimes |\psi_N\rangle$, which spans the 2^N Hilbert space. If we, for example, look at the two-*qubit* Hilbert space, constructed by a the tensor product of the two Hilbert spaces of *qubit* A and *qubit* B, the two-*qubit* state can be written as:

$$\begin{aligned} |\psi\rangle &= \alpha_{0,0} |0\rangle_A \otimes |0\rangle_B + \alpha_{0,1} |0\rangle_A \otimes |1\rangle_B + \alpha_{1,0} |1\rangle_A \otimes |0\rangle_B + \alpha_{1,1} |1\rangle_A \otimes |1\rangle_B \\ &= \alpha_{00} |00\rangle + \alpha_{01} |01\rangle + \alpha_{10} |10\rangle + \alpha_{11} |11\rangle = \begin{pmatrix} \alpha_{00} \\ \alpha_{01} \\ \alpha_{10} \\ \alpha_{11} \end{pmatrix} \end{aligned} \tag{2.3}$$

and re-written in the last line using the shorthand notation $|ij\rangle = |i\rangle_A \otimes |j\rangle_B$ for the bases of this 2^2-dimensional Hilbert space. The superposition of states gives access to new fundamental concepts, as *entanglement*. *Entangled states*, in opposition to *separable states*, cannot be factorized in the tensor product of their individual components. The *Bell states* represent the simplest form of quantum entanglement, the maximally entangled (non-separable) quantum states of two *qubits*.

$$
\begin{aligned}
|\phi^+\rangle &= \frac{1}{\sqrt{2}}(|00\rangle + |11\rangle) \\
|\phi^-\rangle &= \frac{1}{\sqrt{2}}(|00\rangle - |11\rangle) \\
|\psi^+\rangle &= \frac{1}{\sqrt{2}}(|01\rangle + |10\rangle) \\
|\psi^-\rangle &= \frac{1}{\sqrt{2}}(|01\rangle - |10\rangle)
\end{aligned}
\tag{2.4}
$$

The Bell states are in a superposition of 0 and 1, in a linear combination of the two states. This has the result that, when measuring one of the two *qubits* and knowing the random outcome of this measurement, the state of the second *qubit* is certain. When this condition holds true regardless of the measurement basis, the two *qubits* are denoted as maximally entangled. This correlation between the two qubits for any analyzed basis is exploited in entanglement-based cryptography. If, for example, an eavesdropper intercepts the communication the wavefunction of the quantum state collapses and, depending on the chosen measurement basis of the eavesdropper, the expected quantum state on the other side is altered. Hence, the communicating parties can detect the presence of an eavesdropper.

The more general description of a *qubit* or a composited *qubit*-system needs the extension from pure states, Eq. (2.1) and (2.4), to mixed states, which are formalized in terms of density matrices. This is discussed in Section 4.4.

Qubits have been demonstrated in various platforms, such as electronic states of atoms [39], nuclear [40] or electronic [41, 42] spins, flux or phase [43] states in superconducting materials, and photons [10]. Entangled states can either be generated by interaction of quantum states [18] or through non-linear parametric processes [19]. For quantum communication, photons are the optimal choice. Photons do not only take advantage of the current well-established fiber and free space communication infrastructure, they are also robust against decoherence due to weak interaction with the environment. Therefore, photons provide an easy implementation in the current infrastructure as well as less losses in the transferred information. Additionally, photons provide various degrees of freedoms to encode information, for example, Fock states (number of particles) [44], time-bin [45], orbital-angular momentum [46] and polarization [47]. This work focuses on an efficient source of polarized photons. Hence, the *qubit* is the polarization degree of freedom of a single photon.

In the following discussion, we define the $|0\rangle$ *qubit* as horizontally linearly polarized photon and $|1\rangle$ *qubit* as a vertically polarized photon. Additionally, we choose an entangled photon pair, in the $|\psi^+\rangle$ state. These single- or entangled-photons can now be exploited for intrinsically secure encryption schemes using QKD.

2.1 Quantum key distribution

QKD is an encryption key technology that, in theory, provides unconditionally secure communication based on the laws of quantum mechanics. Instead of generating a secret key between two entities (Alice and Bob) using classical bits, the secret key in *QKD* is encoded in *qubits*. If now an eavesdropper is trying to intercept the conversation, Alice and Bob detect its presence. Imagine the following scenario: Alice prepares a *qubit* in a randomly selected basis out of two non-commutating sets of bases. The *qubit* is then sent to Bob, who measures the *qubit* randomly also in one of the two non-commutating bases. If an eavesdropper wants to get information on the encryption key, it has to perform measurements on the *qubits* sent to Bob. For this the eavesdropper chooses a measurement basis, produces a state based on its measurement result and then sends this state to Bob. Bob, when performing his measurement, chooses randomly out of the non-commutating bases. The eavesdropper, however, is not able to predict the choice of Bob's basis and consequently cannot faithfully reproduce the result that Bob would have read without the intercept. Therefore, Alice and Bob can detect for eavesdropping by comparing part of their bit strings and checking if they have larger discrepancies than expected. Consequently, *QKD* protocols prove to be robust against attacks, even with unlimited computational power.

Numerous QKD protocols are developed depending on the QKD platform, i.e., decoy protocols for attenuated lasers, multidimensional protocols, fully and partially device-independent protocols and so on [48]. However, I am interested in discrete variable protocols, which are categorized in two types of *QKD* protocol families, prepare-and-measure-based and entanglement-based *QKD* protocols. In the following section we will quickly introduce the two concepts, but later focus on entanglement-based protocols.

2.1.1 Prepare-and-measure quantum key distribution

The first *QKD* protocol was proposed in 1984 by Bennett and Brassard [49], which falls under the category of prepare-and-measure *QKD* protocols. This protocol family, as the BB84 protocol, use single *qubits* to establish the encryption key. The sender (Alice) has a single *qubit* source, which generates single *qubits* with a certain rate. Every *qubit* is then prepared randomly in a particular quantum state out of a set of non-commutating bases. For example, Alice randomly prepares a photon with specific polarization (H) out of the basis sets $\{H, V\}$ and $\{D, A\}$. Since these two bases sets are non-commutating (not mutually orthogonal), it is impossible to distinguish among all of these states with certainty with a single-shot measurement. The *qubit* is then sent to the receiver (Bob). The receiver measures the photon in the same basis sets, but chooses the measurement basis randomly. After transmission of multiple *qubits* Alice and Bob communicate in a public authenticated, classical channel their bases used for preparation and measurement. If the preparation and measurement bases do not coincide, Alice and Bob discard the measured bits. In the other case, Alice and Bob keep the measurement result in a bit string. Alice randomly discloses a certain fraction of the bit string and communicates it to Bob. Both, Alice and Bob announce the bits (measurement results) for the selected fraction in the public channel and check

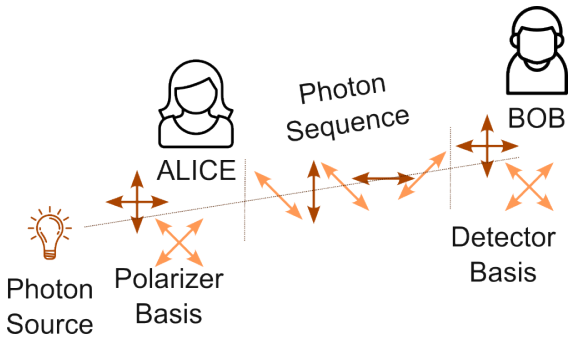

Figure 2.2. Prepare-and-measure based *QKD*: Alice prepares randomly each *qubit* in a specific state, i.e., a set of polarization basis. Bob measures the *qubit* in a predefined set of bases. The measurement basis are shared via a public channel and when Alice and Bob prepared and measured the same basis, the measurement result is added to the key. A randomly chosen portion of the key is compared between Alice and Bob, checking whether a certain number of bits coincide. If this is the case, Alice and Bob share an encryption key, the remaining unshared key.

whether a certain number of these measurements match. If this check passes, Alice and Bob share an encryption key, the remaining bit string, which has not been disclosed during the check. In case an eavesdropper, Eve, infiltrated their communication, the best choice she has is measuring the *qubit* and generating a state that has the result of its measurement. This state is then sent to Bob, which again randomly measures the state generated by the eavesdropper. However, since Eve does not know for certain which measurement basis Bob will choose, she has a 50 % chance to have guessed wrong. In this case, the result of Bob's measurement has a 50 % chance of differing from Alice's basis selection. Hence, the eavesdropper has the risk disturbing a particular *qubit* with a probability of 25 %. This is then detectable by Alice and Bob as a higher uncertainty when matching results in the compared bits. In case an eavesdropper infiltrated their communication, Alice and Bob would delete the established key and start generating a new encryption key.
The second protocol family based on entanglement, on the other hand, does not share single *qubits* via the quantum channel, but share two *qubits*, which are entangled with each other.

2.1.2 Entanglement-based quantum key distribution

Entanglement-based *QKD* protocols, as the name indicates, rely on entangled *qubits*, instead of single *qubits*. Using an entanglement-based protocol instead of a prepare-and-measure scheme, the achievable raw key rate is in principle the same. However, the achievable distance can be doubled, since one can simply place the entangled photon source between the communicating parties. Thus, an entangled *qubit* source, which emits, i.e., polarization-entangled photons, is put in the middle between the two communicating parties, Alice and Bob. One *qubit* is sent to and analyzed in a randomly-selected basis by Alice. The second *qubit*, which is entangled to the other qubit, is sent to Bob and also analyzed in a randomly-selected basis. In case an eavesdropper measures one of the two *qubits*, the entanglement between them is destroyed. Alice and Bob, as in the prepare-and-measure protocol, again share the measurement basis over a public channel. If the same measurement bases were chosen by Alice and Bob, they use the outcome as a new bit in the encryption key, since it is certain that it will be the same due to entanglement. In case they chose

different measurement bases, they communicate the measurement outcome and check if the result is plausible conditioned by the entanglement of the *qubits*. The exact implementation is dependent on the specific protocol choice.

Ekert 91 protocol

In 1991, Ekert developed a *QKD* protocol that exploits the completeness of quantum mechanics using entangled pairs of photons [50]. The scheme is based on Bohm's version of the Einstein-Podolsky-Rosen gedanken experiment [51] and tests for eavesdropping with the generalized Bell theorem (Clauser-Horne-Shimony-Holt inequalities) [52, 53].
The quantum channel consists of a source that emits pairs of *qubits*, for example polarization entangled photons, in the Bell state ϕ^+. The two *qubits* fly apart in the z axis, towards the two users of the channel, Alice and Bob. Both, independently perform measurements on the polarization components along one of the three directions given by the unit vectors a_1 and b_j $(i, j = 1, 2, 3)$ of the *qubits*. In terms of polarization basis, this would correspond to $\{a_1, a_2, a_3\} = \{0°/90°, -22.5°/67.5°, -45°/45°\}$ and $\{b_1, b_2, b_3\} = \{-22.5°/67.5°, -45°/45°, -67.5°/22.5°\}$, where the angles are with respect to H polarization. The orientation of the analyzers are chosen randomly and independent for each pair of incoming *qubits*. The result of each measurement, in $\hbar$ units for the polarization basis is either, +1 (L) or -1 (R) (equivalent for the other basis), and can potentially reveal one bit of information. To test the success of the protocol we have to perform a test of local realism. Locality means that an object is only influenced by its immediate surrounding. Since Alice and Bob are placed far apart, locality would predict that the measurement performed by Alice does not instantly influence the measurement performed by Bob and vice versa. Realism means that the outcome of the measurement follows deterministically from preexisting properties of the particle. Local realism, or its negation, can be determined through the Bell parameter. The Bell parameter S, as defined by Clauser, Horne, Shimony and Holt [53] is defined from the correlation coefficients between Alice and Bob:

$$S = E(a_1, b_1) - E(a_1, b_3) + E(a_3, b_1) + E(a_3, b_3) \tag{2.5}$$

with E, the correlation coefficient on spin components along one of the three directions given by the unit vectors a_i, b_j $(i, j = 1, 2, 3)$, for Alice (a) and Bob (b), respectively. The correlation coefficient depends on the probability $(P_{\pm\pm}(a_i, b_j))$, which are ± 1 for the measurements on a_i and b_j:

$$E(a_i, b_j) = P_{++}(a_i, b_j) + P_{--}(a_i, b_j) - P_{+-}(a_i, b_j) - P_{-+}(a_i, b_j) \tag{2.6}$$

Quantum mechanics predicts for a maximally entangled state

$$S = -2\sqrt{2} \tag{2.7}$$

After the transmission of the *qubits*, Alice and Bob announce in the public channel the analyzing basis that they have chosen for each particular measurement. All the measurements in which either

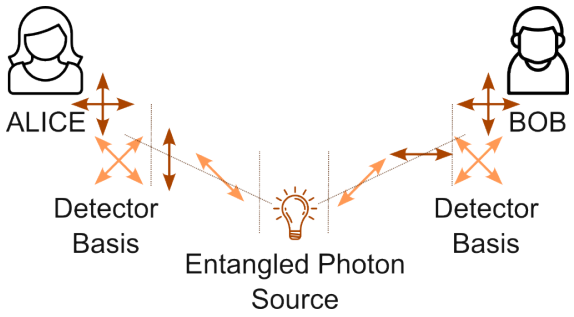

Figure 2.3. Entanglement-based *QKD*: An entangled photon source sends one *qubit* to Alice, the second *qubit*, entangled to the first, to Bob. Alice and Bob measure the received *qubit* and share the measurement basis via a classical channel. When both measured the key basis of the entangled photon pair, the measurement result is added to the raw key. Otherwise the measurement result is communicated via a classical channel and the security of the key is verified checking the Bell parameter.

or both of them failed to register a particle are discarded. When they measured different bases, the measurement results are shared via a public channel and the value S can be retrieved. If the *qubits* were not directly or indirectly disturbed, the result of Eq. (2.7) should be reproduced. However, experimental imperfections and non-perfect entanglement lower the value S. To experimentally demonstrate that the signal violates local realism, it is enough that the Bell parameter surpasses a given threshold. Hence, we test that the source negates the classical signal limit of the Bell parameter, which is:

$$S \leq 2 \tag{2.8}$$

When the measured Bell parameter is above 2, Alice and Bob are assured that they obtained anti-correlated results, when they chose the same measurement basis, as quantum mechanics predicts. Now, Alice and Bob can convert the measurement outcome for the same measurement bases into a secret string of bits - the key [50].
If an eavesdropper is present it would for example, measure part of the *qubits* and may try to substitute his own prepared data for Alice and Bob to misguide them. However, the eavesdropper does not know the orientation of the analyzers, the analyzing basis, for the particular *qubit* pairs, because they are chosen randomly. Hence, the eavesdropper introduces elements of physical reality to the measurements of the spin components and results in being detected [50]. Ekert could demonstrate that the generalized Bell´s theorem has a practical application in cryptography and can be used to test the safety of the key distribution.

2.1.3 Post processing

So far, I have considered ideal protocols. In reality, however, errors in the transmission are unavoidable, which need to be processed in order to obtain a common secret shared key. This is an essential part of any *QKD* protocol to ensure its success.

Qubit exchange: First, as described before, the single- or entangled-*qubits* are shared between Alice and Bob. The measurement results in the key basis build the so called raw key.

Sifting of the key: Different transmission and detection efficiencies introduce unequal losses for Alice's and Bob's measurement channels. Consequently, Alice and Bob might not have measurement results for each sent *qubit*-pair. For this reason the raw key on both sides needs to be re-organized. Alice and Bob communicate in a public channel the measured bases and reduce the raw key by only considering measurements where both have a measurement result on the same basis. This step is referred to as key sifting. After this step, both, Alice and Bob, in the absence of errors, share a secret key, the sifted key, which has the same length on both sides and correspond to the same entangled *qubit*-pairs. During sifting no important bit information is revealed to a possible eavesdropper, because only information on the bases is exchanged.

Error estimation and correction: In the next step it is necessary to check if an eavesdropper was listening to the communication. This step is referred to as error estimation. Alice and Bob can, for example, estimate the error by disclosing part of the acquired raw key and guess the total error on the key based on the partial statistic taken. Eavesdropping is not solely responsible for errors in the quantum channels. Errors may also occur due to imperfections in the state preparation, a polarization reference frame misalignment, an imperfect measurement apparatus (polarizing beam splitters, detector dark counts, background stray light) [54]. All of these factors might result that the bits measured by Alice and Bob differ even though they use the same measurement basis. This error or the key is quantified by the *Quantum Bit Error Rate (QBER)*, the fraction of differing bits. Depending on the protocol a certain bit error rate is tolerated, for example 11 % for the protocol used in this thesis [3, 55]. This boundary of 11 % ensures that random errors can be corrected for. If the error is bellow the protocol limit, the sifted key is processed further and compensated by an error correction step. The error correction aims to transform an error-afflicted sifted key into an error-free key. Many error correction schemes can be applied, one of the simplest approaches to implement is based on public bit block comparison [54]. The algorithm is set up to reduce the error on the sifted key round-by-round while disclosing the minimum amount of information. However, when publicly sharing information, for example the parity of a bit block, the eavesdropper gains some information on the error corrected key. This has to be considered in the next step, the privacy amplification.

Privacy amplification: The last step is a specific post processing on the error corrected key that Alice and Bob have agreed on beforehand. Alice and Bob apply a pre-defined mathematical function, the so-called hash function [56]. The hash function reduces the error corrected key by considering the amount of information the eavesdropper possesses, which is estimated on the basis of an experimental parameter, such as the error rate or the Bell parameter depending on the protocol. As a consequence the eavesdroppers has less knowledge on the error corrected key, in best case only a negligible amount. This will be discussed in more detail in Section 6.4.3. The length of the final secret key should also keep into account possible shortcomings between the protocol assumptions and its implementations, for example due to the photon splitting attack against states which have no true single-photon statistics. The remaining bits form now the secure key, which is used for encryption.

Using this procedure, a secure key is established between the two communicating parties. However, to ensure full security on the encrypted message, the *OTP* encryption method has to be applied on the message [57]. The *OTP* relies on the strategy that the secure key shared between Alice and Bob is secret and randomly generated. Additionally, the *OTP* requires that the secure key is as long as the massage to be encrypted and is only applied once [58].

If these requirements on the secure key and the usage hold, it can simply be applied to the message using an exclusive OR operation. Consequently, Alice and Bob can send the encrypted message via a public channel and the receiving party can decipher the massage applying again an exclusive OR operation on the message. Since the secure key seems random to third parties, and any repetitions of the key are excluded using the *OTP*, no useful information is shared to any adversary.

2.2 Quantum repeater

The *QKD* protocols establish a secure key between two communicating parties. However, as it can be imagined, when the two are parted by long distances, new challenges arise. When sending photons over long distances, they interact with the transmission medium and hence, lose their coherence or just simply get absorbed. Fibers, which currently are the basis for our long distance communication, scale the transmittance T exponentially with the fiber-length L, with a minimum attenuation of $\alpha = 0.16\ dBkm^{-1}$ (ultra low-loss fibers at 1550 nm wavelength) [59]. This results in the probability that both photons from an entanglement-based *QKD* protocol arrive at destination, of $P \sim T_1 \cdot T_2 = e^{-\alpha L_1 - \alpha L_2} = e^{-\alpha(L_1+L_2)}$, leading to a signal attenuation of ca. 50 % after 20 km travel distance. For this reason, when messages are transferred over long distances in our current classical communication channels, signal repeaters are placed along the channel to restore the shape and intensity of the wave traveling through the communication channel. If we now, however, send a quantum signal (*qubit*) from one distant location to another, we cannot just amplify the *qubit* to restore its coherence. This would violate the no-cloning theorem [5], that relies on the fact that a quantum state will be projected onto the measurement basis upon measurement. Thus, a quantum state cannot be simply measured and copied. On the one hand this is a big advantage for *QKD*, because the no-cloning theorem renders man-in-the-middle attacks obsolete. On the other hand for long distance quantum communication new repeater concepts are needed. Fortunately, quantum mechanics provides a solution to this challenge by the concept of quantum repeaters. At best, the quantum repeater is a device that restores the signal but also is a compatible building block for setting up quantum networks. Hence, a quantum repeater should be a technology that enables the distribution of quantum entanglement among distant nodes. This leads to the idea of a platform built up from an entanglement resource, projective measurements and quantum memories, as introduced in Chapter 1. Different strategies are currently followed for its implementation:
One can use dissimilar quantum systems for the entanglement resource and the memory [15, 48, 60]. This would allow to combine the best entanglement resource and the best quantum memory, both

optimized for the needs of the quantum repeater. However, using different systems sets strict requirements on the compatibility of the two blocks in terms of physical specifications. Additionally, it raises the potential for more losses in the quantum repeater due to imperfect operations. The second quantum repeater concept omits these drawbacks, because it uses the very same platform for entanglement resource and quantum memory [61]. Here, the spin *qubit* is used as a quantum memory and photonic *qubits*, that are entangled to the spin *qubit*, to interface the different nodes [62–64]. This would omit compatibility losses, but it is rather difficult to find a platform that meets the stringent requirements for both parts. Hence, intrinsic imperfections need to be balanced. The last quantum repeater concept completely skips quantum memories and is consequently referred to as memory free-schemes. These rely on measurement-based operations on complex cluster states [14, 65–67]. While all the different approaches have their own advantages and disadvantages, the construction of functional quantum repeaters will most likely require merging the different concepts being developed [68].

The conceptual operation idea for quantum repeater is the following: A long channel is broken down into small segments linked by quantum repeaters, which can also act as nodes to build up a quantum network. Before being able to send a quantum signal through the network, the different nodes need to be connected. This is carried out by extending the entanglement from one single node to the two adjacent nodes via entanglement swapping [16]. For entanglement swapping each node generates an entangled photon pair. One photon of each entangled photon pair remains at the node and the second photon is sent to a *Bell State Measurement (BSM)*. The *BSM* performs a projective measurement on the two photons of the different nodes. The outcome of the measurement instructs the nodes, which operation has to be performed on the remaining photons so that the two photons are transferred in an entangled state. After performing the appropriate operation on the remaining photon on each node, the two nodes share an entangled state. This entanglement swapping protocol can be continued and applied to the next adjacent nodes following the same procedure. Performing this sequenced swapping operations enables the sharing of entanglement throughout the network, but it does not improve the transmission probability through the network. For this we need quantum memories. The quantum memories in each node store the photons until they are needed in the network. This is in particular useful in case of imperfect operations, for example a failure of the swapping operation, or for timing in the network, for example each swapping operation needs the classical signal transfer to get the unitary operation applied on the remaining photon. Hence, the quantum state has to be stored for a couple of milliseconds to allow for classical signal transfer or a new swapping operation.
In order for the whole quantum repeater technology to be advantageous each step in the operation needs to be accurately performed, which poses high demands on the basic hardware blocks. The quantum resources need to generate highly entangled photons, preferably on-demand with a low multiphoton emission probability. Meeting these conditions lowers the complexity and failure of the operation. Additionally, the photons emitted by the quantum resources should be highly indistinguishable. This an essential requirement for efficient *BSM* [18]. These are the must-have features of the entanglement resource. Some other useful features are brightness and scalability. The

brightness would allow for faster transmission rates through the network and the scalability would pave the way from prototyping towards out-of-the-lab operations. For the quantum memories, the most important figures of merits are the fidelity of state storage, a high efficiency of storage and retrieval [69], preferably on demand, with long storage times [15]. The efficiency of a quantum memory is quantified by the probability to re-emit a photon after storage. A high recall efficiency is favorable because it increases the success rate of entanglement distribution and thus makes scaling of the quantum networks easier. The fidelity is the overlap of the quantum state of the retrieved photon after storage with the input state. For practical quantum memories the fidelity needs to be higher than the no-cloning limit [70]. The storage time indicates the time over which the quantum state remains faithfully stored. In particular for long-distance quantum communication memories, the classical communication time between distant nodes imposes a lower boundary on the quantum memory storage time [15]. Hybrid quantum repeater systems require the memory also to be compatible with a broad signal bandwidth acceptance [71]. The bandwidth of the quantum memory determines the wavelength compatibility with the interfacing quantum resource and affects the achievable repetition rates [72]. Often, highly efficient memories exhibit a narrow bandwidth in the order of few MHz [73]. The long list of requirements on the quantum resources and quantum memories makes the search for the right quantum repeater platform quite demanding. One potential quantum repeater platform is given in the outlook of this thesis.

2.3 Quantum teleportation

Quantum teleportation is the transmission of a quantum state over arbitrary distances by taking advantage of entanglement. A quantum state (photon) transfers its information on a distant photon, without the need of direct interaction. This is possible by performing a measurement, more specifically a *BSM*, on the initial photon with one photon of an entangled photon pair. The measurement transfers the state of the initial photon onto the second photon of the entangled photon pair. Exploiting a shared entanglement resource to transfer a *qubit* without the *qubit* having to travel the whole distance has great potential, for example in distributed quantum computation or enhanced coordination in specific tasks. The dependence of quantum teleportation on entanglement resources underlines the potential of the entanglement distribution technology introduced before.
Both quantum teleportation and entanglement swapping rely on the same measurement, the *BSM*. The experimental implementation of quantum teleportation, however, is slightly simpler. It requires an initial *qubit*, for example prepared in H polarization, and one entangled photon source. To perform a working teleportation operation, the indistinguishability between the initial *qubit* and the interfering photon from the entangled photon source has to be high. High indistinguishability is also essential for entanglement swapping, except now between two photons from two entangled photon sources. Considering the fabrication of solid-state-quantum emitters, meeting the stringent requirements on the sources is quite challenging. But, first demonstrations on quantum teleportation [33, 74], even with imperfect emitters [34], and also entanglement swapping [35, 75] have been realized.

The concept of quantum teleportation is apparent by going through the mathematical description: As mentioned before, quantum teleportation is the procedure of transferring an input state $|\psi\rangle_1$ via a *BSM* onto one *qubit* $|\mathbf{1}\rangle_3$ (photon) from an entangled photon pair $|\phi^+\rangle_{23}$. This procedure is illustrated in Figure 2.4. A generic state of *qubit* (photon) **1**:

$$|\psi\rangle_1 = \alpha\,|0\rangle_1 + \beta\,|1\rangle_1 \tag{2.9}$$

is teleported to a second *qubit* (photon) **3**, via a shared entangled *qubit* (photon) pair **2-3**, which is in one of the four possible Bell states, i.e. the $|\phi^+\rangle$ state

$$|\phi^+\rangle_{23} = \frac{1}{\sqrt{2}}(|0\rangle_2\,|0\rangle_3 + |1\rangle_2\,|1\rangle_3) \tag{2.10}$$

The complete three-photon state is the tensor product of the elements, and is written as

$$\begin{aligned} |\xi\rangle &= (\alpha\,|0\rangle_1 + \beta\,|1\rangle_1) \otimes \frac{1}{\sqrt{2}}(|0\rangle_2\,|0\rangle_3 + |1\rangle_2\,|1\rangle_3) \\ &= \frac{1}{\sqrt{2}}(\alpha\,|0\rangle_1\,|0\rangle_2\,|0\rangle_3 + \alpha\,|0\rangle_1\,|1\rangle_2\,|1\rangle_3 + \beta\,|1\rangle_1\,|0\rangle_2\,|0\rangle_3 + \beta\,|1\rangle_1\,|1\rangle_2\,|1\rangle_3) \end{aligned} \tag{2.11}$$

We can take advantage of the completeness of the Bell states and rewrite the state from the computational basis in a straightforward representation to understand the operation principle of the protocol. The computational basis can be expressed in terms of Bell states the following way:

$$\begin{aligned} |00\rangle &= \frac{1}{\sqrt{2}}(|\phi^+\rangle + |\phi^-\rangle) \\ |11\rangle &= \frac{1}{\sqrt{2}}(|\phi^+\rangle - |\phi^-\rangle) \\ |01\rangle &= \frac{1}{\sqrt{2}}(|\psi^+\rangle + |\psi^-\rangle) \\ |10\rangle &= \frac{1}{\sqrt{2}}(|\psi^+\rangle - |\psi^-\rangle) \end{aligned} \tag{2.12}$$

Using Eqs. (2.12), the state in Eq. (2.11) can be expressed as

$$\begin{aligned} |\xi\rangle &= \frac{1}{\sqrt{2}}[(\alpha\frac{1}{\sqrt{2}}\,|\phi^+\rangle_{12} + |\phi^-\rangle_{12})\,|0\rangle_3 + \alpha\frac{1}{\sqrt{2}}(|\psi^+\rangle_{12} + |\psi^-\rangle_{12})\,|1\rangle_3 \\ &\quad + \beta\frac{1}{\sqrt{2}}(|\psi^+\rangle_{12} - |\psi^-\rangle_{12})\,|0\rangle_3 + \beta\frac{1}{\sqrt{2}}(|\phi^+\rangle_{12} - |\phi^-\rangle_{12})\,|1\rangle_3] \\ &= \frac{1}{2}[|\phi^+\rangle_{12}\,(\alpha\,|0\rangle_3 + \beta\,|1\rangle_3) + |\phi^-\rangle_{12}\,(\alpha\,|0\rangle_3 - \beta\,|1\rangle_3) \\ &\quad + |\psi^+\rangle_{12}\,(\alpha\,|1\rangle_3 + \beta\,|0\rangle_3) + |\psi^-\rangle_{12}\,(\alpha\,|1\rangle_3 - \beta\,|0\rangle_3)] \end{aligned} \tag{2.13}$$

Now, by performing a *BSM* between qubit (photon) **1** and **2**, the input state of qubit (photon) **1** will be projected to one of the states in Eq. (2.13). The two qubits (photons) **1** and **2** are coupled and destroyed in the *BSM*, while qubit (photon) **3** will collapse in one of the four different states. Depending on the *BSM*, a unitary transformation on qubit (photon) **3** has to be applied in order to obtain the initial state $|\psi\rangle$. The unitary transformations dependent on the Bell state measurement

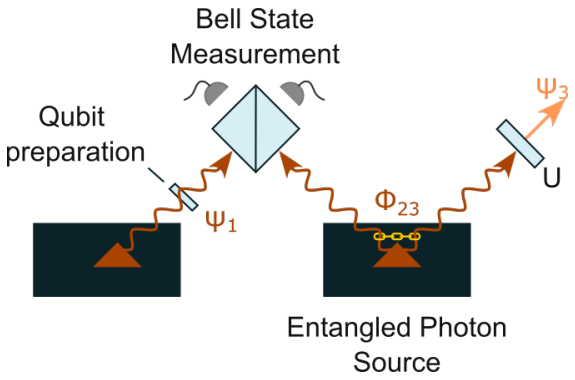

Figure 2.4. Sketch of quantum teleportation. A *qubit*, whose information will be teleported, is prepared in a specific state ψ_1. Additionally, an entangled photon pair ϕ_{23} is generated. One photon of the entangled photon pair is sent to a *BSM* with the *qubit*, which we want to teleport. The *BSM* transfers the information from the prepared *qubit* to the interacting photon of the entangled photon pair. Depending on the result of the *BSM*, a unitary transformation U on the second *qubit* of the entangled photon pair is applied, in order to restore the actual state of the prepared *qubit*.

results are:

$$\begin{aligned} |\phi^+\rangle_{12} &\to I & |\psi^+\rangle_{12} &\to \sigma_x \\ |\phi^-\rangle_{12} &\to \sigma_z & |\psi^-\rangle_{12} &\to \sigma_y \end{aligned} \tag{2.14}$$

where I is the identity and σ_i $(i = x, y, z)$ the Pauli matrices. If we take as an example, the *BSM* on the state $|\psi^-\rangle_{12}$, the polarization state of photon **1** is transferred on qubit (photon) **3**, with a rotation. If we now apply the belonging unitary transformation σ_y, the following relation results:

$$\sigma_y(\alpha\,|1\rangle_3 - \beta\,|0\rangle_3) = (\alpha\,|0\rangle_3 + \beta\,|1\rangle_3) \tag{2.15}$$

which resembles the initial state that was teleported. Consequently, the initial state of photon **1** was teleported onto photon **3**. The necessary tools were the *BSM* and the potential unitary transformations, which can easily be performed using half-waveplates.

2.3.1 Bell state measurement

The core process in quantum teleportation is the *BSM*. An efficient measurement of the Bell state is crucial for the perfomance of the teleportation process. The *BSM* setup has a rather simple composition, a balanced beam splitter and two single-photon detectors (illustrated in Fig. 2.4). The crucial step is the interaction of the beam splitter with photons.
When a photon impinges on one of the two entrances of a balanced beam splitter, the output will be a superposition of the two exit ports. The interaction can be mathematically described with the use of the creation $\hat{a}^\dagger$ and annihilation $\hat{a}$ operators, acting on a Fock state $|0\rangle$. Note, the reflected paths undergo a phase shift of π, due to conservation of energy. Consequently, the beam splitter transformation can be expressed as the following:

$$\begin{aligned} |1\rangle_1 &\to \tfrac{1}{\sqrt{2}}(\hat{a}_3^\dagger + i\hat{a}_4^\dagger)\,|0\rangle \\ |1\rangle_2 &\to \tfrac{1}{\sqrt{2}}(i\hat{a}_3^\dagger + \hat{a}_4^\dagger)\,|0\rangle \end{aligned} \tag{2.16}$$

Two-photon interference at a beam splitter

The *BSM* is based on two-photon interference, in detail, the overlap of two wavefunctions in a balanced beam splitter.
Lets consider two, in all degrees of freedom, indistinguishable single photons, that are prepared in a pure polarization state and then sent each into one of the two entrance ports (1,2) of a balanced beam splitter (see Figure 2.5). This can be written as two creation operators acting on a common vacuum state:

$$\begin{aligned} |1\rangle_1 |1\rangle_2 &= \hat{a}_1^\dagger \hat{a}_2^\dagger |0\rangle \\ &= \frac{1}{\sqrt{2}}(\hat{a}_3^\dagger + i\hat{a}_4^\dagger)\frac{1}{\sqrt{2}}(i\hat{a}_3^\dagger + \hat{a}_4^\dagger)|0\rangle \\ &= \frac{1}{2}(i\hat{a}_3^\dagger\hat{a}_3^\dagger + \hat{a}_3^\dagger\hat{a}_4^\dagger + (i^2)\hat{a}_4^\dagger\hat{a}_3^\dagger + i\hat{a}_4^\dagger\hat{a}_4^\dagger)|0\rangle \\ &= \frac{1}{\sqrt{2}}(|2\rangle_3 |0\rangle_4 + |0\rangle_3 |2\rangle_4) \end{aligned} \tag{2.17}$$

The two indistinguishable photons enter from different entrance ports, however, exit at the same output ports. This phenomenon is called the *Hong-Ou-Mandel (HOM)* effect on a 50:50 beam splitter [76] and it tells us, in case two photons are identical in every degree of freedom (i.e. spatiotemporal mode, energy, polarization and time of arrival on the beam splitter), we observe the *bosonic coalescence*, a solely quantum effect, and the two photons will be found at the same exit of the beam splitter. If we now collect time correlations on clicks of two *Avalance Photo Diodes (APDs)*, which are placed at the output ports of the beam splitter, we should detect no clicks at a time-delay zero between the two detectors. It is worth mentioning, as it will be discussed in more depth in Section 4.5, that, when performing these time correlations in a laboratory, there are always some clicks at zero-time delay. These are related to non-perfect indistinguishably of the two interfering photons due to time jitter in the emission process, spectral wandering or dephasing, which result in indistinguishable photons.

In the experimental conditions the interfering photons in quantum teleportation are often expressed in terms of Bell states. This representation is the most convenient, since it makes evident the action of the two-photon interference process, which discriminate the polarization states based on their symmetry. For this reason, we determine the expected outputs, when two photons of a specific Bell state impinge at the same time at the beam splitter. We now consider polarization of the impinging photons by adding the subscript h and v for the linear polarization basis. Therefore, we extend Eq. (2.17) for the interference of the two photons, with Bell states as input states:

$$\begin{aligned} |\phi^+\rangle_{12} &= \tfrac{1}{\sqrt{2}}(\hat{a}_{1,h}^\dagger\hat{a}_{2,h}^\dagger + \hat{a}_{1,v}^\dagger\hat{a}_{2,v}^\dagger)|0\rangle &&\rightarrow \tfrac{1}{2\sqrt{2}}(|2_h\rangle_3 + |2_v\rangle_3 + |2_h\rangle_4 + |2_v\rangle_4) \\ |\phi^-\rangle_{12} &= \tfrac{1}{\sqrt{2}}(\hat{a}_{1,h}^\dagger\hat{a}_{2,h}^\dagger - \hat{a}_{1,v}^\dagger\hat{a}_{2,v}^\dagger)|0\rangle &&\rightarrow \tfrac{1}{2\sqrt{2}}(|2_h\rangle_3 - |2_v\rangle_3 + |2_h\rangle_4 - |2_v\rangle_4) \\ |\psi^+\rangle_{12} &= \tfrac{1}{\sqrt{2}}(\hat{a}_{1,h}^\dagger\hat{a}_{2,v}^\dagger + \hat{a}_{1,v}^\dagger\hat{a}_{2,h}^\dagger)|0\rangle &&\rightarrow \tfrac{1}{\sqrt{2}}(|1_h1_v\rangle_3 + |1_h1_v\rangle_4) \\ |\psi^-\rangle_{12} &= \tfrac{1}{\sqrt{2}}(\hat{a}_{1,h}^\dagger\hat{a}_{2,v}^\dagger - \hat{a}_{1,v}^\dagger\hat{a}_{2,h}^\dagger)|0\rangle &&\rightarrow \tfrac{1}{\sqrt{2}}(|1_h\rangle_3 |1_v\rangle_4 - |1_v\rangle_3 |1_h\rangle_4) \end{aligned} \tag{2.18}$$

One can see that the $|\psi^-\rangle_{12}$ leads to two photons at distinct output ports. The reason for this

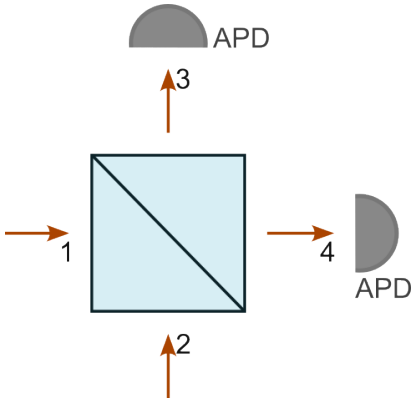

Figure 2.5. Sketch of a Bell state measurement. Two photons are entering at the two entrance ports of a 50:50 beam splitter. When both photons exit at different exit ports, the entering state was $|\psi^-\rangle_{12}$. The other Bell states cannot be discriminated with this setup, because in these cases two photons exit the same port.

lays in the two-photon state. This state is the only one which is anti-symmetric under exchange of particles. The other Bell states, however, have symmetric spatial wavefunctions. For the $|\psi^+\rangle_{12}$, the two photons exit the same output port, but they differ in polarization. For $|\phi^\pm\rangle_{12}$, both photons also exit at the same output port and also have the same polarization. From these formulas we can now see that we can easily detect the $|\psi^-\rangle_{12}$ state by collecting the correlations with respect to different arrival times on the two *APDs*, at each output port of a regular beam splitter. Detecting the $|\psi^+\rangle_{12}$ is also possible with linear optics, by adding a polarizing beam splitter after the 50:50 beam splitter. Because even though the two photons for the $|\psi^+\rangle_{12}$ state exit the same output port, we can split them due to their difference in polarization. Thus, we can measure it by correlating coincidences between *APDs* after the two polarizing beam splitters. The $|\phi^\pm\rangle_{12}$, however, exit from the same output port and have the same polarization. If we correlate coincidences between the two output ports of the beam splitter, we will always have a dip at zero-time delay. Additionally, since they have the same polarization there is no way to discriminate the two photons using linear optics. However, exploiting non-linear optics also these states can be differentiated [77], even if this is very challenging to implement efficiently.

Chapter 3

Fundamentals of GaAs droplet-etched quantum dots

3.1 Introduction to semiconductor quantum dots

As discussed in the previous section, quantum networks and *QKD* systems are often based on platforms using entangled photons. The current state-of-the-art entangled photon sources exploit parametric down conversion. A polarized pump laser is focused on a non-linear crystal and generates under energy and momentum conservation two entangled photons, which have half the energy of the pump source. The crystals are categorized in two types, type-I and type-II. Type-I *Spontaneous Parametric Down Conversion (SPDC)* relies on two crystals placed one after each other with their crystal axis being rotated 90° between them. For example, when a pump beam oscillates at 45° with respect to the horizontal axis, the first crystal generates a horizontally-polarized photon and the second generates a vertically-polarized photon. Type-II crystals, on the other hand, are single crystals, whose nonlinearity creates two cones, one composed by horizontally-polarized photons, the second by vertically-polarized photons. Selecting the two photons from the two intersection points of the two cones, the photons are correlated and are in a superposition of their polarization states. *SPDC* sources provide nearly-maximally entangled photons [20], used for the longest distance realization of *QKD* over 1200 km [78]. To improve the key rate in *QKD*, the pump power sent on the crystal needs to be increased. However, increasing the pump power to a level where the probability of generating at least an entangled photon pair approaches unity, also raises the multipair emission probability, due to the non-zero probability of emitting more than one entangled photon pair per excitation pulse [79]. Consequently, the multipair emission impairs the entanglement fidelity [21], which limits the achievable secure key rate in *QKD* [22, 23].

For these reasons, alternative entangled photon sources are currently investigated. One promising entangled photon source, with the potential of generating entangled photons on demand and meeting the stringent requirements of the *QKD* and quantum repeater schemes are *Semiconductor Quantum Dots (QDs)*. *QDs* can generate polarization-entangled photon pairs via the biexciton-exciton cascade [26] with extremely low multiphoton emission probability [27, 28], high degree of

entanglement [80] photon-indistinguishability [29, 30] wavelength-tunability [31] and with nearly on-demand generation [25].

As their name implies, *QDs* are structures based on semiconductor materials, showing quantum confinement effects. Semiconductor materials are crystals where the Fermi energy is situated within the energy gap (E_g). Thus, at 0 K all available states in the valence band are filled, whereas the conduction band is fully empty. By using an electric or light source with an energy $hv \geq E_g$, the gap energy, an electron from the valence band is promoted to the conduction band. This electron can return to the valence band after the radiative lifetime by the emission of a photon. Since various states are possible to be excited in the conduction band, the emission of a semiconductor bulk material comprises a broad spectrum. But, the optical and electrical properties of semiconductors can be altered by inserting impurities into the lattice or building heterostructures. Prominent examples are III-V group heterostructures, built from GaAs/AlGaAs. When creating heterostructures in the nanometer scale the electron motion gets confined within the lower bandgap material, which increases the uncertainty in its momentum and consequently the average kinetic energy, due to the Heisenberg principle. If the confinement is comparable or below the de Broglie wavelength for thermal motion, quantum confinement arises. This is indeed the case for heterostructure dimensions in the nanometer - tens of nanometer range. We speak of quantum wells for a one-dimensional confinement, quantum wires, for two-dimensional confinement and *QDs*, for three-dimensional confinement. Looking at the density of states for the different confinement dimensions, we can see that the possible states in the conduction band are connected to higher confinement in the potential well. For three-dimensional confinement only discrete energies are allowed. Hence, light emitted by three-dimensional confined objects have specific energies. Thus, the emission spectrum comprises isolated lines similar to an atom. *QDs*, when fabricated small enough exhibit these three-dimensional confinement effects and emit light with discrete energies. For this reason, *QDs* are referred to as artificial atoms, despite being often formed by tens of thousands of atoms.

3.2 Fabrication of semiconductor quantum dots - Aluminum droplet etching

To fabricate *QDs* with optical properties suitable for quantum information experiments, several methods have been developed over the past. The main challenge is to control size, density and uniformity while keeping it compatible with the growth technique.

The most prominent techniques are based on epitaxial growth of self-assembled nanostructures using molecular beam epitaxy or metalorganic vapor phase epitaxy. Most of the pioneering experiments in the field relied on *QDs* fabricated by the Stranski-Krastanow growth mode. This technique relies on the spontaneous formation of crystalline three-dimensional islands due to strain induced by the lattice mismatch of the different deposited materials [81]. This strain driven mechanism is compatible with standard molecular beam epitaxy technology and leads to excellent crystalline and

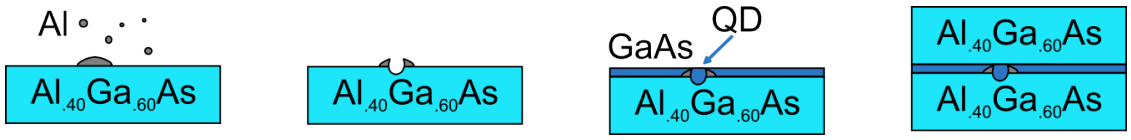

Figure 3.1. Sketch of the droplet etching technique to fabricate uniform *QDs*. First aluminum (Al) droplets are deposited on the $Al_{0.4}Ga_{0.6}As$ matrix. When heating, the Al evaporates, leaving behind an etch pit in the host matrix. The next step, depositing a thin layer of GaAs, fills the drilled holes. To prevent surface states, influencing the optical quality of the nanostructures, the GaAs material is capped with another layer of host matrix of $Al_{0.4}Ga_{0.6}As$.

optical quality. However, it is restricted to specific heterostructures with a large lattice mismatch such as InAs/GaAs [81] or Ge/Si [82]. This is not the case for GaAs/AlGaAs, which have similar lattice constants. Additionally, strain effects in the *QDs* lead to entanglement degradation, as discussed later on in Section 3.5.1. Almost strain-free and highly symmetric GaAs *QDs* are fabricated with a more recent fabrication technique called *Local Droplet Etching (LDE)* [83]. *LDE* does not rely on strain and is performed at higher temperatures compared to conventional droplet epitaxy, a former technique to fabricate strain-free *QDs* [84]. Hence, *LDE* provides an improved crystal quality, narrower emission linewidths [85] and consequently, having entanglement fidelities above 90 %.

The *QD* samples used in this thesis are grown in a collaborating group of ours, at the Institute of Seminconductor and Solid-State Physics Department at the Johannes Kepler University of Linz (AT). The droplet epitaxy growth is conducted in a molecular beam epitaxy machine, which can deposit thin-films of single crystals. The sample fabrication starts with an $Al_{0.4}Ga_{0.6}As$ layer grown on a (001) GaAs commercial wafer. To achieve artificial-atom like structures we need a second material which is capped within the host material in the nanometer size. To achieve this first, Al droplets are deposited on the $Al_{0.4}Ga_{0.6}As$ layer, see Figure 3.1. These evaporate in the next annealing step - heating the molecular beam epitaxy growth chamber to 600°- and leave holes with 10 - 100 nm diameter and ∼10 nm height in the $Al_{0.4}Ga_{0.6}As$ layer. The nanoholes are now filled with the *QD* material. This is performed by depositing a 2 nm thick GaAs layer. To achieve confinement in growth direction, the GaAs layer is capped by a 123 nm thick $Al_{0.4}Ga_{0.6}As$ layer. With the deposition parameters chosen for our work the *QDs* exhibit a height of 7 - 8 nm and a diameter of 50 - 60 nm. This size results in a weak confinement of the charges and an emission wavelength of ∼790 nm at cryogenic temperature [86]. By changing the depth of the nanoholes, which means changing the amount of GaAs during filling and the Al content of the barriers, the average emission wavelength can be tuned [87], i.e., tuning it to around 780 nm [36], favorable for satellite-based *QKD* due to the atmospheric transmission window between 775 - 785 nm [88]. In order to serve different communication spectral windows other choices of materials are required.

The bare structure of a vertical stack of semiconductor materials is very inefficient for collecting light using confocal microscopy. First, the emission takes place in all directions of the nanostructure. Second, the high refractive index of the AlGaAs would lead to mostly total internal reflection [89]. This challenge is directly tackled by sample fabrication, by immediately growing a λ-cavity

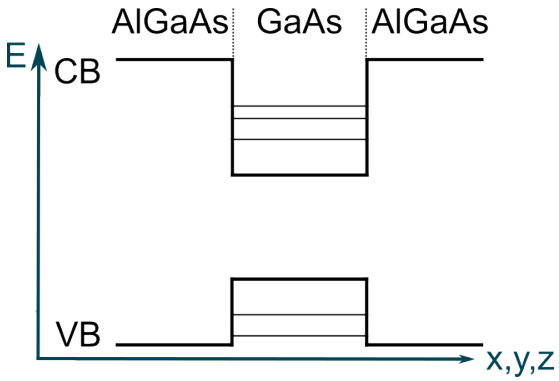

Figure 3.2. The heterostructure consisting of a sandwiched GaAs between a AlGaAs host matrix, leads to a drop of the conduction band (CB) and rise of the valence band (VB) in the potential landscape, effectively a potential. The local change in potential energy (E), traps the electron and holes in the vicinity and confines their motion, resulting in discrete energy levels.

on the sample. The optical cavity enhances the coupling between the emitter and a specific electromagnetic mode to improve the directionality of the spontaneous emission.
To do so, the active layer ($Al_{0.4}Ga_{0.6}As$/GaAs/$Al_{0.4}Ga_{0.6}As$) is grown between 60 nm thick $Al_{0.2}Ga_{0.8}As$ layers. This change in material composition results in a λ-cavity effect. Additionally, sets of *Distributed Bragg reflectors (DBRs)* are grown. These consist of 9 (on the one side) and 2 (on the opposite side) layer pairs of $Al_{0.95}Ga_{0.05}As$ with a thickness of 70 nm and $Al_{0.2}Ga_{0.8}As$ with a thickness of 60 nm. These two amendments, λ-cavity and *DBR*, results in a 10 % efficiency to collect the emitted light from the top surfaces of a planar unprocessed sample [90]. Additional techniques used to increase the extraction efficiency are discussed later on in Section 3.5.3.

3.3 Modeling semiconductor quantum dots

Impurities or fabricated heterostructures lead to a change in the potential landscape of the material. For GaAs/AlGaAs *QDs* this potential change is simply imagined the following way: The nm-range structures of the GaAs inside the host material AlGaAs build a heterostructure, more specifically a type-I heterostructure. This type realizes a rise in the valence band and a drop in the conduction band potential landscape. Thus, a sandwich of these two materials results in a potential well for both bands and consequently traps the electron and hole at the same position. A schematic picture of the potential landscape around a GaAs *QD* in an AlGaAs host matrix is illustrated in Figure 3.2.

3.3.1 The infinite potential well

The simplest model describing the energy levels of this heterostructure is the model of a confined particle in an infinite potential well (particle in a box) [91]. Despite its simplicity the infinitely deep well gives a solid approximation of the energy levels of a *QD*.
The time-independent Schrödinger equation for an infinite potential well in one dimension, where the free particle with an effective mass m^* moves in the spatial interval $0 < x < L$, with L the confinement length, is expressed as:

$$-\frac{\hbar^2}{2m^*}\frac{d^2\Psi}{dx^2} + V(x)\Psi(x) = E\Psi(x) \tag{3.1}$$

The solutions of this Schödinger equation are sinusoidal wave functions which fulfill the boundary conditions that the wave vanishes at the edge of the barrier region. Thus, we have stationary waves with nodes in $x = 0, L$ and the wave functions and energies result to:

$$\Phi_n(x) = \sqrt{\frac{2}{L}}sin(k_n x) = \sqrt{\frac{2}{L}}sin(\frac{n\pi x}{L}) \tag{3.2}$$

$$E_n = \frac{\hbar^2\pi^2 n^2}{2m^* L} \tag{3.3}$$

The integer $n = 1, 2, 3, ...$ is a quantum number that labels the confined states of the well and $m^* = m_0 \cdot m_e$ the effective mass, where m_0 is the electron mass and m_e the reduced mass due to the band structure. The later can be derived from the curvature of the band.

An extension to three-dimensions is straightforward considering that the potential $V(x, y, z)$ can be decomposed to a linear sum of potentials $V(x, y, z) = V_x(x) + V_y(y) + V_z(z)$, where each potential depends only on one coordinate. Using this approximation, the Schrödinger equation is now separable into three one-dimensional problems. Consequently, the solutions for the wave functions and energies result to:

$$\begin{aligned}\Phi_{n_x,n_y,n_z}(x, y, z) &= 2\sqrt{\tfrac{2}{L_x L_y L_z}}sin(k_n x)sin(k_n y)sin(k_n z) \\ &= 2\sqrt{\tfrac{2}{L_x L_y L_z}}sin(\tfrac{n\pi x}{L_x})sin(\tfrac{n\pi y}{L_y})sin(\tfrac{n\pi z}{L_z})\end{aligned} \tag{3.4}$$

$$E_n = \frac{\hbar^2\pi^2}{2m^*}[(\frac{n_x}{L_x})^2 + (\frac{n_y}{L_y})^2 + (\frac{n_z}{L_z})^2] \tag{3.5}$$

with $n_x, n_y, n_z = 1, 2, 3, ...$ the three independent quantum numbers that label the confined states of the well.

This basic model captures two essential features of *QDs*, the discretization of energy levels and the zero-point energy, meaning the lowest state has a positive energy. Both are summarized in the energy spectrum E_n of Eq. (3.5).

Although an infinitely deep well cannot be fabricated, it is simple nowadays to grow structures that are close to ideal finite wells. For example, if we now consider a heterostructure that consists of a thin sandwich of GaAs between thick layers of AlGaAs (i.e. an alloy such as $Al_{0.3}Ga_{0.7}As$), we end up with a simple quantum well. We can check the conditions at which size the GaAs structure exhibits quantization effects, meaning discrete energy levels. More importantly we are interested in the spacing between the energy levels. In order to have the possibility to deterministically promote a particle from the ground state to the first excited state the spacing between the ground state energy to the first excited state energy has to be higher than the thermal energy, so that the thermal energy is barely sufficient to promote the particle from the ground state to the first excited state.

This condition reads as $E_1 - E_0 > 3k_BT$, with E_1 and E_0, the first excited and ground state, k_B the Boltzmann constant and T the temperature. Plugging these values into Eq. (3.5), and rewriting the function for L_x, if $L_z < L_y < L_x$, we end up with the following equation:

$$L_x \leq \frac{\hbar\pi}{\sqrt{2m^* k_B T}} \tag{3.6}$$

Using the reduced mass ($m_e = 0.067$) of GaAs, for example, the minimum size of the quantum well must be at room temperature ca. 15 nm. As a result, we could demonstrate with a very simple and straight forward manner using only the model of a particle in an infinite potential well, that QDs with sizes smaller than 15 nm exhibit confinement effects. According to the model, these *QDs* have discrete energy levels, behaving similar to an artificial atom.

Using this simplistic model we can describe the two main features of the *QD* spectrum, the quantization effect and the minimum energy. One might argue that this simplistic model does not account for any effects given by the host material and all effects introduced by the band structure of the surroundings were neglected up to now.

3.3.2 Effective mass approximation

The following model considers the heterostructure - quantum well and barrier - in more depth. This provides more insight to the effective mass approximation and how it is linked to the actual physical system. The quantum mechanical motion of electrons in the crystal is exposed to the periodic lattice potential and perturbed by a defect or quantum well. To model the electronic motion we treat the quantum well as a static perturbation to a perfect crystal. Additionally, we restrict the perturbation to be small enough to be treated in lowest order perturbation theory, and of a spatial range much larger than the lattice constant of the underlying material. These restrictions allow for considerable simplifications leading to an effective mass Schrödinger equation for electrons in the conduction bands with parabolic dispersion.

To provide a quantitative, yet approximate, description of the equation of motion of the electronic structure of a semiconductor *QD*, we search for the solution of the Schrödinger equation of a localized three-dimensional potential well V_{per}, the perturbation of the quantum well, within a periodic Hamiltonian H_{crys} of the crystal:

$$[\hat{H_{crys}} + V_{per}(\mathbf{r})]\Psi(\mathbf{r}) = E\Psi(\mathbf{r}) \tag{3.7}$$

This Schödinger equation is a difficult problem, whose exact solution is not solvable analytically. However, reasonable assumptions simplify the equation, leading us to approximate solutions for the energies.

We can safely assume that the Schrödinger equation for the unperturbed crystal $\hat{H}_{crys}\Psi(\mathbf{r}) = E\Psi(\mathbf{r})$, with the corresponding dispersion relations $E_n(\mathbf{k})$ and the Bloch-functions $\Phi_{nk(\mathbf{r})} = u_n(\mathbf{k})e^{i\mathbf{kr}}$, are known. Also it can be assumed, that the perturbing potential changes slowly on the scale of

the lattice constant, i.e. $V_{per}(\mathbf{r})$ contributes only significantly in the region « π/a in k-space. And additionally, we assume that the perturbation is small compared to typical energy separations of bands in the crystal, and that the values of the coefficient $u_n(\mathbf{k})$ are only significant for small values of $\mathbf{k}$. The last assumption is on the considered bands. For the lowest lying confined levels, which we are mainly interested in our applications, we can assume that only the closest bands to the Fermi level, the s-like conduction band and the heavy hole p-like valence band, contribute.
Using these assumptions we can write the wave function $\Psi(\mathbf{r})$ of the system with the perturbation as an expansion of Bloch-functions of the perfect crystal $\Phi_{nk}(\mathbf{r}) = u_n(\mathbf{k})e^{i\mathbf{kr}}$ with the expansion coefficients $\tilde{\chi}_n(k)$. Note, V_{per} contains all differences, electronic motion and potential changes, introduced by the quantum well. To include all states, we sum over all bands n and integrate over all possible momenta k in the Brillouin zone $[-\frac{\pi}{a}, \frac{\pi}{a}]$, with a the lattice constant.

$$\Psi(\mathbf{r}) = \sum_n \int_{-\pi/a}^{\pi/a} \tilde{\chi}_n(k)\Phi_{nk}(\mathbf{r})\frac{dk}{2\pi} \tag{3.8}$$

The summation over all bands n can be dropped, since we assume that only one band of the unperturbed crystal is important in the interaction with the perturbation. This single-band approximation can be applied when looking at the lowest confined levels, otherwise this approximation is rather inaccurate. Additionally, we can apply the effective mass approximation. The effective-mass approximation disregards the detailed band structure of the semiconductor and only accounts for the energy dispersion near the conduction band minimum and the valence band maximum. Thus, only states from a small region of k-space contribute significantly to the integral. This is an eligible assumption for GaAs and AlGaAs with low Al contents, because the lowest band gap is in the Γ-point ($k = 0$). Consequently, the crystal wave function can be reduced to a Bloch function of the perfect crystal $\Phi_{nk}(\mathbf{r}) \approx \Phi_{n0}(\mathbf{r})$ at the Γ-point and the electron wave function can be written as a product of the perfect crystal wavefunction modulated by an envelope function $\chi_n(k)$, that slowly varies with respect to the crystal lattice constant.

$$\Psi(\mathbf{r}) \approx \Phi_{n0}(\mathbf{r}) \int_{-\pi/a}^{\pi/a} \tilde{\chi}_n(k)\frac{dk}{2\pi} = \Phi_{n0}(\mathbf{r})\chi_n(\mathbf{r}) \tag{3.9}$$

The problem is now reduced to a pseudo Schrödinger equation for the envelop function containing an effective Hamiltonian. The Bloch function and the periodic potential of the crystal vanished only leaving the full dispersion curve $\epsilon_{crys,n}(\mathbf{k})$ for band n.

$$[\epsilon_{crys,n}(-i\nabla) + V_{per}(\mathbf{r})]\chi_n(\mathbf{r}) = E\chi_n(\mathbf{r}) \tag{3.10}$$

The full band structure for $\epsilon_{crys,n}(\mathbf{k})$ is simplified with the effective mass approximation and reduces to a parabolic dispersion around Γ.

$$\epsilon_{crys,n}(\mathbf{k}) \approx E_c + \frac{\hbar^2 k^2}{2m^*} \tag{3.11}$$

E_c is the energy of the bottom of the conduction band and $m^* = m_0 \cdot m_e$, where m_0 is the electron mass and m_e the effective mass of the electrons. We can now replace $\mathbf{k} \to -i\nabla$ and substitute the approximated energies back in Eq. (3.10). It results a pseudo Schrödinger equation

that resembles that for free electrons with an effective mass and an energy measured from the bottom of the conduction band.

$$[-\frac{\hbar^2}{2m^*}\nabla^2 + V_{per}(\mathbf{r})]\chi_c(\mathbf{r}) = (E - E_c)\chi_c(\mathbf{r}) \tag{3.12}$$

χ_c is the envelope function for the electron quasiparticle in the conduction band.

The electron behavior in a heterostructure can now be estimated considering a finite square potential well. The drop in the potential structure in the conduction band would correspond to the drop in the conduction band minimum. Additionally, the effective mass inside the quantum well $[-L, L]$ would change from the effective mass of the bulk $m_{e,B}$ to that of the perturbing material $m_{e,Per}$.

$$\begin{cases} V = 0 & \mathbf{r} > L \\ V = -\Delta E_c & \mathbf{r} < L \end{cases} \qquad \begin{cases} m^* = m_0 \cdot m_{e,B} & \mathbf{r} > L \\ m^* = m_0 \cdot m_{e,Per} & \mathbf{r} < L \end{cases} \tag{3.13}$$

Using this estimation, one can get a first reasonable approximation of the energy levels of an electron in a *QD*.

3.4 Excitonic complexes

In the previous section we discussed the electronic structure of a *QD* and how we can model it. The confined motion that was considered was only that of the electron in a single-particle picture. But let's now go a step further and populate these discrete states of the *QD*. When we excite an electron from the valence band into the conduction band, a hole is left in the valence band. This hole can be treated as a positive charge and consequently, we should consider an electron-hole pair rather than only an electron. For this reason, we extend the Hamiltonian from before by taking into account the Coulomb interaction between the confined electrons and holes. We introduce the electrostatic coupling term W_{ij}

$$W_{ij}(r_i, r_j) = \frac{1}{4\pi\epsilon_r\epsilon_0}\frac{e_i e_j}{|r_i - r_j|} \tag{3.14}$$

which describes the contribution to the total energy of the system from each electron-hole pair i, j with charge e at a distance $|r_i - r_j|$ and the dielectric constant of the material ϵ_r. A single electron-hole pair has an attractive interaction, thus, lowering the total energy of the system. This bound complex is also referred to as *Exciton (X)*. The force between the electron-hole pair can be approximated by an attractive Coulomb interaction. The binding energies can then be calculated with the effective masses of the electron m_e and hole m_h and the relative dielectric constant ϵ_r of the semiconductor material:

$$E_X(n) = \frac{m_e m_h}{(m_e + m_h)m_0}\frac{1}{\epsilon_r^2}\frac{E_{Ry}}{n^2} \tag{3.15}$$

E_{Ry} is the Rydberg energy of the hydrogen atom and n, the quantum number. When we plug the numbers $E_{Ry} = 13.6eV$, $\epsilon_r = 12.53$, $m_e = 0.067 \cdot m_0$ and $m_h = 0.51 \cdot m_0$ for GaAs, we get a

binding energy of ca. 5.1 meV for the first bound state in bulk GaAs [92].

The first excited state (called s-shell of the *QD* by loose analogy to the atomic systems) of the electronic structure can be occupied by more than one electron-hole pair. Electrons are fermions, and thus, obey the Pauli exclusion principle and occupy the same level with maximum two electron-hole pairs with opposite spin directions. Consequently, the carrier configuration is limited for the first excited state to a finite number. The different occupation configurations for this state are depicted in Figure 3.3.
First, we have the neutral *X* complexes. These are formed with heavy-holes with a spin contribution of $J_{hh,z} = \pm\frac{3}{2}$. Due to the confinement of the *QD* the degeneracy between heavy- and light-holes, where the later have a projection of the total angular momentum of $J_{lh,z} = \pm\frac{1}{2}$, is lifted and thus the assumption that the valence band is only composed of heavy-hole states is valid. Consequently, four different total angular momenta $M = S_{e,z} + J_{hh,z}$ for the different combinations of heavy-holes and electrons are possible. The latter have a spin contribution of $S_{e,z} = \frac{1}{2}$. The two configurations, $-\frac{3}{2} - \frac{1}{2}$ and $\frac{3}{2} + \frac{1}{2}$, result in a total angular momentum of $|M| = 2$. These cannot decay to the ground state by emitting a single photon. For this reason, they are referred to as "dark" states. The remaining two possibilities, $-\frac{3}{2} + \frac{1}{2}$ and $\frac{3}{2} - \frac{1}{2}$, have a total angular momentum of $|M| = 1$. These states are "bright" states and recombine efficiently to the ground state with the emisson of a photon. Depending on the component of the total angular momentum, the photon has either circular-right σ^+ ($M = +1$) or circular-left σ^- ($M = -1$) polarization.
Additionally to the single electron-hole pair configurations, an additional charge, electron or hole, can occupy the conduction or valence band state. These complexes are referred to as Trions. The additional charge interacts with the *X* and changes the *X* binding energy. Depending on the charge it is either a positive Trion X^+ with $|M| = \frac{1}{2}$ and negative Trion X^- with $|M| = \frac{3}{2}$. In a simplified meanfield picture, the *X* acts as an attractive potential for an additional electron, and repulsive for a hole, consequently the binding energy for the negative Trion would be lower and for the positive Trion would be higher with respect to the *X* binding energy [93, 94].
The last occupation possibility is the *Biexciton (XX)* state with $M = 0$, where two electron-hole pairs are present.

As mentioned before, the excitonic complexes are bound by Coulomb interaction. Since we are now interested in populating the states with multiple electrons and holes, we need to consider their interactions. Hence we extend the electrostatic coupling term to:

$$W_{ij}(r_i, r_j) = \int\int \frac{e_i e_j}{4\pi\epsilon_r\epsilon_0} \frac{|\psi_i(\mathbf{r}_i)|^2 |\psi_i(\mathbf{r}_j)|^2}{|\mathbf{r}_i - \mathbf{r}_j|} d\mathbf{r}_i d\mathbf{r}_j \tag{3.16}$$

Depending on the different interaction terms, the spatial extent of the wave function of the single particles, and on their relative position inside the *QD*, the magnitude of the coupling term varies. As a very rough, and quite inaccurate estimate one can use the following explanation to understand the different interactions of the electrons and holes in a *QD*. The interaction term for two electrons and holes, for example, is positive W_{ee},$W_{hh} > 0$, due to repulsive interaction between the same particle types, whereas the interaction term of an electron and hole is negative $W_{eh} < 0$ due

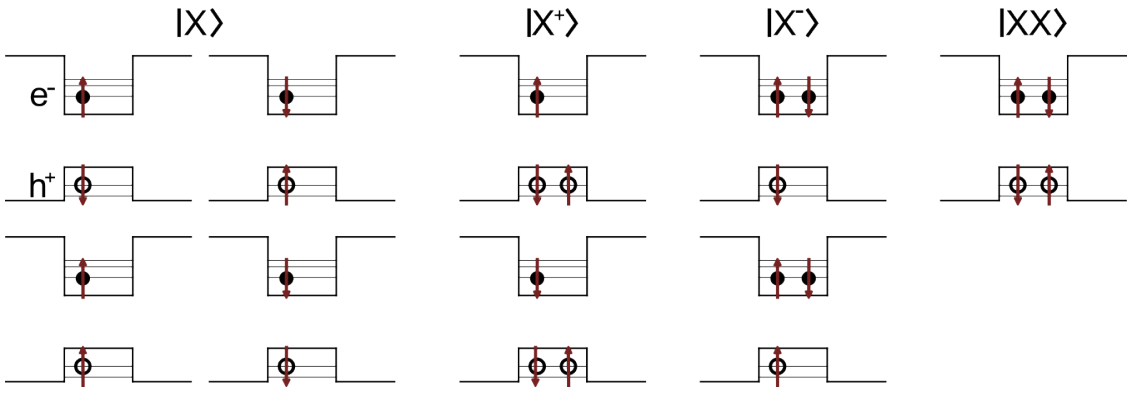

Figure 3.3. The s-shell of the *QD* can be occupied in various electron and hole configurations. Depending on the configuration, different nomenclatures are present. The most important for our applications are the bright X-states, top left, and the XX state, top right. The X state consists of an electron-hole pair and depending on the projection of the total angular momentum of the state, the emitted light after recombination of this electron-hole pair, is right ($M = +1$) or left ($M = -1$) polarized. The XX state consists of two electron-hole pairs emitting two entangled photons in polarization after cascaded recombination.

to attractive interaction between different particles. Using this information we can calculate the energies of the different complexes by simply accounting for the present electrons and holes and their interaction. This leads to the following energies of each complex:

$$\begin{aligned} E(X) &= [\epsilon(e) - \epsilon(h)] + W_{eh} \\ E(X^+) &= [\epsilon(e) - 2\epsilon(h)] + 2W_{eh} + W_{ee} \\ E(X^-) &= [2\epsilon(e) - \epsilon(h)] + 2W_{eh} + W_{hh} \\ E(XX) &= [2\epsilon(e) - 2\epsilon(h)] + 4W_{eh} + W_{ee} + W_{hh} \end{aligned} \tag{3.17}$$

with $\epsilon(i)$ the energy of a single electron or hole.

From these energies we can also extract the binding energy, which corresponds to the difference in transition energy between complexes to the transition energy of their individual components. The biexciton state, for example, is composited by two excitons, but the exchange between them introduces a binding term. We can write the energy of the biexciton state as $E(XX) = 2E(X) - \Delta_{binding}$, with $\Delta_{binding}$ the binding energy. Rewriting this expression and using Eq.(3.17) results to:

$$\Delta_{binding}(XX) = E(X) - (E(XX) - E(X)) = -2W_{eh} - W_{ee} - W_{hh} \tag{3.18}$$

The binding energy is hence responsible that the emission energy of the complex has a different energy than the emission energy of their individual components. For GaAs/AlGaAs *QDs* grown with molecular beam epitaxy the biexciton binding energy is approximately 4 meV [95]. Hence, the emission energy of the biexciton is roughly 4 meV lower than the exciton emission energy. We will see later that this binding energy will play an important role in the excitation of the *QD* system.

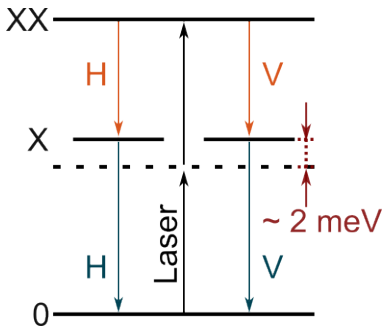

Figure 3.4. The XX-state has total angular momentum $M = 0$. When the first electron-hole pair recombines, it is either circular right or circular left polarized. The second electron-hole pair after recombination then emits a photon with opposite polarization. When the two paths are indistinguishable the two photons are perfectly entangled in polarization.

3.5 Entangled-photon emission from quantum dots

Before explaining the concept of entangled photon generation in *QDs* we simplify the electronic structure to the only two energy levels interesting for entangled-photon generation, the highest valence band, and the lowest conduction band level from the potential well model (see Figure 3.2). In this system, due to the Pauli exclusion principle, maximally two electrons with opposite spin can be excited from the valence band to the conduction band, leaving behind two holes. Consequently, the total angular momentum projection of the XX-state is $M = 0$. When two electron-hole pairs are generated in the *QD*, a radiative cascade from the XX-state through the X-state to the ground-state starts.

The generation of polarization entangled photon pairs from the XX-X-ground state cascade originates from the angular momentum states of the excitonic complexes and from the optical selection rules. The exciton is built up from an electron and a heavy hole. The polarization of the emitted photon is directly connected to the total angular momentum projection $M = S_{e,z} + J_{hh,z}$ of the recombining electron-hole pair by the optical selection rules: transitions with a momentum variation $\Delta M$of ± 2 are forbidden, while those with $\Delta M = -1(+1)$ result in the emission of right- (left-) circularly polarized photons. The biexciton state presents a symmetric linear superposition of the $M = +1$ and -1 angular momentum states due to the fact that the electron and heavy hole are in singlet states of angular momentum [96, 97] with null total angular momentum projection. In *QDs* with high structural symmetry, the bright excitons are double degenerate and characterized by $M = \pm 1$. The radiative cascade can take place via two equivalent decay paths, i.e., via the emission of a right- followed by a left-circularly polarized photon, or vice versa. Since the two decay paths are identical, as illustrated in Figure 3.4, the resulting two-photon state is entangled in polarization $\frac{1}{\sqrt{2}}(|R\rangle\,|R\rangle + |L\rangle\,|L\rangle)$, precisely in the maximally entangled Bell state

$$|\phi^+\rangle = \frac{1}{\sqrt{2}}(|H\rangle\,|H\rangle + |V\rangle\,|V\rangle). \tag{3.19}$$

3.5.1 Fine structure splitting

The real situation is quite different from the ideal scenario discussed before, in particular concerning the *QD* symmetry. Despite remarkable improvements in fabrication techniques, inevitable fluctuations in composition, size, shape, arrangement in the host matrix, and intermixing with the substrate and the cap material, make the fabrication of symmetric *QDs* a mere theoretical idea [98]. The deviation from an ideal *QD* with maximal symmetry to a real *QD* with lower symmetry induces an anisotropic electron-hole exchange interaction. This interaction leads to a coupling of the two bright excitonic states, the so-called *Fine Structure Splitting (FSS)* [99], which we need to account for in the total wave function of the state:

$$|\phi^+\rangle = \frac{1}{\sqrt{2}}(|H\rangle\,|H\rangle + e^{\frac{iSt}{\hbar}}\,|V\rangle\,|V\rangle) \tag{3.20}$$

t is the time between the emission of the biexcition photon and that of the exciton photon and S the energetic separation equal to the *FSS*. The energy difference between the two X states introduced by the *FSS* causes a precession during the intermediate step of the cascade. This quantity is indeterminate before detection, which in general leads to a mixed two-photon state with a reduced degree of entanglement, as quantified by the time-averaged fidelity to the maximally entangled Bell state [100]. The coupling noticeably affects the emitted two-photon entangled state, when the *FSS* is larger than the radiative linewidth of the exciton transition. GaAs *QDs* produced by droplet etching have an average *FSS* of 4.8 ± 2.4 μeV [101], and radiative linewidths of as low as ca. 5 μeV [36, 102], which is roughly twice the fourier transform-limited linewidth.
One can compensate for this drop of entanglement due to the time averaging from the measurement by employing time-resolved measurements. Time-resolved measurements use the information on the arrival time of the two different photons to retrieve a highly entangled state [103] reaching near-unity fidelities [104]. However, time-resolved measurements come with technical hurdles. First, the temporal resolution of the hardware (ca. 200 ps for *APDs*) used for detection needs to be well below the characteristic time of the precession, which is given by the Planck constant divided by the *FSS*, namely 4.135/S [μeV]. For the 4.8 μeV from before, for example, a timing resolution of ca. 140 ps would be necessary. Consequently, time-resolved measurements are achievable for small values of *FSS*. But obtaining this information becomes impossible in multiphoton experiments involving two-photon interference measurements or photon storage in quantum memories, which are our main applications stated in the introduction. In addition to that, in a projective Bell state measurement - a fundamental ingredient for quantum information protocols - the frequency detuning caused by the *FSS* can reduce the photon indistinguishably and therefore undermines the possible accuracy.
Another approach to retrieve highly entangled photons at the presence of *FSS*, is narrow spectral filtering of the *XX* and *X* photons [105]. Even though spectral filtering would be compatible for experiments involving two-photon interference measurements or quantum memories, it has to be emphasized that post-selection schemes inevitably induce severe photon-pair losses, that hamper on-demand generation of entangled photons and, more in general, the real possibility of using *QDs* for applications.
In contrast to post-selection schemes, external perturbations [106] such as electric [107] magnetic

[100] and strain [108] fields, provide the possibility to compensate for the *FSS* by directly modifying the *QD* electronic structure.

3.5.2 Excitation methods for entangled-photon generation

Light emission from a semiconductor can be induced by different methods, i.e. catholuminescence (high-energy electron beam), electroluminescence (electric current) or photoluminescence (light). Even though electrical pumping is by far the most desirable excitation method for application in compact devices, photoluminescence provides an exact control on the excitation energy and polarization of the injected carriers. Consequently, it allows to access precise information on the energy levels and the recombination dynamics. For this reason, we focus on the various methods of photoexcitation.

If a photon, with an energy higher than the bandgap, impinges on a semiconductor material, it gets absorbed and transfers its energy to an electron in the crystal potential. This electron is elevated to the conduction band of the semiconductor material, leaving behind a hole in the valence band. This electron-hole pair, bound by Coulomb interaction, after thermalization due to interactions with the lattice and other carriers, can undergo radiative recombination. In this process, the system returns into the electronic ground state by emitting a photon corresponding to the energy difference.

There are different strategies to populate a *QD* by generating an electron-hole pair. The most intuitive is above-band excitation. Similar as explained before, an energy source with an energy above the barrier bandgap is utilized to generate many electron-hole pairs in the barrier, which are in a highly non-equilibrium state. These carriers then decay to the minimum (maximum) of the conduction (valence) band, by interacting with the electrons and phonons of the lattice. During this, they can be captured by a *QD* acting as a potential well. If so, the electron-hole pair thermalizes to the lowest level, faster than interband transitions of roughly $\sim$ 10-100 ps [109]. The electron-hole pair spontaneously recombines within the radiative lifetime of the state and emits a photon corresponding to the energy difference of the confined levels near the conduction and valence band. Above-band excitation does not deterministically create a single confined electron-hole pair in the *QD*, but rather occupies several *QD* levels following a Poissonian distribution [110]. In this way, excitonic complexes at various energies are generated starting from the possible combinations in the s-shell and extending to higher energy shells, if present, see Figure 3.5. To deterministically populate the *QD* with an electron-hole pair, a different excitation method must be utilized, called resonant excitation. Therefore, a pulsed laser is resonantly tuned to the *X* transition, generating an electron-hole pair in the *QD*. Resonant excitation, however, only allows for the generation of single photons in the *QD*. We, on the contrary, are interested in the deterministic generation of two photons that are entangled in polarization. This can be achieved using resonant two-photon excitation.

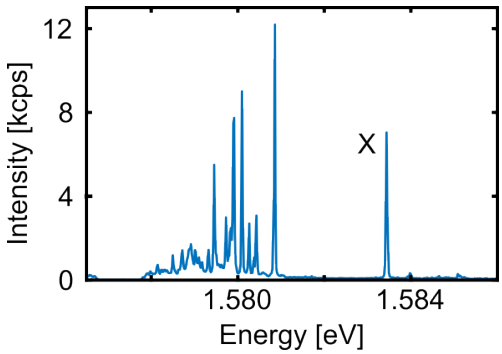

Figure 3.5. Micro-photoluminescence spectrum of a GaAs *QD* under non-resonant above-band excitation. The neutral exciton emission line is labeled as *X*. The biexciton line *XX* lays within the bundle of emission lines at lower energy.

Resonant two-photon excitation

A way to resonantly excite the biexciton state under compliance with the electric-dipole selection rules consists in using a two-photon absorption process [111, 112]. The laser energy is therefore set between the *X* and *XX* emission energy and, in *QDs* with a sufficiently large and positive biexciton binding energy, it cannot directly populate the *X* state. Additionally, the probability of populating other states or charge configurations is also drastically reduced. The resulting spectrum is shown in Figure 3.6. The excitation laser, laying between the *X* and *XX* energies is largely suppressed by narrow band stop filters.
The resonant excitation process is clearly visible when changing the excitation power. The radiative cascade undergoes Rabi oscillations, indicating the population and depopulation of the *XX* state. The probability of successfully preparing the biexciton state and hence, initiating the radiative cascade is referred to as preparation fidelity. The maximum preparation fidelity is given at π-pulse excitation, which corresponds to the laser power needed to maximize the state population. The preparation fidelity η_{prep} can be estimated by an indirect method using the Rabi oscillations. In this method, the preparation fidelity can be estimated as a ratio between the intensity at π-pulse and the intensity at zero laser power, extrapolated with an exponential fit of the oscillation maxima. For GaAs *QDs* the preparation fidelity has already been experimentally shown to be as high as 94 % [23], thus going towards the direction of almost deterministic entangled-photon emission. To properly reproduce the actual Rabi oscillations and their damping due to coherence losses a more refined model may be required.

Phonon-assisted two-photon excitation

To complete this section, it is important to mention that there exists another effective method to pump the biexciton state: Phonon-assisted two-photon excitation. In this scheme the excitation laser is detuned to higher energy, with respect to the two-photon resonant excitation energy, to address the acoustic vibrational modes coupled to the biexciton state. The exact detuning for optimal state preparation is determined by the *QD* structure and the surrounding material deformation potential. [113] In contrast to the strict two-photon excitation, this scheme provides a stable population probability for fluctuating excitation laser power. However, if one aims at simultaneously

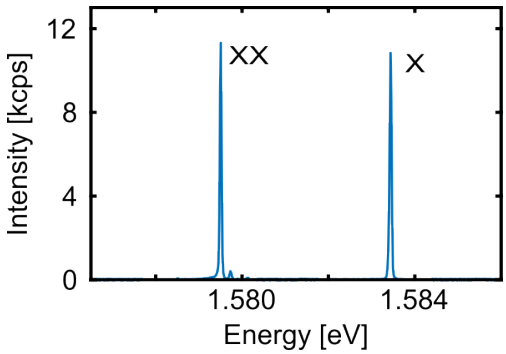

Figure 3.6. Micro-photoluminescence spectrum of a GaAs *QD* under resonant two-photon excitation. The laser is set to half the *XX* energy. This does not correspond to the *X* energy due to the different Coulomb binding for these states. The resonant excitation of the *XX* state with *TPE* occupies mainly this state, resulting in the emission of an *XX* photon, followed by an *X* photon, which is clearly visible in the spectrum.

optimizing the degree of entanglement, photon indistinguishability, single-photon purity, and on-demand generation, two-photon resonant excitation has so far proven to be the best solution and is thus often used for entangled photon generation in *QDs*.

3.5.3 Extraction efficiency

Using resonant two-photon excitation, *QDs* can in principle generate deterministic photon pairs close to unity efficiency without negatively influencing the entanglement fidelity [25, 114]. The main limiting effect for brightness in semiconductor *QDs* is a small extraction efficiency, related to the fact that *QDs* are embedded in a host matrix, like GaAs or AlGaAs, which typically has a high refractive index n, e.g. 3.5 in GaAs.

A common definition of the brightness of the source, among the wide range, is the probability of collecting a single photon with the first lens of the collection optics upon an excitation pulse [115]. Consequently, we can estimate the brightness of the source in the following way: The first aspect to be considered that determines the brightness of a pulsed entangled photon source is the probability that an excitation pulse successfully triggers the emission of a photon pair from the *QD*. This quantity depends on a few factors, namely on the probability of creating a biexciton state – which, for a resonant excitation method, depends on the probability that the system starts in the designed initial ground state multiplied by the probability that excitation promotes the system to the biexciton state – and on the weight of the two-photon cascade with respect to other non-radiative decay cannels, if present. The analysis and modeling of Rabi oscillations in two-photon resonant excitation suggest that QDs in an optically active ground state can be excited to the biexciton state with near-unity efficiency [114]. A more direct assessment of the overall photon pair emission is by comparing coincidence events to single channel count rates [116]. A photon pair emission can be triggered with high probability under resonant two-photon excitation, up to an observed value of 94.3 % accounting for the success of the two-photon absorption mechanism and non-radiative losses [23], but not for the probability that the system starts in the designed initial ground state. This topic will be discussed in more depth in chapter 5.1.2. Consequently, the

brightness is limited for planar as-grown samples due to the second aspect to be considered, the extraction efficiency. The extraction efficiency is the fraction of the emitted signal from the *QD* that can be collected with the detection instrument. Total internal reflection allows only a small fraction $\frac{1}{4n^2}$ of the emitted light to have the chance of exiting the sample [89]. Taking into account the finite numerical aperture of the collection optics and interface reflection, generally, only less than 1 % of the emitted light can be collected from the top surface of planar unprocessed samples [89].

Over the years, several methods have been employed to improve the brightness of QD-based sources. One method is based on solid immersion lenses. With the use of a Weierstrass sphere with $n = 1.88$ and a collection system NA of about 0.53, a theoretical extraction efficiency of up to 11 % can be achieved [90], however with the unrealistic assumption of perfect transmission at all interfaces. For a semi-spherical solid immersion lens with n = 3.5 and a collection system numerical aperture of about 0.42, an extraction efficiency of 65(4) % was recently demonstrated [117]. A second approach is based on photonic structures that embed the *QDs* in a planar lambda-cavity either defined by *DBR*, metal mirrors or a hybrid *DBR*/metal mirror system. The mirrors define an optical cavity designed to enhance the coupling between the emitter and a specific electromagnetic mode that couples into the far field beyond the top surface of the sample with the goal of improving the directionality of the spontaneous emission [90]. Figure 3.7 illustrates an example of the combination of a glass-made solid immersion lens with a *DBR* structure to enhance the extraction efficiency. However, the single-photon extraction efficiency, with measured values of approximately 12 %, is still relatively modest [33]. Higher extraction efficiencies are achieved using more elaborate photonic cavities, for example, micropillars. By fabricating an additional lateral optical confinement via etching from the planar cavity, the single-photon extraction efficiencies can reach up to 79 % [118]. Even though these microcavities achieve high extraction efficiencies for single photons, they are less suitable for entangled photon pair generation as the energy difference between the biexciton and exciton typically exceeds the resonance width of these cavities. Consequently, enhancing the extraction efficiency of entangled photon sources is mainly feasible with cavities that have a broadband extraction efficiency and moderate Purcell factor. The purcell factor quantifies the enhanced radiative rate of an emitter within a microcavity relative to its rate without. In this context, second-order Bragg gratings, also called bullseye cavities [119], are particularly promising. There, a microstructure is accurately patterned around selected single *QDs*. As a result, photons emitted by the *QD* in the center of the second-order Bragg grating will be directed perpendicular to the concentric trenches. When combining these bullseye cavities with highly efficient broadband reflectors, a single-photon extraction efficiency of 85(3) % has been achieved. The same structure with GaAs *QDs* exhibits an entangled photon pair collection probability per excitation pulse of 65(4) % [29].

3.5.4 Indistinguishability

Numerous applications in photonic quantum technologies rely on quantum interference of deterministically generated single or entangled photons. Such schemes include Bell state measurements [120], quantum teleportation [121], post-selective production of polarization-entangled photons

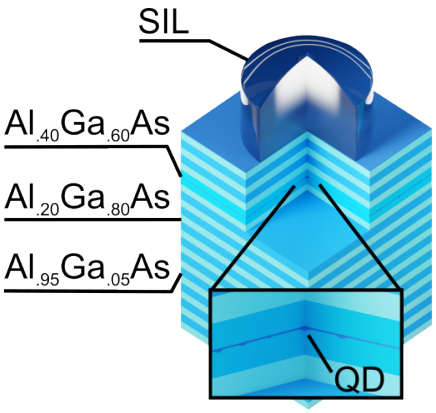

Figure 3.7. The GaAs *QDs* are embedded in distributed Bragg resonantors (blue and light blue alternating layers) to guide the emission to the top of the sample structure. Additionally, a solid immersion lens is placed on the top surface, to increase the light collection angle.

[122], linear-optics quantum computation [123], and boson-sampling [124]. As we saw previously in Section 2.3.1, the correct outcome of a *BSM* depends on the degree of indistinguishability of the incoming photons and the spatial and temporal overlap of the wave packets. Two photons are indistinguishable if they are identical in their spectral, spatial, and polarization modes [125]. The photon indistinguishability can be verified by measuring the two-photon interference visibility in a *HOM* experiment [76]. The experimental implementation of a *HOM* experiment for co-polarized and cross-polarized measurements is explained in Section 4.5. Using this approximation, a raw *HOM* visibility to about 0.65 is extracted. A more accurate way of estimating the *HOM* visibility is by performing co- and cross-polarization measurements. Visibilities up to $V_{raw} = 0.95(5)$ for a GaAs *QD*, as used in this thesis, operated as on-demand single-photon source were achieved, without the need for any enhancement technique such as microcavities [126]. However, the excitation technique used to achieve such a result, namely cross-polarized pulsed resonance fluorescence, is incompatible with entangled photon pair generation, as resonant two-photon excitation is needed to coherently populate the biexciton state.

Under resonant two-photon excitation the coincidence counts at zero-time delay indicate a non-perfect indistinguishability between the two interfering photons. This is caused by many factors [127], namely time jittering [128], phonon-induced dephasing [129], fluctuating magnetic, electric fields [130, 131], and time-energy entanglement introduced by the three-level system [132]. Decoherence introduced by time jittering is caused by non-resonant or quasi-resonant excitation schemes [128, 133] because the stochastic relaxation process from a higher excited state to the lowest-energy level via non-radiative processes leads to an uncertainty in the emission time, which degrades the indistinguishability. Therefore, time jittering can be largely neglected in our case, because it can be overcome by using resonant excitation [134]. Phonon-induced dephasing, on the other hand, results from the inevitable coupling of the *QDs* to the vibrational modes of their host lattice. Inelastic exciton-phonon scattering produces detuned, distinguishable photons in sidebands by exchanging energy with the *QD* [135]. Also, elastic phonon-exciton scattering through virtual excitations introduces a broadening of the zero-phonon line, which decreases the photon indistinguishability [136].

The latter can be mitigated by operating the source at lower temperatures than the characteristic phonon energies. Additionally, phonon-induced effects can be significantly reduced by embedding the *QD* in a photonic cavity that selectively enhances zero-phonon emission processes through the Purcell effect [137]. Charge and spin noise, the last predominant indistinguishability degradation mechanism in *QDs*, mainly arises from random occupations of the available electronic states in the surroundings of the confined excitons and interaction with the spin of the nuclei, which leads to fluctuations in the local electric field. This can induce shifts in the optical transition energy of a nearby *QD* through the quantum confined Stark effect and can induce spin dephasing through the spin-orbit interaction [130]. The quantitative impact depends on many factors such as the materials system and the exact growth conditions during fabrication. The effect of charge noise on the emission linewidth of the *QD* depends on the optical transition, i.e., the exciton and biexciton transition in *QDs* have a different sensitivity to charge noise [138]. Charge noise can significantly increase the linewidth of self-assembled QDs above the natural linewidth limit and, thus deteriorating the achievable indistinguishability. One strategy to mitigate or even suppress the undesired linewidth broadening caused by charge noise is to embed the *QD* in a p-i-n diode structure, which allows to control the charge occupation inside the *QD* [139]. It should be mentioned that slow fluctuations in the local magnetic field or fluctuations in nearby crystal impurities do not necessarily affect the indistinguishability of photons emitted subsequently from the same source [138, 140]. However, they do affect indistinguishability between photons from different *QDs*. The last effect that we need to discuss is peculiar to the cascaded photon emission from a three-level ladder, such as the biexciton-exciton decay. The photons—even when having perfect coherence—exhibit an upper bound for the indistinguishability. The maximum achievable *HOM* visibility in the three-level system is defined by the lifetime ratio between the biexciton and exciton states, a factor 1/2 for GaAs *QDs*, and is limited to about 66 % [132]. In order to reach the dephasing-limited indistinguishability values with photons stemming from a three-level system, as demonstrated in a resonantly driven two-level system, the lifetime-ratio between the two excited states has to be modified. Therefore, asymmetric Purcell enhancement of the two states could overcome this limitation. Improved photon indistinguishability was indeed recently demonstrated using second-order Bragg gratings [29, 30]. In particular, Liu et al. [29] reported values of indistinguishability of 0.901(3) and 0.903(3), for exciton and biexciton photons, respectively.

Chapter 4

Measurement techniques and sample structure

4.1 Visible and infrared photoluminescence spectroscopy

Photoluminescence is a valuable tool to characterize semiconductor *QDs* in terms of their structure, which is responsible for their single- and entangled-photon quality. Spectroscopy, in particular, enables studies on the excited electronic states of the system. In detail, the recombination dynamics of the carriers is visualized when combining spectroscopy with different sample temperatures or excitation powers.

The photoluminescence setup is schematically illustrated in Figure 4.1. To excite the semiconductor structures various laser sources can be selected. For above-band excitation either a green Nd:YVO_4 continuous wave laser at 532 nm with an output power up to 4 mW or a HeNe continuous wave laser at 633 nm with an output power up to 12 mW is employed. The power is regulated by a neutral density filter wheel in the excitation beam path to adjust the optimal density of excited carriers. The above-band laser can be interchanged with a white light lamp, often used for stabilizing the electronic surrounding of the *QD*. For two-photon excitation a Ti:Sapphire femtosecond laser (Coherent) with a repetition rate of 80 MHz and a pulse width of around 200 fs, with tunable wavelength (690 - 1040 nm), is implemented. The spectral width of the excitation pulses is reduced by a custom 4f pulse-shaper, broadening the 200 fs to about 10 ps pulse length. The different excitation lasers are coupled to one excitation path with a dichroic mirror. The lasers are then coupled into the common excitation/detection path by a 90:10 beam splitter, where 10 % of the laser signal is reflected and then focused on the sample through a 0.81 numerical aperture objective (LT-APO/IR, Attocube), which are both placed inside a closed-cycle He cryostat. The laser spot size, with a diameter of approximately 0.5 μm, generating electron-hole pairs in the *QD*. The photoluminescence, after the recombination of the generated electron-hole pairs, is again collected via the same objective and 90 % of the signal is transmitted into the detection beam path by the 90:10 beam splitter. The photoluminescence signal then directly enters a 750 mm focal length spectrometer (Prinsceton Instruments) to be dispersed by one of the exchangeable diffraction gratings of

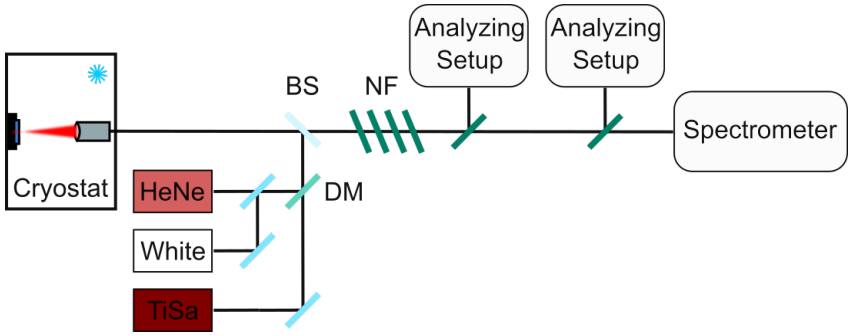

Figure 4.1. The optical spectroscopy setup is split in two main parts, the excitation path and the detection path. The excitation path consists of three different light sources, a Ti:Sapphire (Ti:Sa) laser for *TPE*, a green laser for above-band excitation, and a white light source. The green and white light illumination can be interchanged by placing a magnetic mirror. Then both are coupled into the same excitation path as the Ti:Sa laser via a dichroic mirror (DM). All excitation lasers are coupled into the common excitation/detection path via the reflection of a 90:10 beam splitter (BS). Afterwards the excitation is focused on the sample, which is placed inside a 4 K closed-cycle cryostat, using an objective. The emitted light is collected by the same objective and 90 % is sent to the detection path by the transmition of the 90:10 BS. The backscattered laser light is cut out in the detection path by using multiple *NFs*. The signal from the *QD* can either be spectrally selected via the reflection of additional *NFs* and sent to one of the analysing setups, or sent directly to the spectrometer.

(300/1200/1800 g/mm), and analyzed by a CCD camera (PyLon). With this system the spectral resolution for the analyzed wavelengths of 700 - 800 nm is roughly 40 μeV. Confocal imaging of the *QD* photoluminescence is assured by coupling the photoluminescence signal, prior to entering the spectrometer, into a single mode fiber with a 5 μm core acting as a pinhole. This assures the collection of photoluminesence of only one, or at worst a few *QDs*. As a third option, single spectral lines can be selected using *Notch Filters (NFs)* with 0.4 nm bandwidth in reflection. This option is mainly chosen to separately analyze specific emission lines of the *QD*.

Additionally to the spectral division of the emitted light, polarization-dependent spectra can be acquired by adding a polarizer and a motorized half-wave plate within the detection path. For example, the *FSS* introduces an energy shift in the *X* and *XX* line when probing for different polarizations. A LabVIEW program synchronizes the motorized rotation of the waveplate with a spectral acquisition. Several spectra for different linear polarization settings are acquired. The *X* and *XX* emission lines are then fitted with a Gaussian line shape to estimate the line center. One example of extracted line centers of a *X* emission line for different polarization settings is shown in Figure 4.2. The energy shift, induced due to the *FSS* and detected by the polarization-selected analysis, is then fitted with a sinusodial function. *FSSs* with an accuracy down to 1 μeV can be detected.

Further to the spectral resolution and polarization-dependent measurement, the same system can be used to estimate the population of the excited states, giving an approximation for the population probability, called the preparation fidelity of the *QD*, as defined in Section 3.5.2. The *QD* can be simplified to a three-level system, as illustrated in Figure 3.4. A three-level system, similar to a two-level system undergoes Rabi oscillations, when changing the excitation power. In a nutshell, the excitation laser can modify (populate/depopulate) the excited states coherently. To

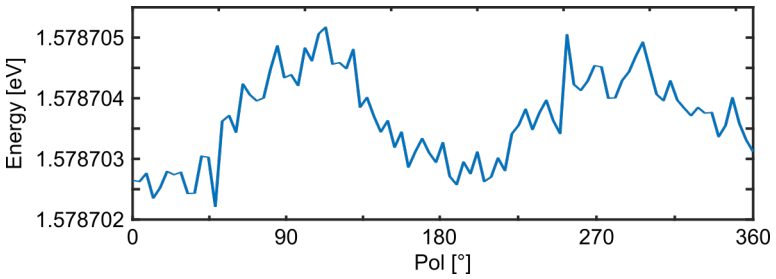

Figure 4.2. The spectral position of the *X* peak oscillates for different linear polarization-angles. This polarization dependent energy fluctuation is called *FSS*. The amplitude of the oscillation refers to the amount of the splitting, which is 1.8 μeV for this *QD*.

visualize the Rabi oscillations, a LabVIEW program synchronizes a power-ramp with the acquisition of a spectrum for every power step. The presence of the Rabi oscillations can then be deduced from the photoluminescence intensity, which gives information on the population of the excited state.

4.2 Lifetime measurements

The same spectroscopy setup is used to perform lifetime measurements of the different excitonic transitions in the *QD*. The emitted signal is again sent into the spectrometer. This time, though, the signal is not directly sent to the CCD camera. The selected grating, in our case the 1200 g/mm, disperses the signal in different wavelengths which allows to select specific emission lines of the *QD*. By turning the grating a specific wavelength is centered onto the side output port of the spectrometer. Opening and closing the side output port slit lets us select more or less of the chosen spectral distribution of the *QD* signal. For the lifetime measurements we fully open the slit and turn the grating to select the *X* or *XX* line. The signal exiting the side output port is sent to a fast *APD* using multiple mirrors. This fast detection, with time jittering of roughly 70 ps, allows to collect time traces of the emitted light, with respect to time of generation of the excitation laser pulse. A TimeTagger Ultra (Swabian Instruments) and their software package allow to convert the TTL signal, generated by the detector to mark detection events, into digital time stamps and extract the time traces. A sketch of the analyzing setup is shown in Figure 4.3. The lifetime is then extracted from the data by fitting it with the convolution of the instrument response function and a single exponential decay. This analysis assumes that only one radiative recombination channel is present.

4.3 Auto-/Cross-correlation measurements

The second-order correlation function $g^{(2)}(\tau)$ is an important measure for the characterization of single photon emitters. A *Hanbury-Brown and Twiss (HBT)* setup enables the evaluation of this quantity based on coincidences at different time delays.

The *HBT* setup consist of a 50:50 beam splitter with an *APD* at each of the two output ports of the beam splitter (see Figure 4.4). The two detectors are then connected to a fast electronics

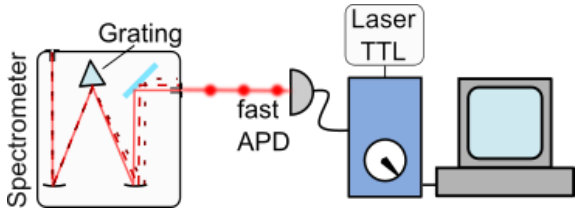

Figure 4.3. Lifetimes of the X and XX states are measured via a fast APD. First, the X or XX signal is spectrally selected by tuning the grating of the spectrometer to reflect the correct wavelength onto the side output port of the spectrometer. Afterwards it is sent onto the fast APD chip, which is connected to a time-to-digital converter. By manually opening or closing the exit slit different spectral distributions of the QD can be analyzed.

correlation system, TimeTagger Ultra (Swabian Instruments), that registers time traces between individual detection events. For auto-correlation measurements, the photons emitted from the QDs are spectrally filtered. Then the X or XX signal is sent to a 50:50 beam splitter and is detected by two $APDs$ one placed at each output port of the beam splitter. During a measurement set, the correlations between the two $APDs$ are registered. Since the QD emits per excitation cycle one X (XX) photon and we excite the QD every 80 MHz in *Two-Photon Excitation (TPE)*, we expect a train of photons arriving on the beam splitter with a time spacing of 12.5 ns. The beam splitter randomly sends the photon either to the APD on the transmitted or reflected path, where they are detected and converted by the coincidence counter. If we are looking at a single-photon source, by definition, only one photon per excitation pulse is emitted. This should result in a detection event on only one of the two $APDs$ for any single excitation temporal window. But at a time delay of a multiple of 12.5 ns the system is re-excited by the pulse train of the excitation laser and a detection of a photon on the second detector is plausible. Consequently, the correlations between the detectors at zero-time delay are expected to be 0, whereas at time delays of multiple of the repetition rate of the excitation laser correlations are expected. Another mechanism that auto-correlation measurements study is the blinking characteristics of QDs. Blinking is the intermittent emission behavior of a QD, which is quantified by its on-time fraction or duty cycle. The measurement then determines how likely it is that the QD is in its neutral ground state and can be excited to a higher state using one of the several excitation techniques.

Cross-correlation measurements, on the contrary to auto-correlation measurements, are coincidence measurements between different emission lines, for example the X and XX line, in the QD. Here the X and XX are spectrally selected and sent to an APD each, which is then correlated by the TimeTagger Ultra (Swabian Instruments). In practice, the same setup as for the auto-correlation measurements can be used. But, in this case, the two detectors on the two outputs of the HBT beam splitter need to be considered as a single channel. The rest of the measurement is the same. These cross-correlation measurements allow to extract the preparation fidelity. This is explained in detail in Section 5.1.2. Despite the preparation fidelity, cross-correlations also enable characterizations if specific QD transitions are present simultaneously (within the same radiative cascade), or if a certain transition is only present in the case another is not. The latter case is interesting, when studying emission lines close to the XX or X transition. For example, closely adjacent in energy to

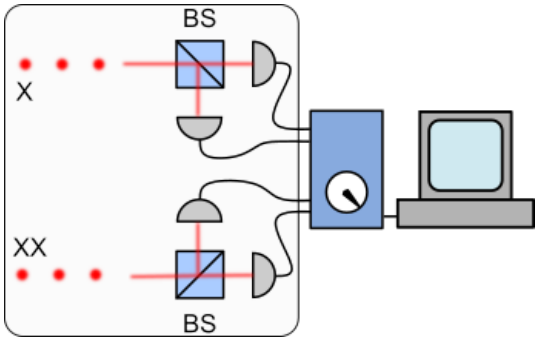

Figure 4.4. Auto- and Cross-correlations of X and XX. First the different emission lines are spectrally selected via the different reflection angles on the *NF*. For the auto-correlation measurement each selected line is sent through a beam splitter (BS) and the correlations between the *APDs* located at the two output ports of the BS are collected. For the cross-correlation measurement the signal of the different lines are directly sent onto the *APDs* and correlated with each other.

the XX there is an emission line, which is not emitting at the same time as the XX.

4.4 Quantum state tomography

In some applications it is interesting to exactly know the full quantum state of the investigated system. However, a measurement on a single quantum particle perturbs its state, making its further investigation uninformative. Quantum state tomography tackles this challenge by performing a series of measurements in different bases on a statistics of particles generated in the same quantum state.

A single-*qubit* in a pure state can be represented by Eq. (2.2). This representation is enough to describe the action of any operator, i.e., unitary rotations, on a pure state, or to carry out tomography on that state. However, when considering an open system the *qubit* can get entangled with the environment. To fully describe its state this requires a representation in form of a density matrix. A density matrix representation is also essential when measuring ensembles of states, which can all be in a different quantum state or altered due to measurement or setup imperfections. In this case, the overall state is mixed. How mixed a state is can be determined by the trace of the density matrix ρ, where $Tr(\rho^2) = 1$ denotes a pure states and $Tr(\rho^2) < 1$ the mixture.
Mixed states are described by a probabilistically weighted incoherent sum of pure states. For example, mixed states behave as if any particle in the ensemble has a specific probability of being in a given pure state, which is distinguishable in some way. In case the individual particles are not distinguishable, they would add coherently with a definite relative phase, yielding a single pure state.
A mixed state is described mathematically with a matrix, the density matrix ρ:

$$\rho = \sum_i P_i \left|\phi_i\right\rangle \left\langle\phi_i\right| = \begin{pmatrix} A & Ce^{i\phi} \\ Ce^{-i\phi} & B \end{pmatrix} \tag{4.1}$$

P_i are the probabilities for the system to be in one of the spanning states $|\phi_i\rangle$, constrained

by $\sum_i P_i = 1$. A, B and C are all real and non-negative coefficients, and ϕ a phase between the two states. Note, A and B are not independent due to normalization and hence, leaving three independent parameters to describe the system.
Any ensemble of single-*qubit* states can be represented by an ensemble of only two orthogonal pure states $|\phi_i\rangle$, $|\phi_j\rangle$ with $\langle\phi_i|\phi_j\rangle = 0$ (orthogonal). Hence, the state is a probabilistic combination of two orthogonal states, which leads to the matrix being diagonal such that

$$\begin{pmatrix} E_1 & 0 \\ 0 & E_2 \end{pmatrix} = E_1 \left|\phi\right\rangle \left\langle\phi\right| + E_2 \left|\phi^{\perp}\right\rangle \left\langle\phi^{\perp}\right| \tag{4.2}$$

where $\{E_1, E_2\}$ are eigenvalues of ρ and $\{\left|\phi\right\rangle, \left|\phi^{\perp}\right\rangle\}$ the eigenvectors. Consequently, the representation of any quantum state, is identical to that of an ensemble of two orthogonal pure states.

Example using qubits

In the course of this thesis we use *qubits* encoded in the polarization of photons. For single photons this system has two bases, horizontal ($|H\rangle \equiv |0\rangle$) and vertical ($|V\rangle \equiv |1\rangle$), with all possible pure polarization states constructed from coherent superpositions of these two states. For example, diagonal ($|D\rangle$), antidiagonal ($|A\rangle$), right-circular ($|R\rangle$) and left-circular ($|L\rangle$) are represented by

$$\begin{aligned} |D\rangle &\equiv \frac{1}{\sqrt{2}}(|H\rangle + |V\rangle) \\ |A\rangle &\equiv \frac{1}{\sqrt{2}}(|H\rangle - |V\rangle) \\ |R\rangle &\equiv \frac{1}{\sqrt{2}}(|H\rangle + i\,|V\rangle) \\ |L\rangle &\equiv \frac{1}{\sqrt{2}}(|H\rangle - i\,|V\rangle) \end{aligned} \tag{4.3}$$

Any single-*qubit* density matrix ρ can be uniquely represented by three parameters $\{S_1, S_2, S_3\}$, the Stokes parameters:

$$\rho = \frac{1}{2}\sum_{i=0}^{3} S_i \hat{\sigma}_i \tag{4.4}$$

with $\hat{\sigma}_i$ being the Pauli-matrices

$$\hat{\sigma}_0 \equiv \begin{pmatrix} 1 & 0 \\ 0 & 1 \end{pmatrix},\ \hat{\sigma}_1 \equiv \begin{pmatrix} 0 & 1 \\ 1 & 0 \end{pmatrix},\ \hat{\sigma}_2 \equiv \begin{pmatrix} 0 & -i \\ i & 0 \end{pmatrix},\ \hat{\sigma}_3 \equiv \begin{pmatrix} 1 & 0 \\ 0 & -1 \end{pmatrix} \tag{4.5}$$

and the S_i values given by

$$S_i \equiv Tr\{\hat{\sigma}_i \rho\} \tag{4.6}$$

Each of these parameters directly corresponds to the outcome of a specific pair of projective

measurements:

$$\begin{aligned} S_0 &= P_{|H\rangle} + P_{|V\rangle} \\ S_1 &= P_{|D\rangle} - P_{|A\rangle} \\ S_2 &= P_{|R\rangle} - P_{|L\rangle} \\ S_3 &= P_{|H\rangle} - P_{|V\rangle} \end{aligned} \tag{4.7}$$

with $P_{|\psi\rangle}$ the probability to measure the state $|\psi\rangle$. Note, that the set of the three orthogonal basis states describing the Stokes parameters are chosen to be $|\psi_1\rangle \equiv |D\rangle$, $|\psi_2\rangle \equiv |R\rangle$ and $|\psi_3\rangle \equiv |H\rangle$.

This theory can be extended in a more general manner. We can define parameters similar to these and serving the same function with respect to any three arbitrary states, ψ_i, as long as the matrices $|\psi_i\rangle\langle\psi_i|$ along with the identity are linearly independent.
We can define operators analogous to the σ operators relative to these linearly independent states:

$$\tau_i \equiv |\psi_i\rangle\langle\psi_i| - |\psi_i^{\perp}\rangle\langle\psi_i^{\perp}| \tag{4.8}$$

And additionally, we can define an S-like parameter, T:

$$T_i \equiv Tr\{\tau_i \rho\} \tag{4.9}$$

Note that the S_i parameters are simply a special case of the T_i parameters, for the case when $\tau_i = \sigma_i$. Using these parameters, we can see that

$$\begin{aligned} T_{i=1,2,3} &= P_{\psi_i} - P_{\psi_i^{\perp}} \\ T_0 &= P_{\psi} - P_{\psi^{\perp}} = 1 \end{aligned} \tag{4.10}$$

In order to reconstruct the density matrix from T parameters they first have to be transformed into the S parameters. However, in our case this is not necessary, since we will always choose the basis of our states to be in the σ_i case.

The probability of projecting a given state ρ in the state $|\psi\rangle$, which is the probability of measuring $|\psi\rangle$ is given by [141]:

$$\begin{aligned} P_{|\psi\rangle} &= \langle\psi|\,\rho\,|\psi\rangle \\ &= Tr\{|\psi\rangle\langle\psi|\,\rho\} \end{aligned} \tag{4.11}$$

Using Eq. (4.11) and Eq. (4.10) we exactly obtain the Stokes parameters from Eq. (4.7), except written in a more generalized formula, which will be of use in the multiple-*qubit* case.

Example using multiple-qubits

Transforming now to the representation of multiple *qubits* means constructing the multiple-*qubit* states out of individual *qubits*. The Hilbert space of a many *qubit* system is spanned by state vectors which are the tensor product of single-*qubit* state vectors, with the example of a two-*qubit* pure state of Eq. (2.3).

We have previously seen that moving to multiple states discloses the concept of entanglement. Bell states as in Eq. (2.4) are an example of entangled pure states. Noise, related to the measurements or sample imperfections, can be accounted for in the density matrix formalism by extending the model to Werner states [142]:

$$\rho_W = P\left|\gamma\right\rangle\left\langle\gamma\right| + (1-P)\frac{1}{4}\mathbb{I} \tag{4.12}$$

with $|\gamma\rangle$ being a maximally entangled state and $\frac{1}{4}\mathbb{I}$ the totally mixed state. The latter is a matrix that has solely elements on the diagonal with equal contribution. In contrast to a pure state ($Tr(\rho^2) = 1$), the mixed state follows the criterion $Tr(\rho^2) < 1$.

As before, the general mixed state is an incoherent sum of pure states, however, now represented a 2^n-by-2^n density matrix:

$$\rho = \sum_{i=1}^{2n} P_i\left|\phi_i\right\rangle\left\langle\phi_i\right| \tag{4.13}$$

where ϕ_i are orthogonal ($\langle\phi_i|\phi_j\rangle = \delta_{ij}$) and the amount of linear independent vectors is limited to 2^n vectors.

A general two-*qubit* polarization state can be written in the $|HH\rangle$, $|HV\rangle$, $|VH\rangle$, $|VV\rangle$, as

$$\rho = \begin{pmatrix} A_1 & B_1 e^{i\psi_1} & B_2 e^{i\psi_2} & B_3 e^{i\psi_3} \\ B_1 e^{-i\psi_1} & A_2 & B_4 e^{i\psi_4} & B_5 e^{i\psi_5} \\ B_2 e^{-i\psi_2} & B_4 e^{-i\psi_4} & A_3 & B_6 e^{i\psi_6} \\ B_3 e^{-i\psi_3} & B_5 e^{-i\psi_5} & B_6 e^{i\psi_6} & A_4 \end{pmatrix} \tag{4.14}$$

with A_i, B_i the coefficients and ψ_i being the phases between the different bases with $\{i = 1, 2, ..., 6\}$ for the different bases. ρ is positive and Hermitian with unit trace.

As for the single-*qubit* density matrix representation, also the n-*qubit* state ρ can be represented in terms of n-*qubit* Stokes Parameters:

$$\rho = \frac{1}{2^n}\sum_{i_1,i_2,...,i_n=0}^{3} S_{i_1,i_2,...,i_n}\sigma_{i_1}\otimes\sigma_{i_2}\otimes ...\otimes\sigma_{i_n} \tag{4.15}$$

Normalization requires $S_{0,0,...,0} = 1$, leaving $4^n - 1$ real parameters to identify any point in the Hilbert space. This is analogous to the three parameters that determine the exact position of a

one-*qubit* state on the Poincare sphere. For a two-*qubit* Hilbert space, already 15 independent real parameters are needed to describe the exact state.
For two *qubits* the link between the two-*qubit* Stokes parameters and measurement probabilities still holds. Also the formalism of τ operators holds for larger *qubit* systems [143], so that

$$T = Tr\{\tau\rho\}$$

Extracting τ is more difficult in the case of a multiple-*qubit* system. We need to resort to local measurements on a single *qubit* in the multi-*qubit* system. This means we first project *qubit* one along τ_{i_1}, and then *qubit* two along τ_{i_2}. Consequently, we can write $\tau = \tau_{i_1} \otimes \tau_{i_2} \otimes ... \otimes \tau_{i_n}$ and hence,

$$\begin{aligned} T_{i_1,i_2,...,i_n} &= Tr\{(\tau_{i_1} \otimes \tau_{i_2} \otimes ... \otimes \tau_{i_n})\rho\} \\ &= \frac{1}{2^n} \sum_{j_1,j_2,...,j_n=0}^{3} Tr\{\tau_{i_1}\sigma_{j_1}\}Tr\{\tau_{i_2}\sigma_{j_2}\}...Tr\{\tau_{i_n}\sigma_{j_n}\}S_{j_1,j_2,...,j_n} \end{aligned} \tag{4.16}$$

For a n-*qubit* system

$$T_{i_1,i_2,...,i_n} = (P_{|\psi_{i_1}\rangle} \pm P_{|\psi_{i_1}^{\perp}\rangle}) \otimes (P_{|\psi_{i_2}\rangle} \pm P_{|\psi_{i_2}^{\perp}\rangle}) \otimes ... \otimes (P_{|\psi_{i_n}\rangle} \pm P_{|\psi_{i_n}^{\perp}\rangle}) \tag{4.17}$$

where the $+$ is used for a zero index and the $-$ for a non-zero index.

T_{i_1,i_2} simplifies for a two-*qubit* system to

$$\begin{aligned} T_{i_1,i_2} &= (P_{|\psi_{i_1}\rangle} - P_{|\psi_{i_1}^{\perp}\rangle}) \otimes (P_{|\psi_{i_2}\rangle} - P_{|\psi_{i_2}^{\perp}\rangle}) \\ &= P_{|\psi_{i_1}\rangle|\psi_{i_2}\rangle} - P_{|\psi_{i_1}\rangle|\psi_{i_2}^{\perp}\rangle} - P_{|\psi_{i_1}^{\perp}\rangle|\psi_{i_2}\rangle} + P_{|\psi_{i_1}^{\perp}\rangle|\psi_{i_2}^{\perp}\rangle} \end{aligned} \tag{4.18}$$

in the case $i_1 \neq 0$ and $i_2 \neq 0$, and for $i_1 = 0$ or $i_1 = 0$ follows:

$$\begin{aligned} T_{i_1,i_2} &= (P_{|\psi_{i_1}\rangle} + P_{|\psi_{i_1}^{\perp}\rangle}) \otimes (P_{|\psi_{i_2}\rangle} + P_{|\psi_{i_2}^{\perp}\rangle}) \\ &= P_{|\psi_{i_1}\rangle|\psi_{i_2}\rangle} + P_{|\psi_{i_1}\rangle|\psi_{i_2}^{\perp}\rangle} + P_{|\psi_{i_1}^{\perp}\rangle|\psi_{i_2}\rangle} + P_{|\psi_{i_1}^{\perp}\rangle|\psi_{i_2}^{\perp}\rangle} \end{aligned} \tag{4.19}$$

with

$$P_{|\psi_{i_1}\rangle|\psi_{i_2}\rangle} = \frac{I(|\psi_{i_1}\rangle\,|\psi_{i_2}\rangle)}{I(|\psi_{i_1}\rangle\,|\psi_{i_2}\rangle) + I(|\psi_{i_1}\rangle\,|\psi_{i_2}^{\perp}\rangle) + I(|\psi_{i_1}^{\perp}\rangle\,|\psi_{i_2}\rangle) + I(|\psi_{i_1}^{\perp}\rangle\,|\psi_{i_2}^{\perp}\rangle)} \tag{4.20}$$

where $I(|\psi_{i_1}\rangle\,|\psi_{i_2}\rangle)$ are measured coincidences between the bases $|\psi_{i_1}\rangle, |\psi_{i_2}\rangle$, assuming the same measurement time for each coincidence measurement. The same follows for the other measurement bases.

If we now again assume the same orthogonal basis describing the Stokes parameters, as before

$|\psi_1\rangle \equiv |D\rangle$, $|\psi_2\rangle \equiv |R\rangle$ and $|\psi_3\rangle \equiv |H\rangle$, we end up with the following single two-*qubit* Stokes-like parameters T: Note, we assume again $\tau = \sigma$, hence in our special case $T = S$.

$$\begin{aligned}
S_{1,1} &= P_{DD} - P_{DA} - P_{AD} + P_{AA} \\
S_{1,2} &= P_{DR} - P_{DL} - P_{AR} + P_{AL} \\
S_{1,3} &= P_{DH} - P_{DV} - P_{AH} + P_{AV} \\
S_{2,1} &= P_{RD} - P_{RA} - P_{LD} + P_{LA} \\
S_{2,2} &= P_{RR} - P_{RL} - P_{LR} + P_{LL} \\
S_{2,3} &= P_{RH} - P_{RV} - P_{LH} + P_{LV} \\
S_{3,1} &= P_{HD} - P_{HA} - P_{VD} + P_{VA} \\
S_{3,2} &= P_{HR} - P_{HL} - P_{VR} + P_{VL} \\
S_{3,3} &= P_{HH} - P_{HV} - P_{VH} + P_{VV}
\end{aligned} \tag{4.21}$$

These nine two-*qubit* Stokes Parameters can be measured using nine complete four-element basis measurement, giving us a total of 36 measurement results. To measure, for example, $S_{1,1}$, *qubit* 1 and *qubit* 2, are split and each analyzed in the D, A polarization basis using a half wave plate and a polarizing beam splitter. Then the correlations between the different *qubit* outputs are collected simultaneously. Using Eq. 4.20 we normalize the collected coincidences and hence can calculate the different probabilities for $S_{1,1}$.

The six remaining required Stokes parameters to fully describe the state, depend upon the same measurements already conducted in the previous nine measurements and can be extracted from them with the following conditions:

$$\begin{aligned}
S_{0,1} &= P_{DD} - P_{DA} + P_{AD} - P_{AA} \\
S_{0,2} &= P_{RR} - P_{LR} + P_{RL} - P_{LL} \\
S_{0,3} &= P_{HH} - P_{HV} + P_{VH} - P_{VV} \\
S_{1,0} &= P_{DD} + P_{DA} - P_{AD} - P_{AA} \\
S_{2,0} &= P_{RR} + P_{LR} - P_{RL} - P_{LL} \\
S_{3,0} &= P_{HH} + P_{HV} - P_{VH} - P_{VV}
\end{aligned} \tag{4.22}$$

These, in total, 15 Stokes parameters exactly describe the point in the 2^2 Hilbert space, fulfilling the condition of $4^n - 1$ parameters. Hence, this point is exactly determined by the set of nine 4-bases measurement set of Eq. (4.21). We collect these 36 measurements by averaging over the detection events of multiple *qubits* for the same basis, as given by the nine sets in Eq. (4.21). We can now use Eq. (4.15) to reconstruct the density matrix of the state.
Note, this formalism is not only valid for two-*qubit* systems, but can be extended to n-*qubits* systems.

Measuring a ϕ^+ entangled state

Let's assume we would like to measure the density matrix of the $|\phi^+\rangle = \frac{1}{\sqrt{2}}(|HH\rangle + |VV\rangle)$ Bell state. In order to extract the density matrix, we need to measure the 36 coincidence probabilities given in Eq. (4.21), with Eq. (4.11), for the different polarization bases $|D\rangle$, $|R\rangle$, $|H\rangle$. After collecting the coincidences for the different bases, and normalizing them to the total amount of coincidences for a certain basis set, we can reconstruct the density matrix using Eq. (4.15). This, in a perfect scenario, leads to the following matrix:

$$\rho_{\phi^+} = \frac{1}{2}\begin{pmatrix} 1 & 0 & 0 & 1 \\ 0 & 0 & 0 & 0 \\ 0 & 0 & 0 & 0 \\ 1 & 0 & 0 & 1 \end{pmatrix} \tag{4.23}$$

The finite acquisition time and the statistical distribution of the finite acquisition can render the matrix non-physical, meaning the matrix might have non-physical states (no positive real eigenvalues). Additionally, non-perfect entangled states or measurement artifacts, such as accidental coincidences, beam splitter crosstalk, intensity drifts, introduce errors into the matrix, introducing a mixture or imaginary components. For this reason, a Maximum Likelihood algorithm with a least square minimization of the measured matrix with a physical matrix is applied and returns a physical matrix which is the most likely to have been produced by the measurement [143].

4.4.1 Measures of entanglement and mixture

The previous section explained how the quantum state can be measured using quantum state tomography. Since the quality of the entangled photon source is an important factor because it is pivotal for the success of many applications in this thesis. Hence, the reconstructed quantum state is then characterized by the crucial measures for our implementations, which include fidelity and concurrence.

Fidelity Fidelity is the measure of the state overlap of the reconstructed quantum state ρ_1 with a reference state ρ_2, which we would like to compare it to.

$$F(\rho_1, \rho_2) = (Tr\{\sqrt{\sqrt{\rho_1}\rho_2\sqrt{\rho_1}}\})^2 \tag{4.24}$$

The formula simplifies to $Tr\{\rho_1, \rho_2\}$, considering one state is pure, and simplifies further to $|\langle\psi_1|\psi_2\rangle|^2$, for two pure states.
In our case, the *QD* emits a ϕ^+ state when analyzing the X and XX at π-pulse area. Consequently, we analyse the overlap of the measured state ρ_1 with the perfectly entangled Bell state $|\phi^+\rangle = 1/\sqrt{2}(|HH\rangle + |VV\rangle)$. If the fidelity to a Bell state is higher than 50 % a presence of entanglement can be considered [143].

Concurrence and tangle The fidelity, though, is not always a reliable measurement of entanglement because it changes with unitary transformations. A quantitative measure of entanglement

is the amount of separability of the state, which is the information loss when tracing out part of the system [144]. One measure for separability is the concurrence.
For two *qubits*, concurrence is defined as follows: consider a non-Hermitian matrix $R = \rho\Sigma\rho^T\Sigma$ where T denotes the transpose and Σ the spin flip matrix defined by

$$\Sigma \equiv \begin{bmatrix} 0 & 0 & 0 & -1 \\ 0 & 0 & 1 & 0 \\ 0 & 1 & 0 & 0 \\ -1 & 0 & 0 & 0 \end{bmatrix} \tag{4.25}$$

We calculate the eigenvalues of R and sort them in decreasing order by $r_1 \geq r_2 \geq r_3 \geq r_4$. Then the concurrence is calculated:

$$C = Max\{0, \sqrt{r_1} - \sqrt{r_2} - \sqrt{r_3} - \sqrt{r_4}\} \tag{4.26}$$

The tangle is directly extracted from the concurrence by

$$T \equiv C^2 \tag{4.27}$$

The concurrence (and the tangle) range from 0 for product states (any incoherent mixture of product states) to a maximum value of 1 for Bell-states. The higher the concurrence (tangle) the higher the non-classical correlation of the two *qubit* systems.

4.4.2 Entanglement measurement setup

To measure the 36 coincidence probabilities given in Eq. (4.21), the X and XX photons are spectrally selected and each sent to a state-tomography setup, see Figure 4.5. The state-tomography setup consists of a set of quarter waveplate, half waveplate (both mounted on motorized rotational states (Newport, Thorlabs)) for state rotation and a polarizing beam splitter for state selection. Using this technique, the X and XX photons can be projected on the different bases. A MATLAB program is coded to move the rotational waveplates to the different bases that have to be analyzed and instructs the time-to-digital converter to collect the four possible coincidence measurements for each waveplate setting for a specified acquisition time. After the acquisition of the first basis is finished, the program moves the rotors to the next basis setting from Eq. (4.21) and again the coincidences are collected using the functionalities of the TimeTagger Ultra (Swabian Instruments). An image of the GUI of the custom MATLAB program is shown in Figure 4.6. The program allows to select different rotors as well as choosing between the full quantum state tomography (36 coincidence measurement setting), or a reduced quantum state tomography (16 coincidence measurement setting, which is not used in this thesis). When the automatic acquisition is complete, the collected coincidence measurements for each channel combination are normalized by the total amount of coincidence for that particular measurement setting. This is the input for the state-tomography analysis software, which first directly constructs the density matrix, as described before, and additionally runs a maximum likelihood estimation.

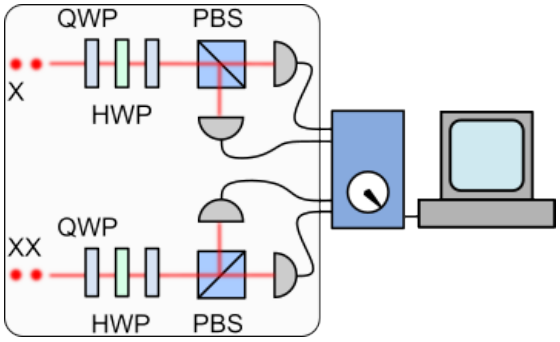

Figure 4.5. Quantum state tomography setup. The spectrally selected X and XX signal is rotated on a set polarization state using the half-waveplate (HWP) and quarter-waveplate (QWP) and projected by the polarizing beam splitter (PBS).

Figure 4.6. Custom-written quantum state tomography measurement software. The custom-written MATLAB program allows the user to input a file with the different measurement bases. After inserting the different rotors, measurement protocol, acquisition times, and other measurement settings, the measurement for the different entered bases is performed automatically. In case needed, the software immediately analyzes the resulting experimental estimate of the quantum state.

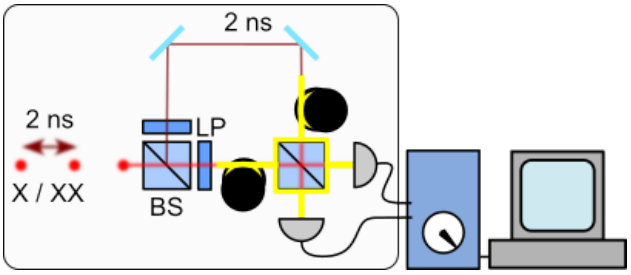

Figure 4.7. Two-photon interference setup. The analyzing setup consists of a beam splitter (BS) to couple half the photons in the delay line. This mirrors the delay in excitation, which created a train of photon pairs separated by a 1.8 ns delay. The photons for each output of the first BS are first polarization selected with a linear polarizer (LP) and then coupled into a fiber-BS. Fiber-induced polarization changes and letting interfere photons with different polarization is performed by adjusting the polarization with bat-ear polarization controllers for fibers, installed on both the input fibers. The two *APDs* at the output ports of the interfering BS detect the signal, which is converted to a coincidence histogram in a time-to-digital converter.

4.5 Hong-Ou-Mandel interferometry

The *HOM* effect is an important measure for the indistinguishability of photons. It can be estimated from the *HOM* visibility, despite the fact that even for perfectly indistinguishable photons the *HOM* visibility can be lowered due to measurement artifacts, as imperfect beam splitters or dark counts [145].

The interference of two photons is conducted by exciting a *QD* with a pulsed Ti:Sapphire laser, at a repetition rate of 80 MHz. The excitation path is modified to obtain a train of pairs of pulses separated by a 1.8 ns delay. The same delay is mirrored after spectrally splitting the train of emitted photons and selecting a single emission line in the detection path, to overlap two consecutively excited photons from the QD on a 50:50 fiber-beam splitter, see Figure 4.7. Before coupling into the fiber input ports of the beam splitter, linear polarizers are placed for polarization selection. To compensate for fiber-induced polarization changes and to let interfere photons with different polarization, bat-ear polarization controllers for fibers are installed on both the input fibers. This allows us to have full control over the polarization of the interfering photons and makes it possible to interfere only photons with a specific polarization state.

When two subsequent laser pulses excite the *QD*, two photons are emitted, which can interfere at the last beam splitter, depending on the path taken. Figure 4.8 shows five peaks, which correspond to the different delay times from the possible combinations of photon paths, see Figure 4.7. The central peak at zero-time delay results from the paths, when the first emitted photon takes the long arm of the Mach-Zehnder interferometer, while the second photon takes the short path. Here, the two photons arrive at the beam splitter at the same time. If the photons are distinguishable no interference takes place and the central peak has the same intensity of the side peaks at immediately later time delays. This can be enforced experimentally by measuring the *HOM* visibility in cross-polarization configuration. This means, selecting the polarization of one input arm in the interfering beam splitter to H polarization and the second input arm to V polar-

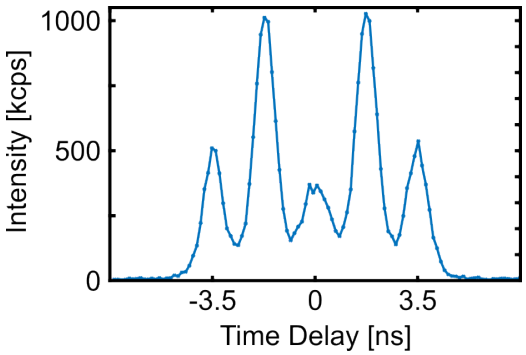

Figure 4.8. Two-photon interference coincidence histogram from co-polarized photons emitted by the same GaAs *QD* with a time delay of 1.8 ns, under resonant *TPE*. The central peak is expected to have the same area of the immediate side ones for total distinguishable photons and to be null for perfectly indistinguishable photons. The extracted interference visibility is 64(3) %.

ization using the bat-ear polarization controllers. Instead, if we set both input paths to the same polarization (co-polarization setting) and the two photons are indistinguishable in all their degrees of freedom, interference occurs and a dip in the coincidence count is observed. This dip happens because the two photons leave the beam splitter at the same exit port, see Eq. (2.18). However, in real experiments, the dip is not zero, which is due to the various physical mechanisms described in Section 3.5.4.

The *HOM* visibility in co-polarization measurements, as shown in Figure 4.8, can be estimated using the following formula:

$$V = 1 - \frac{I(0)}{I(\tau)} \tag{4.28}$$

Using this approximation, for the example of co-polarized exciton photons coming from subsequent biexciton-exciton radiative cascades from the same GaAs *QD* under resonant excitation a raw *HOM* visibility of about 0.65 was measured.

A more accurate way of estimating the *HOM* visibility is by performing co- and cross-polarization measurements. There the *HOM* visibility can be directly extracted from the amount of coincidences at zero-time delay for the two different measurement settings of co- and cross-polarization:

$$V = 1 - \frac{I_{co}}{I_{cross}} \tag{4.29}$$

I_{co} corresponds to the coincidences at zero-time delay for the co-polarized measurement setting, hence indistinguishable case. I_{cross} on the other hand, corresponds to the intensity at zero-time delay for the cross-polarization measurement setting, consequently, fully distinguishable photons.

Chapter 5

Limitations on entanglement of GaAs/AlGaAs quantum dots

Highly entangled photon sources are the core elements for the success of quantum key distribution [23] and the build of photonic quantum networks [146]. GaAs *QDs* are currently one of the most promising sources to generate entangled photons with a low multiphoton emission probability [27, 28], high degree of entanglement [80], photon-indistinguishability [29, 30], wavelength-tunability [31], as well as with nearly on-demand generation [25]. These points are underlined with the experimental demonstration of single-photon emission with a $g^{(2)}(0)$ as low as $7.5 \pm 1.6 \cdot 10^{-5}$ [28] and, more importantly, entanglement figures of merit of 0.97(1) and 0.978(5) for concurrence and entanglement fidelity, respectively [37]. This degree of entanglement, however, is exceptional and only achieved in precisely pre-selected *QDs*. Standard samples, fabricated by *LDE*, typically exhibit entanglement values above 90 % [23, 95, 147], which is significantly lower than the almost perfect entanglement of the state-of-the-art sources based on *SPDC* [20]. This considerably lower entanglement reduces the advantage of *QDs* as deterministic entangled photon sources compared to the probabilistic *SPDC* sources. In *QKD*, for example, a lower entanglement leads to a higher error rate limiting the transmission distance [148]. Also, for the realization of quantum networks, having a sub-optimal entanglement is strongly detrimental. As briefly mentioned in the introduction, the core element of a quantum network is a quantum repeater, to exceed certain communication lengths as well as to synchronize the communication between multiple parties. These quantum repeaters rely on entanglement swapping to link the nodes, and quantum teleportation to transfer the state. For both experiments, high entanglement is crucial to reach high efficiencies in the swapping/teleportation process [149].

Spatial [34] or temporal filtering [150] allows to experimentally only select good entanglement values, increasing the entanglement figures of merit of *QDs* making them comparable to *SPDC*. But filtering comes at the cost of brightness and weaker signal limiting the transmission rate. In addition, filtering the emitted photons suspends the potential of on-demand entangled photon generation, which is an important factor for longer transmission lengths in *QKD*. For these reasons, it is important to investigate where the degradation of entanglement comes from in *QDs* and to eliminate the problem at its core.

The potential factors reducing entanglement in photon pairs generated from *QDs* are manifold. The main degradation cause in *QD* systems is the *FSS*. As addressed in Section 3.5.1, a broken symmetry of the excitonic wavefunction lifts the energy degeneracy of the two possible decay paths in the radiative *QD* cascade, inducing a temporal phase to the entangled state. This phase is indeterminate before measurement and gets fixed upon measurement according to the emission time of the photons. When measuring the time-averaged fidelity to a maximally entangled Bell state, one averages over multiple entangled states with different phases [100, 103]. Consequently, the measured time-averaged two-photon state is mixed, leading to a reduced degree of entanglement. The same effect of time-averaging would apply for the *BSM*, reducing the photon indistinguishability. One can quantify this effect on the entanglement by including the *FSS* into the density matrix of the entangled photon state emitted by a GaAs/AlGaAs. This leads to the following quantum state representation [151]:

$$\rho = \frac{1}{2}\begin{pmatrix} 1 & 0 & 0 & exp(\frac{-iSt}{\hbar}) \\ 0 & 0 & 0 & 0 \\ 0 & 0 & 0 & 0 \\ exp(\frac{iSt}{\hbar}) & 0 & 0 & 1 \end{pmatrix} \tag{5.1}$$

with S the energetic separtion equal to the *FSS* and t, the time spent in the superposition state of the two exciton states. With a demonstrated average *FSS* value of droplet-etched *QDs* of $2.5 \pm 1.3\,\mu eV$ [36], the concurrence (fidelity) is lowered to 0.7245 (0.8624) from the initial 100 %. However, external perturbations, such as electric [107], magnetic [100] and strain fields [108] provide the possibility to compensate for the *FSS* directly, by modifying the *QD* electronic structure. Using the latter technique, entanglement could be restored and pushed to the record-high values for GaAs/AlGaAs *QDs* [37].

The second, often investigated entanglement degradation effect is the interaction of the *QD* exciton with its nuclear environment via the hyperfine interaction. The large nuclear spin ensemble present in the solid-state structure acts on the electron spin and induces an effective fluctuating magnetic field, the Overhauser field [152]. This effect is stronger for *QD* materials with species with high nuclear spin number, as In in InAs, which has a nuclear spin of 9/2. For GaAs, where the Ga nuclei have a nuclear spin of 3/2, the Overhauser field amounts to a maximum field of $B_{max} = 4$T with a standard deviation of $\sigma = B_{max}/\sqrt{N} = 4$ mT, with N being the number of nuclei [152]. At 4 K, the operation temperature for the experiments, the nuclei are not polarized and hence only the fluctuation around the null mean value σ enters. We can use this information and the measured magnetic response ($\gamma_z = 16.81\,[\frac{\mu eV}{T^2}]$, $g_z = 1.112$ and $g_{2,z} = -0.001\,[T^{-2}]$) to determine the energy splitting of the X energy looking at the induced Zeeman splitting of this static field [153]. The energy splitting amounts to roughly 0.3 μeV, which is one order of magnitude lower than the average *FSS* and the Fourier-transform limited linewidth, which is roughly 2.3 μeV for the X of as-grown GaAs *QDs* [36]. To quantify the effect of the nuclei induced energy splitting of 0.3 μeV on the entanglement, we use the same model from before. If we assumed that these would

be the only effect reducing the entanglement of the biexciton-exciton photon pair, the resulting fidelity and concurrence would be 0.9975 and 0.9949, respectively. These numbers visualize that the effect of the nuclei on entanglement is rather small for GaAs *QDs*, especially when comparing it to other entanglement degrading effects, as the *FSS*. Consequently, I do not investigate it further in the course of this thesis.

The third limiting factor for unity entanglement in GaAs/AlGaAs *QDs* are decoherence effects. In depth studies demonstrate that there are many different mechanisms that fall under the category of decoherence effects, which all in general influence the entangled state. We can include them in the density matrix from before by extending it with the different factors, which results in a mixed output state [100]. The different factors are background light, spin-scattering and cross-dephasing of the exciton state. Background light is light that originates from any area of the sample or the *QD*, except the *X* and *XX* emission from the *QD*. Its polarization is random and hence contribute to uncorrelated light in polarization, which lowers entanglement. This effect can be minimized by carefully filtering out any light except the *X* and *XX* photons of the *QD*. Spin-scattering, the second factor, flips the spin of the exciton after the emission of the biexciton photon. One hypothetical scenario, where two photons are emitted via the radiative cascade but their polarization is random due to a spin flip could be the following: The *QD* emits one photon, the *XX* photon, the remaining bright exciton experiences a spin flip to the dark exciton state and a flip back to the bright exciton one, which afterwards recombines and emits the *X* photon. In this scenario still both photons would be emitted from the cascade, however, the photons would not be entangled in polarization. The lack of polarization correlation between the biexciton photon and the exciton photon lowers the entanglement. The last factor is the dephasing of the bright exciton states. One has to distinguish between two different types of dephasing, pure dephasing of a state and cross-dephasing between two states. Prior randomizes the phase of the single eigenstate with itself, meaning it resets the phase of the eigenstate after some time. Even if this phase is randomized, it may not affect entanglement, if the same phase jump is observed between the two exciton transitions. Hence, the phase relationship between the two states is kept, which is exactly important for entanglement. The second, cross-dephasing, on the other hand, randomizes the phase between the two bright exciton states. This phase change between the two bright exciton states results that the exciton and biexciton are still correlated, but the phase of the superposition changes, which lowers the entanglement. Using this information on the different decoherence mechanisms we can write the full density operator [100]:

$$\rho = \frac{1}{4}\begin{pmatrix} 1+kg'^{(1)}_{H,V} & 0 & 0 & 2kg^{(1)}_{H,V}z^* \\ 0 & 1-kg'^{(1)}_{H,V} & 0 & 0 \\ 0 & 0 & 1+kg'^{(1)}_{H,V} & 0 \\ 2kg^{(1)}_{H,V}z & 0 & 0 & 1+kg'^{(1)}_{H,V} \end{pmatrix} \tag{5.2}$$

with

$$g'^{(1)}_{H,V} = 1/(1+\tau_1/\tau_{SS})$$
$$g^{(1)}_{H,V} = 1/(1+\tau_1/\tau_{SS}+\tau_1/\tau_{HV})$$
$$z = \frac{1+ix}{1+x^2},\ x = \frac{g^{(1)}_{H,V} S\tau_1}{\hbar}$$

k is the fraction of photons that both come from the same radiative XX-X cascade with respect to the total number of detected pairs, τ_1 the radiative recombination time of the exciton state, τ_{SS} and τ_{HV} are the average times of the spin-flip and cross-dephasing, and S is the fine structure splitting.
From this representation we can see that the effect of fluctuating electric fields are less detrimental for entanglement, because only fast processes (within 250 ps) matter for entanglement rendering the slower electron fluctuations in the ns range negligible [140]. Also phonon induced effects are marginal because they would not affect cross-dephasing. Furthermore, from this representation we immediately see the important parameters for the effect on entanglement, which are the exciton lifetime and the various dephasing times. If we shorten the lifetime of the exciton state τ_1 we can extract that the mixed state ρ is less exposed to the different dephasing mechanisms, because the dephasing factors $g'^{(1)}_{H,V}$ and $g^{(1)}_{H,V}$ go towards 1. This leads to the idea of using photonic cavities to shorten the lifetime of the transition. In GaAs *QDs* a lifetime shorter by a factor 3 (Purcell factor of 3) for the high entanglement value of 0.978(5) [37] is expected to mitigate the dephasing resulting in a fidelity of 0.99 [154]. One photonic cavity suitable for the broadband emission of GaAs *QDs* and shows modest Purcell effect are second-order Bragg gratings [119]. Despite their potential to reach Purcell factors of 3, the highest up to now measured fidelity in this cavity is 0.90(1) [30].

The fourth entanglement degrading effect is due to recapture processes during excitation, where the excited state is repopulated immediately after emission of a photon. Recapture processes disrupt an ordered stream of polarization entangled photon pairs throughout undesired excitation cycles and trigger the detection of uncorrelated photon-pairs. For coherently driven two-level systems re-excitation processes in *QDs* can lead to non-negligible values of the second-order auto-correlation function (typical a few percentage points). The effect is in particular apparent when values of excitation power beyond the optimal brightness condition are employed [155]. It has been demonstrated that multiphoton pair emission is much less pronounced for photons from the *XX-X* cascade, provided that the laser pulse length is sufficiently small [27, 28]. Nonetheless, these experimental studies do not investigate the degree of entanglement of the emitted photon pairs. Therefore, we want to answer the question if *QDs* can be considered multipair-free sources of polarization-entangled photons. Hence, we investigate the multipair emission rate from the intensity auto-correlation function in a typical excitation condition of *TPE*, which is preferably applied for entangled photon generation. Additionally, we estimate the effect of multipair emission on the density matrix, which we then proof experimentally. This study is discussed in the first part of this chapter.

The last entanglement degrading effect in *QDs*, which has been recently highlighted by comprehensive theoretical simulations, is related to the particular excitation method used for entangled photon generation, *TPE*. As previously discussed, *TPE* has the potential to almost deterministically generate entangled photons with high entanglement fidelity, with values above 0.90 in GaAs *QDs* [95]. However, theoretical predictions unveiled that the excitation laser-induced local electric field, which shifts the energies due to the AC Stark effect, is also present for normal driving conditions in *TPE* [156]. This effect has been experimentally shown for resonant fields [157, 158] and points out that this energy level shift is only induced during the presence of the excitation laser. Hence, the important factor for this degrading effect is the fraction between the biexciton and excitation laser lifetime. This excitation laser-induced effect is in particular important when considering the claims that cavities would enhance the entanglement fidelity up to 0.99 [154]. These state that the cavities shorten the lifetimes and consequently shorten the interaction times with the environment, which may increase the entanglement through less dephasing, as previously discussed. However, shortening the lifetime would increase the fraction of emitted photons, which experience the presence of the excitation laser, which according to the theoretical predictions would lower entanglement as well [156]. Currently it is not clear if this laser-induced AC Stark effect is also identifiable experimentally. In a brief section in this chapter, I demonstrate the first preliminary data supporting this theoretical work. The obtained results raise the question, if the already demonstrated entanglement fidelity of 0.978(5) [37] might have already been performed on a *QD* with no relevant dephasing mechanism apart from the one induced by the excitation mechanism.

5.1 Entanglement degradation due to multipair emission

Multiphoton emission, as discussed in the introduction, reduces the achievable secure key rate in quantum key distribution [22, 23] and hampers the scalability of multiple photon experiments [20]. Deterministic entangled-photon sources eliminate this restraining factor. One promising potentially deterministic platform, introduced earlier, are solid-state-based quantum emitters, notably epitaxial *QDs*. *QDs* have the potential to overcome this hurdle because they promise near-deterministic generation of strongly entangled photons [114, 149]. In principle, *QDs* exhibit no compromise between multiphoton emission and brightness [145, 159]. However, recent studies on coherently driven *QDs* have highlighted that re-excitation processes can lead to non-negligible values of the second-order auto-correlation function $g^{(2)}(0)$ (as measured via a Hanbury Brown and Twiss (HBT) interferometer) [148, 160], which is so far always put on the same level with the multiphoton emission probability for *QDs*. Thus, these finite (non-negligible) values of $g^{(2)}(0)$ would negatively impact the level of entanglement of the emitted photons, which has been demonstrated experimentally [161]. But these experiments do not employ resonant excitation schemes, and additionally, it is often experimentally challenging to ascertain whether the entanglement degradation and the finite $g^{(2)}(0)$ values are due to true multiphoton emission or background light originating from the excitation laser and/or states not involved in the entangled photon generation process. Also the literature does not clarify this ambiguity. It exhibits inconsistencies on how to relate the information

on multiphoton emission given from the $g^{(2)}(0)$ to the polarization density matrix [37, 151, 162]. For this reason, it remains unclear whether *QDs* can be regarded as a multipair-free source of entangled photons. I address this question by carefully studying the interplay between the second-order coherence function, the multiphoton emission probability, and the degree of entanglement in resonantly driven *QDs*.

5.1.1 Experimental implementation

The investigated entangled photon emitter is a GaAs/AlGaAs *QD* grown by droplet-etching epitaxy [83]. These nanostructures provide state-of-the-art fidelity to a maximally entangled state without resorting to spectral filtering or temporal post-selection [37]. The full composition of the device is explained in Section 3.2 with a solid immersion lens to enhance the extraction efficiency, as discussed in Section 3.5.3. A sketch of the sample structure is shown in Figure 3.7.

The sample is operated at 4 K in a low-vibrational closed-cycle He cryostat from attocube. It is resonantly driven by a Ti:Sprapphire femtosecond laser from Coherent with a repetition rate of 80 MHz and a pulse duration—adapted with a custom-made pulse-slicer—of approximately 10 ps (ca. 200 μeV at 785 nm). The laser is tuned to half the energy difference between the (XX) and the ground state (0) to achieve resonant two-photon excitation [111, 112], as illustrated in the energy scheme in Figure 3.4. The mismatch between the laser energy and the emission energies of the X and the XX state, due to a XX binding energy of ~ 4 meV (~ 2 nm), allows for spectral filtering of the laser back-reflection. This is performed by a set of tunable volume Bragg gratings with a bandwidth of 0.41 nm used in reflection. Emission spectra for two different pump powers and pair generation rates are shown in Figure 5.1. The two peaks with higher intensity correspond to the two transitions of the XX-X cascade, whereas the secondary peak (X^*) is unrelated to the cascade and has a linear dependence on the laser power [28]. X^* is most probably a negatively charged exciton weakly excited through its high-energy acoustic phonon sideband. To maximize the emission rate of the *QD* we maximize the "on"-time of the *QD* [163] with an additional off-resonant light field in a process known as photo-neutralization. The intensity of the off-resonant light is optimized to accelerate charge fluctuations in the *QD* and increase the average probability of having it sitting in the neutral ground state. The coherence of the excitation of a three-level system can be checked by measuring the Rabi oscillations of the *QD* cascaded photon emission, so the X and XX lines [100]. As shown in Figure 5.2, the integrated intensity of the X and XX lines exhibits the typical dependence of (population, depopulation) on the excitation power. The first maximum (π-pulse area) corresponds to the excitation power to optimally populate the biexciton state. This optimal preparation of the state results in a high photon emission rate. For 2π-pulse area, on the other hand, the coherently-driven system is forced back in its ground state lowering the probability of starting the radiative cascade. Consequently, the emitted intensity is weaker, which corresponds to the first minimum in Figure 5.2.
The selected *QD* for the experiment has a *FSS* lower than the spectral resolution of 0.5 μeV, which is the limit of our measurement system. This low *FSS* minimizes the induced relative phase precession in the polarization-entangled state [100]. The X lines is spectrally separated using a *Volume Bragg*

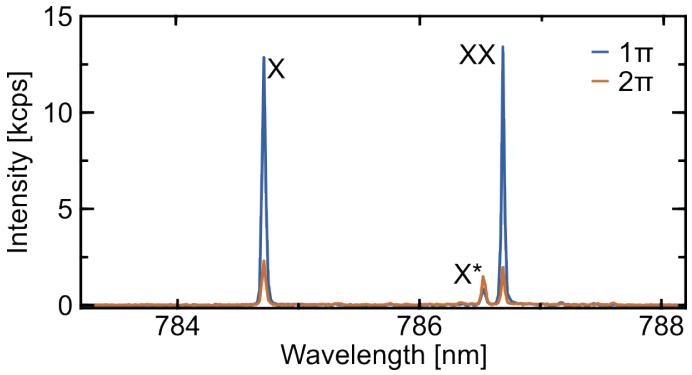

Figure 5.1. Photoluminescence spectrum of the *QD* at π- and 2π-pulse. A line (X^*) unrelated to the cascade is observed. Adapted from Ref. [95]

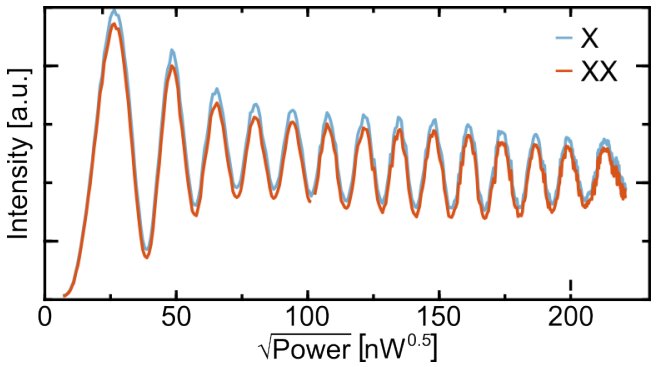

Figure 5.2. Rabi oscillations of X/XX emission intensity vs. laser power. Adapted from Ref. [95]

Grating (VBG) with a filter bandwidth of 0.41. The XX line is sent into the spectrometer, dispersed by the 1200 g/mm grating and spectrally selected by adjusting the grating angle to center the intended wavelength onto the output port of the spectrometer. The filter bandwidth is set to 0.07 nm by closing the output slit accordingly. This approach was chosen to achieve a higher spectral resolution and an option for bandwidth fine-tuning. As discussed in the following section, the XX filter bandwidth is chosen narrower to remove undesired emission wavelengths, as the undesired X* peak. Yet, both bandwidths are large enough not to filter out any significant fraction of the X and XX photoluminescence signal. The X and XX photons are then analyzed by a polarization-resolved cross-correlation measurement setup, similar to the one presented in Section 4.4 for quantum state tomography, see Figure 5.3. This consists of two sets of a half-waveplate and a quarter-waveplate (for state rotation), a polarizing beam splitter, for state projection), and two *APDs*. The second-order auto-correlation $g^{(2)}(\tau)$ measurements were performed with the same setup, by replacing each polarizing beam splitter with a 50:50 beam splitter, as in a standard *HBT* interferometer.

5.1.2 GaAs/AlGaAs quantum dot - A true single photon source

Firstly, we are interested in the single-photon nature of the investigated GaAs *QD*, especially when varying the pump power. To do so, we study the second-order auto-correlation function of the *QD* under quasi-deterministic resonant *TPE*, the most common excitation technique for entanglement-based applications. Additionally, we renounce the use of polarization suppression, a

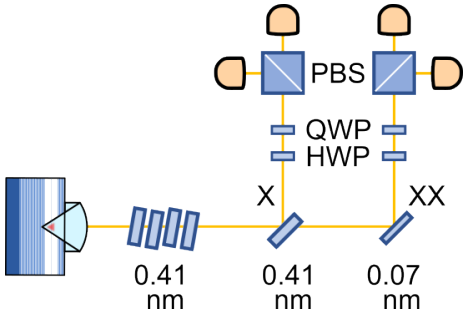

Figure 5.3. Quantum state tomography setup. The laser is filtered by volume Bragg gratings. The X and XX are spectrally filtered with bandwidths of 0.41 and 0.07 nm, respectively. The state is rotated via a half-waveplate (HWP) and quanter-waveplate (QWP), and selected with a polarizing beam splitter (PBS). For the second-order auto-correlation measurements, the PBSs are exchanged with 50:50 beam splitters. Adapted from Ref. [95]

frequently used technique to measure the second-order auto-correlation function, but incompatible with polarization-resolved coincidence measurements, which are needed in the next step to determine the entanglement in polarization of the *QD* photons. In this measurement condition, the next section discusses how to eliminate errors introduced by the measurement equipment and excitation conditions, as well as how mild spectral filtering affects the measurements.

Filtering background events from entanglement-based measurements

Since we are interested in the multipair emission of the GaAs/AlGaAs *QD* under the same measurement conditions as for entanglement, we measure the second-order auto-correlation function of the emitted light using a *HBT* setup (see Figure 4.4) without resorting to polarization suppression. The auto-correlated signal of the XX for different correlation times is shown in Figure 5.4. Note, this auto-correlation measurement is only an example to visualize the result of the experiment, but this measurement represents the optimized case. At zero-time delay, a low number of coincidences is recorded compared to coincidences from photons of subsequent or later excitations of the radiative cascade due to different laser pulses. The $g^{(2)}(0)$ can be calculated by $g^{(2)}(0) = \frac{I(t_0)}{(I(t_{-1})+I(t_{+1}))/2}$, with $I(t_{-1})$ and $I(t_{+1})$ coincidences corresponding to the time delays of ± 12.5 ns. The $g^{(2)}(0)$ results to $1.7 \pm 0.1 \times 10^{-2}$ for the XX, in a standard experimental configuration, eliminating the laser light with *VBGs*. Since record-low values of $7.5 \pm 1.6 \times 10^{-5}$ have been demonstrated with this source, but using polarization suppression of the excitation laser and superconducting single-photon detectors with ultra-low dark-count rates [28], it raises the question: What is limiting our $g^{(2)}(0)$ measurements and how can we improve it with the given setup? In fact, it is valuable to discern which part of the measured multiphoton component is due to the source and which is due to other factors.

One important precaution is removing backscattered laser light from the excitation laser. Since the excitation laser wavelength for *TPE* lies exactly between the X and XX wavelength, it can easily be filtered out by *VBGs*, as explained in the previous section. Additionally, we add two *VBGs* at the wavelength of the X and XX emission in the excitation path. These are placed to remove laser

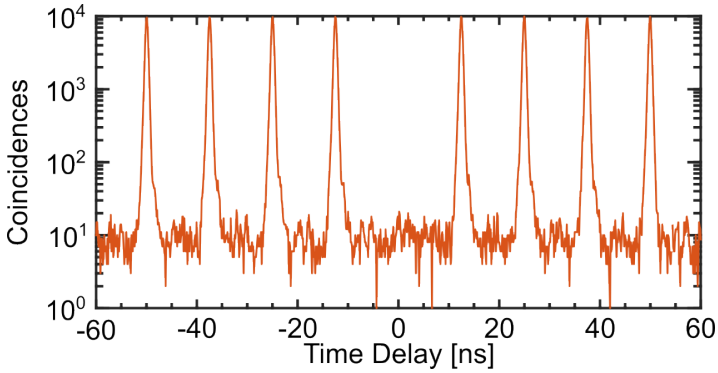

Figure 5.4. Second-order auto-correlation measurement of the *XX* photons. At zero-time delay, a low number of coincidences is recorded compared to coincidences from photons due to different excitation laser pulses.

contributions at the same wavelength of the *QD* signal, which are due to artifacts introduced by the custom-made pulse shaper. The excitation spectrum exhibits interference maxima at exactly the *X* and *XX* wavelengths, which contribute as uncorrelated background to any collected signal. These features are attributed to the first ring of the Airy disks formed on the focal plane of the 4f pulse-shaper, where the slit for wavelength selection is placed. After adequately filtering the laser in the collection and excitation paths, we verified that no signal is present by using the same collection setup and moving the stage under the objective away from the *QD* position in the sample. Finally, we remove another detrimental effect, which is present due to after-pulsing artifacts from the *APDs* [164]. In this work we use single photon counting modules from Excelitas, which feature a dead time of 22 ns. Since the after-pulsing effect is mainly observed after the quenching and recharge phase of the *APD*, with a delay from a detection event which is close to double the repetition rate of the pump, this effect causes accidental coincidence events. Here, we apply in post-processing a virtual dead time of 56 ns to the detection events recorded by the time-to-digital converter, to compensate for the effect. However, we have experimentally determined that also a deadtime of 34 ns leads to the same result. These simple amendments to the optical setup and acquisition settings improve the $g^{(2)}(0)$ to $2.4\pm0.1\times10^{-3}$ for the *XX*. This $g^{(2)}(0)$ value corresponds to the measurement shown in Figure 5.4.

To confirm that we only measure the intrinsic $g^{(2)}(0)$ of the *XX*-*X* radiative cascade and do not have any other additional emission from the sample leading to an overestimation of multiphoton contribution, we further investigate the spectral selection of the emission lines. In particular, we focus on the *XX* line and its second-order auto-correlation function and spectrally separate it using a spectrometer, instead of relying on the 0.4 nm fixed bandwidth of the VBG. In this way, we vary the bandwidth acceptance from 0.12 nm to 0.01 nm. Even if the natural linewidth of the *XX*-*X* transition is lower than 0.01 nm, this bandwidth value is lower than the emission linewidth measured on the spectrometer, leading to a transmitted 67 % and 87 % fraction of the *XX* signal for the 0.01 and 0.02 nm settings, respectively. Even though different spectral filters are applied to the *XX* emission line, the $g^{(2)}(0)$ does not change for this range of spectral selection bandwidths at π-pulse area, see Figure 5.5. In this excitation condition, the *QD* is driven resonantly to the *XX*

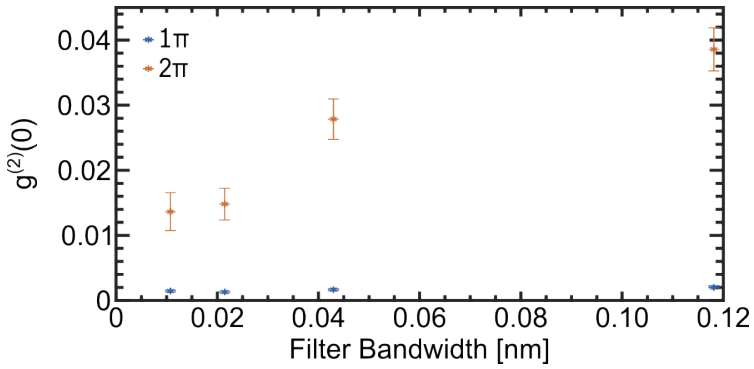

Figure 5.5. $g^{(2)}(0)$ vs. selected spectral bandwidths around the XX emission line for π and 2π excitation pulse area. Note, the error bars for π-pulse area are within the marker size.

state, enabling the highest probability of populating it. We continue this investigation by driving the QD further to 2π-pulse area. Now the laser pulse initially drives the system to the XX state and then depopulates it again to the ground state. Even though the system is driven back to the ground state coherently within the same excitation laser pulse there is still the possibility to have a spontaneous emission event, a probability of inducing the XX-X radiative cascade. Under this excitation condition the emission of the QD signal is much lower than under π-pulse area, but any background emission is higher, arguably increasing linearly with the laser power instead. Also any emission from other states could differ in wavelength from the XX line, which can differently affect the impact of changing the spectral acceptance window.

When now changing the selected spectral bandwidth from 0.12 nm to 0.01 nm at 2π-pulse area, it can be observed that the $g^{(2)}(0)$ of the XX line decreases while narrowing the filtered bandwidth, see Figure 5.5. We interpret this selection as effective in removing the background emission that causes spurious coincidences detected in the HBT setup. It is worth noticing that the $g^{(2)}(0)$ significantly reduces only until the emission linewidth of the QD is reached. Narrowing the filtering from 0.02 nm down to 0.01 nm does not bring any improvement in the zero-time delay intensity auto-correlation function, which implies that we do not observe relevant trade-off between lowering the multiphoton emission and efficiently collecting photons from the radiative cascade. This is very important since having a signal loss through filtering would act as a limitation for applications that need high repetition rates [23] or multiple photon coincidence events [33, 35]. We also point out that the spectral selection is substantially broader compared to the natural linewidth of the emission, so that no effects are expected on the photon emission statistics in this regime [165]. Moreover, filtering the emission spectrum below the natural linewidth also results in the distortion of the wave packet in time. This potentially creates new challenges when dealing with the interference of two photons [127]. Keeping into account all the previously discussed factors, the main residual contribution is light coming from the radiative cascade, which allows to access the intrinsic $g^{(2)}(0)$ of the photon pair generation process. These results support the validity of a quantum tomography measurement setup for assessing the impact of multiphoton emission on the entanglement figures of merit.

Multipair emission contribution in the $\mathbf{g^{(2)}(0)}$

Knowing now that we are measuring the real $g^{(2)}(0)$ in a measurement setting compatible with measuring a density matrix we can now investigate the intended research question, how the multipair contribution acts on entanglement and changes with respect to the driving condition. We start with measuring the $g^{(2)}(\tau)$ for different excitation powers using a *HBT* setup.

$\mathbf{g^{(2)}(0)}$ measurement: Using the *HBT* setup, we measured $g^{(2)}(\tau)$ for different excitation powers. Figure 5.6 shows, in logarithmic scale, the coincidence histograms for the *X* line at π- and 2π-pulse area. The second-order auto-correlation function $g^{(2)}(0)$ is defined as the number of coincidences between photons generated by the same laser pulse (zero-time delay), normalized by that of an equally bright Poisson distributed source. This corresponds to dividing the coincidences at zero-time delay by the coincidences of photons excited by the laser long time delays (till completely uncorrelated, e.g., on the ms timescale) apart. Besides this definition, the second-order auto-correlation function is often interchanged with a different quantity, that we refer to as $\tilde{g}^{(2)}(0)$. It is a relevant quantity for the interference of two photons generated by consecutive pulses and is a common choice in the experimental characterization of quantum emitters for convenience over long-delay normalization. The $\tilde{g}^{(2)}(0)$ is, in contrast to the $g^{(2)}(0)$, calculated by the coincidences of emitted photons at zero-time delay, divided by the coincidences of emitted photons generated by consecutive excitation laser pulses (12.5 ns time delay for 80 MHz repetition rate). This change in normalization leads to a difference in the values of $\tilde{g}^{(2)}(0)$ and $g^{(2)}(0)$, which is accounted for by the blinking of the source. Blinking is an intermittent emission behavior of the *QD* arguably due to the transitory presence of undesired charges in the *QD* and is given as an "on"-time fraction η_{blink}. For the measurements reported here, η_{blink} is estimated to be approximately 0.3. Visible from the formula that links the two normalizations,

$$\tilde{g}^{(2)}(0) = g^{(2)}(0)\eta_{blink} \tag{5.3}$$

$\tilde{g}^{(2)}(0)$ is usually lower than $g^{(2)}(0)$. The measured $\tilde{g}^{(2)}(0)$ is $(3.4 \pm 0.4) \cdot 10^{-3}$ at peak brightness π-pulse for the *X* emission line. When normalizing the coincidences at zero-time delay to the coincidences at consecutive excitation laser pulses (12.5 ns time delay), as done in Figure 5.6, $\tilde{g}^{(2)}_X(0) = \eta_{blink} g^{(2)}_X(0) = (1.0 \pm 0.1) \cdot 10^{-3}$. This is indeed lower by a factor $\eta_{blink} = 0.29$, attributed to the blinking of the source (discussed in the following paragraph). The $g^{(2)}(0)$ value we obtain is very similar to those reported for the GaAs/AlGaAs system [151], only surpassed by the record value obtained using single-photon detectors with ultra-low dark count rates [28]. However, we emphasize that the figures reported here are achieved without polarization suppression of the laser back-reflection or post-selection schemes.

Blinking of the GaAs quantum dot: As stated before, the blinking dynamics is a factor which can affect the dependence of photoluminescence versus excitation power. In fact, blinking is an intermittent emission behavior of the *QD* usually attributed to the transitory presence of undesired charges in the *QD*. If the *QD* initially sits in a charged state, resonant *TPE* of the *XX* cannot

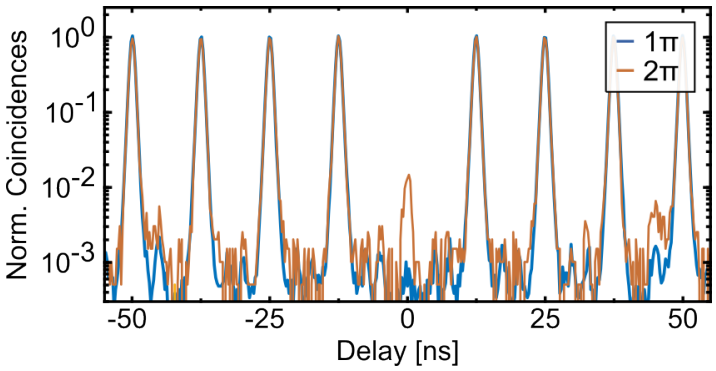

Figure 5.6. Second-order auto-correlation function $\tilde{g}_X^{(2)}(\tau)$, normalized to the side peaks (12.5 ns), at π- and 2π-pulse area. Adapted from Ref. [95]

be performed successfully, and this reduces the pair generation probability. This behavior can be actively suppressed by applying electric fields in a diode structure [139, 147]. When present, it can be affected by the excitation laser, which could in principle ionize traps or photogenerate carriers off-resonantly in the matrix. If these processes depend on power, they must be accounted for when modeling the power dependence of the photoluminescence to deduce the occupation probability of the excited state in the Rabi oscillations. For this reason, we have to investigate how the blinking dynamics changes in the range of excitation power investigated in the main experiment. The study is conducted by measuring the intensity cross-correlation between X and XX photons in an interval of time delays which ranges from 12.5 ns to 0.5 ms. The blinking causes a bunching on the microsecond scale which can be modeled with an exponential decay in time [151, 166]. From Figure 5.7(a) it is clear that the blinking dynamics for our investigated *QD* show a significant power dependence of its characteristic time [166], ranging from 16.1 μs to 1.6 μs. Nonetheless, by adding photoneutralization with a weak off-resonant visible light field, we are able to keep the impact on the overall "on"-time fraction η_{blink} under control. η_{blink} is approximately 0.3 in almost the entire interval of pump powers, as shown in Figure 5.7 (b).

$g^{(2)}(0)$ for different driving strengths: As stated before, we are interested in investigating how the multipair emission of the *QD* affects entanglement. The $g^{(2)}(0)$ has always been referred to as a measure of multiphoton contribution and, since the multipair emission potentially changes with the driving strength (the amount of excitation laser), we investigate the multipair emission versus different excitation powers. Figure 5.8 illustrates the measured second-order auto-correlation functions for different excitation powers up to above 5π-pulse areas using the two different normalizations $\tilde{g}^{(2)}(0)$ and $g^{(2)}(0)$. The values obtained for the X and XX lines are compatible within the margin of error (assuming a Poisson distribution of the coincidence counts). Clear maxima up to $(55.9 \pm 5.1) \cdot 10^{-3}$ are observed at even π-pulse areas. Similar oscillations have been experimentally observed in *QDs* [155], though only in resonantly driven two-level systems (2LS), in which the maxima stem from increased multiphoton emission. Specifically, the 2LS can spontaneously decay to the ground state instead of undergoing an even number of π rotations. In this case, if the excitation laser pulse is still present, a second excitation is possible [155]. This breaks the even

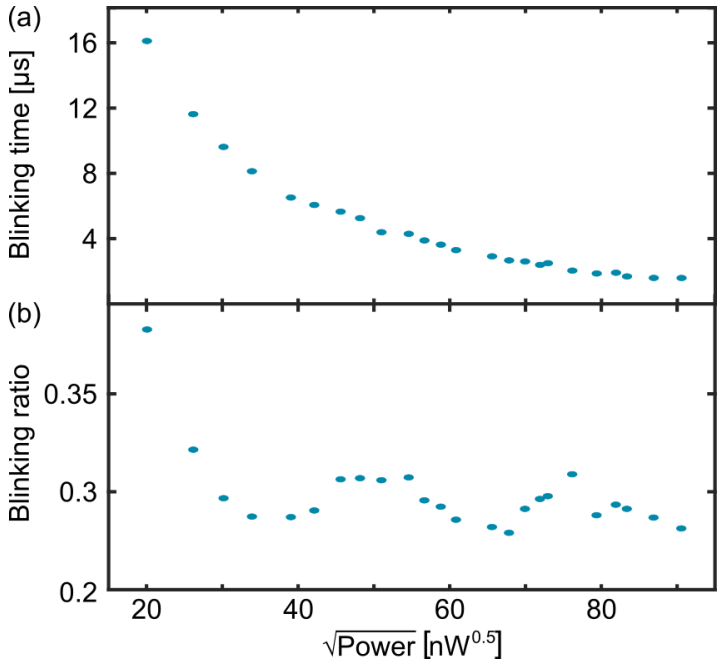

Figure 5.7. (a) The blinking time is extracted by an exponential decay fit of the cross-correlation histograms. (b) Blinking ratio η_{blink} extracted from intensity cross-correlation measurements with a correlation range of 1 ms for different excitation powers. From Supplementary of Ref. [95]

π-pulse area excitation into two uneven π-pulse area excitations with a radiative recombination in-between. Instead, for cascaded quantum ladder systems re-excitation is expected to be strongly suppressed [27]—as it can take place only when both the X and XX photons are emitted. Figure 5.8 may indicate that the multiphoton emission probability is non-negligible and oscillates with the driving strength. To show that this is not the case, we use an approach that does not rely on any assumption on the physical origin of the multiphoton emission. We infer its contribution from the experimental $g^{(2)}(0)$ of the photons emitted by the XX-X cascade and investigate its effect on the measured degree of entanglement.

Extracting multipair emission from the $\mathbf{g^{(2)}(0)}$ measurement data

We are now interested in extracting the real multipair contribution in the $g^{(2)}(0)$ measurement data. For this we derive the relevant figures of merit from a series of basic probabilities.

- η_{blink} is the probability that the QD is in its optically active ground state and can be excited via two-photon excitation.
- η_{prep} is the probability that a coherent excitation of the QD in the ground state promotes it to the biexciton state.
- η_{loss} is the probability that an emitted photon is detected.
- p_m is the probability that a successful cascaded photon emission is followed by re-excitation and a second cascaded photon emission.

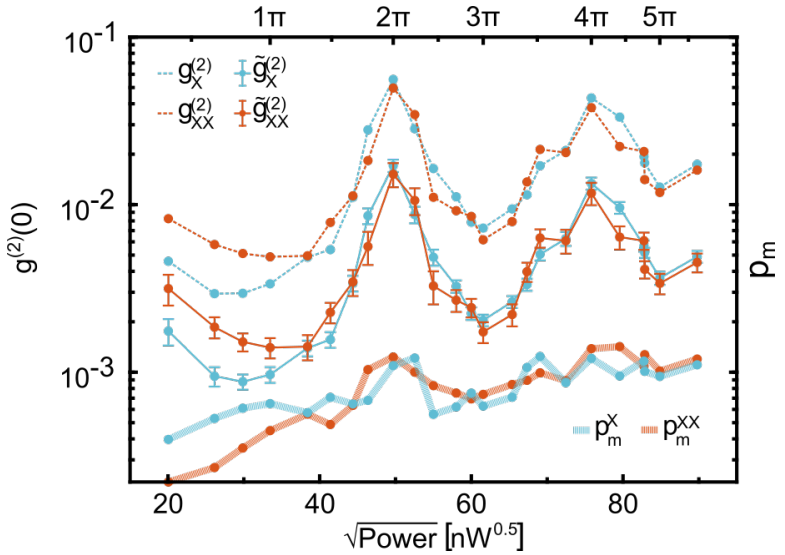

Figure 5.8. Measured $g^{(2)}(0)$, $\tilde{g}^{(2)}(0)$ and multiphoton probability p_m from the X and XX lines for different excitation powers. The $g^{(2)}(0)$ and $\tilde{g}^{(2)}(0)$ increase at even π-pulse areas in contrast to p_m. Adapted from Supplementary of Ref. [95]

For simplicity, we exclude multiple emission events beyond double, which should be a negligible fraction in all realistic cases considered. If we consider the photo-generation distribution, we can define p_1 (p_2) as the probability per excitation pulse of generating a single photon (two photons) per transition. It follows that $p_m = p_2/(p_1 + p_2)$.
Since we are interested in the specific effect of multiphoton emission, we disregard other sources of error, specifically we assume that background and dark counts are negligible as well as the detector dead time. These assumptions are good approximations for our experimental conditions.

We can combine this series of quantities to estimate the detection probabilities. We name C the event of a click on a detector. Under our assumptions, this event can be caused by either a photon from the first radiative cascade induced by the laser pulse or by a second radiative cascade if multiphoton emission takes place.

$p(C_{1^{st}})$ is the probability per single excitation pulse that the detector reveals a photon from the first radiative cascade.

$$p(C_{1^{st}}) = \eta_{blink}\eta_{prep}\eta_{loss}$$

$p(C_{2^{nd}})$ is the probability per single excitation pulse that the detector reveals a photon from a second radiative cascade, which also includes the probability of having multiphoton emission.

$$p(C_{2^{nd}}) = \eta_{blink}\eta_{prep}p_m\eta_{loss}$$

These events are not mutually exclusive, but can happen together with a probability given by

the following formula:

$$p(C_{1^{st}} \cap C_{2^{nd}}) = \eta_{blink}\eta_{prep}p_m\eta_{loss}^2$$

This probability depends linearly on the chance of creating two photons per transition with a single laser pulse and quadratically on losses, which are uncorrelated.

The overall probability of having a detection event is:

$$\begin{aligned} p(C) &= p(C_{1^{st}} \cup C_{2^{nd}}) \\ &= p(C_{1^{st}}) + p(C_{2^{nd}}) - p(C_{1^{st}} \cap C_{2^{nd}}) \\ &= \eta_{blink}\eta_{prep}\eta_{loss}(1 + p_m(1 - \eta_{loss})) \end{aligned}$$

We can also define the probabilities that the detector reveals a photon from the first radiative cascade but never together with a photon from a second radiative cascade (event $C'_{1^{st}}$) and viceversa (event $C'_{2^{nd}}$).

$$\begin{aligned} p(C'_{1^{st}}) &= p(C_{1^{st}}) - p(C_{1^{st}} \cap C_{2^{nd}}) \\ &= \eta_{blink}\eta_{prep}\eta_{loss}(1 - p_m\eta_{loss}) \\ p(C'_{2^{nd}}) &= p(C_{2^{nd}}) - p(C_{1^{st}} \cap C_{2^{nd}}) \\ &= \eta_{blink}\eta_{prep}p_m\eta_{loss}(1 - \eta_{loss}) \end{aligned} \tag{5.4}$$

These will later be useful for the estimation of the impact of multiphoton emission on the degree of entanglement.

Given these premises we can model the effect of multiphoton emission on the second-order auto-correlation function at zero-time delay. Later on, we go back to these premises to also model the polarization density matrix of the photon pair emitted during the *XX-X* cascade. This allows us to quantify the impact of the multiphoton emission on the density matrix and consequently on the figures of merit of entanglement.

The second-order auto-correlation function: The second-order auto-correlation function is experimentally obtained by measuring coincidence events in a *HBT* setup. We consider that the *QD* source is operated in pulsed mode. First, we estimate the probability per single excitation pulse that a coincidence is recorded within the temporal window of a single laser pulse, which we define as the zero-time delay condition. The probability that two photons emitted by the same optical transition (be it the biexciton-to-exciton state or the exciton-to-ground state) and excited from the same laser pulse arrive at the beam splitter of the *HBT* setup is given by $\eta_{blink}\eta_{prep}p_m\eta_{loss}^2$, where η_{loss} does not include photon losses due to the beam splitter. This event will give rise to a coincidence in 50 % of the cases, leading to the following probability of coincidence:

$$p(A \cap B, \Delta\tau = 0) = \eta_{blink}\eta_{prep}p_m\frac{\eta_{loss}^2}{2}$$

with A and B the events associated to a click on each of the two detectors of the HBT setup.

This probability needs to be normalized to be related to the auto-correlation function. As discussed previously in this Section, we can adopt two main approaches for the normalization. Here, instead of considering coincidences between uncorrelated events taking place in the limit of very long delays, we first derive the equations normalizing to the coincidences between events triggered by consecutive laser pulses. This is a common choice in the literature reporting experimental characterization of single emitters. One can easily switch between the two approaches by including the multiplicative factor η_{blink}, as in Eq. (5.3).

To estimate the probability of having coincidences between events triggered by consecutive laser pulses, we break it in two terms:

$$p(A \cap B, \Delta\tau = \pm T) = p(A)p(B|A, \Delta\tau = \pm T)$$

with T the period of repetition of the pump laser pulses. The probability that detector A clicks is given from the previous subsection ($p(C)$), including an additional factor 1/2 for the losses from the beam splitter.

$$p(A) = \eta_{blink}\eta_{prep}\frac{\eta_{loss}}{2}(1 + p_m(1 - \frac{\eta_{loss}}{2}))$$

The conditional probability that detector B clicks knowing that detector A clicked at the previous laser excitation comes from the previous formula by simply removing the η_{blink} term, since we assume that the QD is very likely in an "on"-state if it just emitted a photon.

$$p(B|A, \pm T) = \eta_{prep}\frac{\eta_{loss}}{2}(1 + p_m(1 - \frac{\eta_{loss}}{2}))$$

The probability per excitation pulse of a side-peak coincidence in the second-order auto-correlation histogram directly follows:

$$p(A \cap B, \pm T) = \eta_{blink}\eta_{prep}^2\frac{\eta_{loss}^2}{4}(1 + p_m(1 - \frac{\eta_{loss}}{2}))^2$$

Finally, we have a formula for the second-order auto-correlation function at zero-time delay normalized by the immediate side peaks.

$$\tilde{g}^{(2)}(0) = \frac{2p_m}{\eta_{prep}(1 + p_m(1 - \frac{\eta_{loss}}{2}))^2} \tag{5.5}$$

This formula lets us use the value of $\tilde{g}^{(2)}(0)$ to estimate the multiphoton component of the emission given that the probability of photon emission is known, an information which can be retrieved from *XX*-*X* cross-correlation measurements [167]. This estimate gives values very close to general upper bounds derived in the literature, namely Eq. (16) from Ref. [168] and Eq. (20-21) from Ref. [169]. In our experiment, η_{loss} is about 0.005, therefore we can approximate the term to $(1 - \eta_{loss}/2)$ to 1 and obtain the following formula:

$$\tilde{g}^{(2)}(0) = \frac{2p_m}{\eta_{prep}(1+p_m)^2}$$

If we further assume that $p_m << 1$ (as valid for the data collected in our study), the formula further simplifies to:

$$\tilde{g}^{(2)}(0) = \frac{2p_m}{\eta_{prep}} \tag{5.6}$$

An immediate consequence of Eq. (5.5) is that without changing the multiphoton emission component at the source, the $g^{(2)}(0)$ is inversely proportional to the preparation fidelity η_{prep}. This contribution is to be considered when analyzing the multiphoton component in relation to Rabi oscillations as a function of the excitation power.

Preparation fidelity: In order to extract the multiphoton contribution from our measurements, we first need to determine the preparation fidelity for different excitation pulse areas. The preparation fidelity η_{prep} is the parameter that describes the efficiency of the excitation scheme, which strongly varies in a resonant excitation scheme. This makes it vital to study the multipair emission effect for the whole power dependence, even π-pulse areas included. η_{prep} is often inferred from the power dependence of the photoluminescence as in Figure 5.2, using a model to extract the occupation number of the *XX* state. Here we opt for a different approach, which requires fewer assumptions and prevents us from neglecting power-dependent blinking dynamics. We estimate η_{prep} from intensity cross-correlation measurements between *X* and *XX* photons [151, 167], using the setup of Figure 5.3 without polarization selection. The XX-X cross-correlations histograms, normalized to the side peaks (12.5 ns), for π- and 2π-pulse areas are shown in Figure 5.9. When the preparation fidelity is smaller than 1, the probability of finding a *X* photon is higher when an *XX* photon was detected from the same radiative cascade. We can now compare the cross-correlation histogram peak between the *X* photons at zero-time delay with the *XX* photons from the same radiative cascade ($I_{X,XX}(t_0)$), and the cross-correlation peak between the *X* photons at zero-time delay with the *XX* photon from a subsequent laser pulse ($I_{X,XX}(t_{\pm 1})$), see Figure 5.9(a). The ratio between the photons belonging to subsequent laser pulses and the zero-time delay peaks $\frac{(I_{X,XX}(t_{-1})+I_{X,XX}(t_{+1}))/2}{I_{X,XX}(t_0)} = \eta_{prep}$ is the preparation fidelity. η_{prep} as a function of the pump power is reported in Figure 5.9(b), displaying the expected population oscillations, with the highest (lowest) value of 0.93 (0.14) at π- (2π-)pulse area. The highest preparation fidelity is comparable to those published for similar GaAs/AlGaAs *QDs* [23].
This method does not require any assumption on how to model the damping of the Rabi oscil-

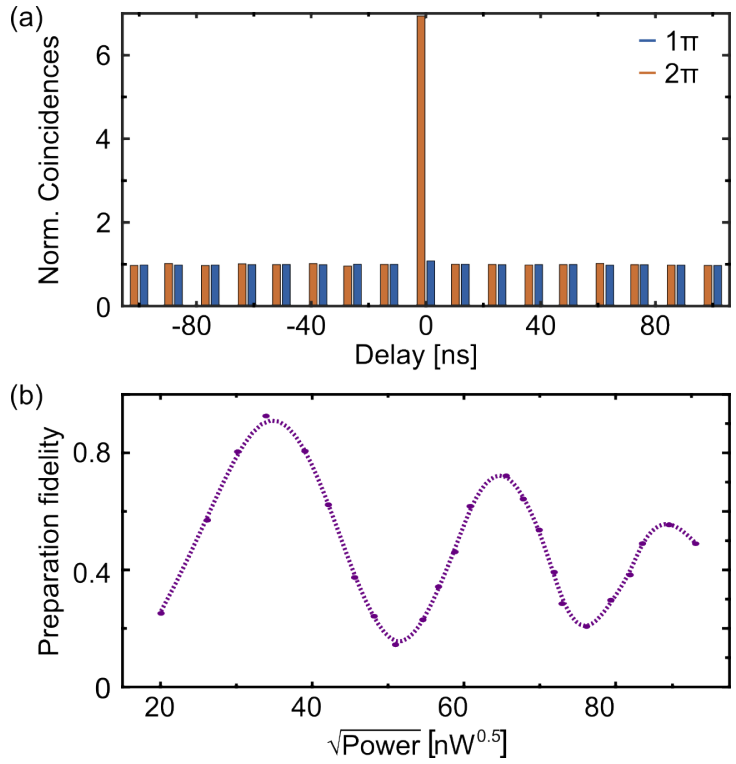

Figure 5.9. (a) Coincidence histograms between X and XX photons, normalized to the side peaks (12.5 ns), for π- and 2π-pulse area excitation. (b) Measured preparation fidelity (dots) for different pumping regimes, with a spline interpolation to visualize the oscillations as a guide to the eye. The error bars are within the marker size. From Ref. [95]

lations. Moreover, power-dependent changes of η_{blink} also affect the photoluminescence intensity. They should not be neglected when inferring information about the coherent coupling between ground level and XX state. In our investigated QD, the blinking dynamics show a significant power dependence, so that the characteristic time of the process decreases by almost an order of magnitude in the studied power range. Nonetheless, by photoneutralization with a weak off-resonant visible light field, we are able to keep the impact on the overall "on"-time fraction η_{blink} under control.

Given these findings, it is apparent from Eq. (5.6) that the oscillations in the $g^{(2)}(0)$ are not necessarily related to variations in the multipair emission probability but rather to oscillations in the preparation fidelity. Using the measured values of $g^{(2)}(0)$, η_{prep}, and η_{blink}, Eq. (5.6) can be exploited to directly calculate p_m, without any specific assumption on the physical origin of the multipair component. The resulting continuous line in Figure 5.8 highlights that the fraction of emission events related to multipair emission does not noticeably vary with the pump power, only slightly increases with the pulse area. This is potentially related to an increasing background due to the approximately linear increasing excitation laser power.

In a next step we are interested in evaluating the effect of multipair emission on the density matrix. To do so, we extend the model and again use the series of basic probabilities to derive the contribution to the density matrix.

5.1.3 Modeling the multipair effects on entanglement

We now describe the effect of multiphoton emission on the polarization state of the photons emitted in the *XX-X* radiative cascade. Multiphoton emission introduces undesired coincidence events which are totally uncorrelated in polarization. The density matrix of the photon-pair polarization state can be modeled as a mixture of the entangled state emitted from the *XX-X* cascade—ideally $|\phi^+\rangle\langle\phi^+|$, ρ_0 keeping into account other coexisting decoherence mechanisms [100]—plus a noise term,

$$\rho = (1-k)\frac{\mathbb{I}}{4} + k|\phi^+\rangle\langle\phi^+| \tag{5.7}$$

where $\mathbb{I}$ is the identity matrix and k is the fraction of photons that both come from the same radiative XX-X cascade with respect to the total number of detected pairs.

In the following discussion, we derive k from the series of basic probabilities introduced when deriving the multiphoton probability from the auto-correlation measurements.

In the case of the density matrix we have two separate detecting apparatuses—may those be composed of waveplates and either a polarizing beam splitter plus two detectors or a single detector with a linear polarizer in front—, one for the biexciton-to-exciton transition (XX events) and the other for the exciton-to-ground state transition (X events). We assume that photons from the two transitions of the cascade are always emitted together and that they experience equal losses in the setup. This is usually a reasonable assumption for the *QDs* considered in our study, since non-radiative mechanisms are negligible and the wavelength of the two transitions is similar, so that we observe similar count rates on the detectors. Given these assumptions, the various detection probabilities introduced at the previous Section can be directly applied here. For example,

$$\begin{aligned} p(X) &= p(XX) = p(C) \\ &= \eta_{blink}\eta_{prep}\eta_{loss}(1 + p_m(1-\eta_{loss})) \end{aligned}$$

From the definition of k, we can estimate it as the probability ratio between the coincidences induced by photons emitted by the same radiative cascade, with no extra photon triggered by the same laser pulse arriving at the detectors, and the complete set of possible coincidence events.

$$k = \frac{p(X'_{1^{st}} \cap XX'_{1^{st}}) + p(X'_{2^{nd}} \cap XX'_{2^{nd}})}{p(X \cap XX)} \tag{5.8}$$

In this way, we assume that all the excluded coincidence events contribute with uncorrelated noise to the matrix. This is true for coincidences between one photon from the first emitted cascade (e.g., $X'_{1^{st}}$) and a photon from a second re-excited cascade (e.g., $XX'_{2^{nd}}$). Instead, this assumption does partially underestimate the residual polarization correlation observed for coincidence events when three or four photons arrive on the detectors. However, this contribution is negligible if the

term η_{loss} is significantly smaller than 1, as in the case of our experimental conditions.

We start from the probability of coincidence only from the first emitted cascade, which is the major contribution.

$$p(X'_{1^{st}} \cap XX'_{1^{st}}) = p(X'_{1^{st}})p(XX'_{1^{st}}|X'_{1^{st}})$$

To evaluate the second term of the expression, we start from the unconditional formula in Eq. (5.4) and consider the conditional probability for each of its parts. Knowing that $X'_{1^{st}}$ has taken place, a photon pair has been emitted, therefore the blinking and preparation terms are removed. The probability of photon loss is unchanged since this independently affects photons from different optical transitions. The probability of multiphoton emission (we label the event as m) is influenced in a way that can be estimated using Bayes' theorem. In fact, we can calculate what is the probability that only a photon from the first cascade is detected on the exciton channel knowing a radiative cascade was successfully induced (event $X'_{1^{st}}|prep$) and that it also resulted in a double excitation (event $X'_{1^{st}}|m$).

$$\begin{aligned}
p(m|prep) &= p_m \\
p(X'_{1^{st}}|prep) &= \eta_{loss}(1 - p_m\eta_{loss}) \\
p(X'_{1^{st}}|m) &= \eta_{loss}(1 - \eta_{loss}) \\
p(m|X'_{1^{st}}) &= \frac{p(X'_{1^{st}}|m)p(m|prep)}{p(X'_{1^{st}}|prep)} \\
&= \frac{p_m(1 - \eta_{loss})}{1 - p_m\eta_{loss}}
\end{aligned}$$

Using for each term of $XX'_{1^{st}}$ the probability conditioned on event $X'_{1^{st}}$, the following result is obtained:

$$\begin{aligned}
p(XX'_{1^{st}}|X'_{1^{st}}) &= \eta_{loss}(1 - p(m|X'_{1^{st}})\eta_{loss}) \\
p(X'_{1^{st}} \cap XX'_{1^{st}}) &= \eta_{blink}\eta_{prep}\eta_{loss}^2(1 - p_m\eta_{loss}(2 - \eta_{loss}))
\end{aligned}$$

The other terms of Eq. (5.8) can be estimated following a similar procedure.

$$\begin{aligned}
p(X'_{2^{nd}} \cap XX'_{2^{nd}}) &= \eta_{blink}\eta_{prep}p_m\eta_{loss}^2(1 - \eta_{loss})^2 \\
p(X \cap XX) &= \eta_{blink}\eta_{prep}\eta_{loss}^2(1 + p_m(3 - \eta_{loss})(1 - \eta_{loss}))
\end{aligned}$$

Finally, we obtain an expression for k.

$$k = \frac{1 + p_m(1 - 4\eta_{loss} + 2\eta_{loss}^2)}{1 + p_m(3 - 4\eta_{loss} + \eta_{loss}^2)}$$

It is worth noticing that in the limit of $\eta_{loss} << 1$, the formula reduces to

$$k = \frac{(1 + p_m)}{(1 + 3p_m)} \tag{5.9}$$

This matches the intuitive expectation of having at the numerator the coincidences from the same cascade and at the denominator all the possible combinations, given that all the coincidences involving one or more photons from a re-excitation event must include in their probability an additional term p_m.

Knowing how multiphoton emission affects the auto-correlation and entanglement measurements, it is possible to relate these two physical quantities. More specifically, the second-order auto-correlation function can be used to obtain information about multiphoton emission and allows to predict its effect on the polarization density matrix of the *XX*-*X* radiative cascade.

Combining Eq. (5.7) and (5.9) in the limit of $p_m << 1$ and $\eta_{loss} << 1$—a good approximation for the experimental conditions of our work—returns the very simple relationship:

$$k \approx 1 - \eta_{prep}\tilde{g}^{(2)}(0) = 1 - \eta_{prep}\eta_{blink}g^{(2)}(0) \tag{5.10}$$

The second equality has been obtained using Eq. (5.3).

In this limit the expression is equivalent to the one obtained for unpolarized and uncorrelated background radiation [151].

The estimate for k is plugged into Eq. (5.7) to simulate the excitation power dependence of the density matrix. The entanglement related figures of merit, such as the fidelity to the expected maximally entangled Bell state and the concurrence, are directly derived from the density matrix.

5.1.4 Multipair effects on entanglement

Knowing now the expected contribution on entanglement, we are interested in measuring it. To do so, we perform polarization-resolved *XX*-*X* cross-correlation measurements to reconstruct the two-photon density matrix using the setup from Figure 5.3. Rotations in the polarization state induced by optical components are compensated using a set of linear waveplates to maximize the fidelity to the expected Bell state $|\phi^+\rangle$ [34]. The density matrix is reconstructed from 36 correlation measurements using quantum state tomography and maximum likelihood estimations [143]. Figure 5.10 shows the resulting real part of the density matrix at π-pulse area. The imaginary part does not contain significant terms (no matrix element is above 0.045 in absolute value). Furthermore, the fidelity to $|\phi^+\rangle$ is 0.93 ± 0.01, while the concurrence is 0.89 ± 0.02, values that are comparable with the literature [80] and bested only by those obtained with strain-tunable *QDs* [37]. We note that the influence of non-measurable *FSS* (below 0.5 μeV) should affect the fidelity by less than

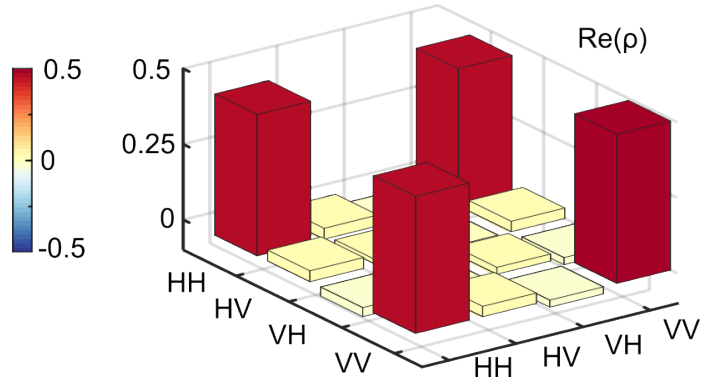

Figure 5.10. Real part of the density matrix of the XX-X photon polarization state measured at π-pulse area. Adapted from Ref. [95]

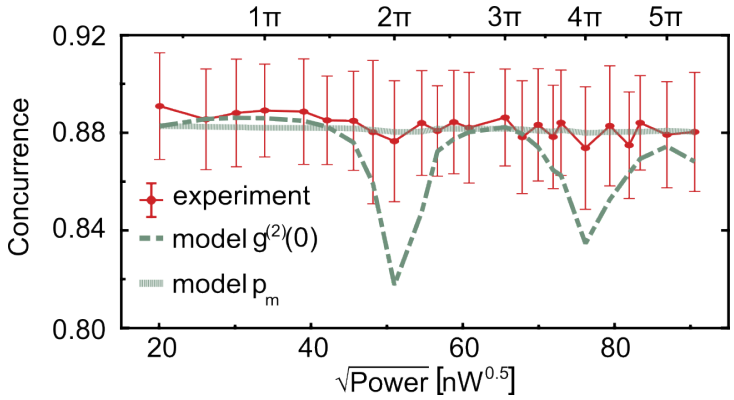

Figure 5.11. Concurrence for different excitation powers. Experimental data (red) are compared with the predictions of Eq. (5.12) (dashed green line) and Eq. (5.10) (our model, continuous green line). The error bars in the modeled values, estimated from the measured multiphoton probability using a Monte Carlo simulation, are within the line thickness. Adapted from Ref. [95]

1 % [34]. Additionally, we characterized the waveplates retardance and detector dark counts and simulated their impact on the density matrix estimation to conclude that their impact amounts to less than 0.7 % on the Bell-state fidelity. The error bars are estimated with a Monte Carlo method assuming a Poisson distribution of the coincidence counts.

The measurements show no significant variation of the concurrence at 2π-pulse area and across the whole range of powers investigated in this work, as shown in Figure 5.8. This result is in stark contrast with the behavior of SPDC entangled photon sources [20]. Furthermore, it clashes with the common idea that multiphoton emission, whose presence was associated with the non-zero $g^{(2)}(0)$ values reported in Figure 5.8, affects the degree of entanglement. Specifically, the measured entanglement would be degraded by erroneous detection events of an X and XX photon belonging to different photon pairs from subsequent (thus uncorrelated) cascades. In previous works to ours, multiphoton components have been included in the density matrix ρ directly using knowledge of the $g^{(2)}(0)$ in the following way [37, 162]:

$$\rho = \frac{1}{4}(1-k) * \mathbb{I} + k\rho_0 \tag{5.11}$$

$$1 - k = \frac{1}{2}(g_X^{(2)}(0) + g_{XX}^{(2)}(0)) \tag{5.12}$$

with ρ_0 being the density matrix neglecting accidentals due to multiphoton components, k being the fraction of photon pairs that come from a radiative XX-X cascade with respect to the total number of detected pairs. According to this model, a link between concurrence and pulse area should be visible, as indicated by the dashed line in Figure 5.11, obtained using Eq. (5.12) and the $g^{(2)}(0)$ measurements reported in Figure 5.8. The discrepancy is especially evident at even π-pulses, which motivates the effort to investigate a wide range of excitation powers. A clear inconsistency between the measurements and this commonly used theory is observed.
This raises the question: Can the $g^{(2)}(0)$, as measured via HBT, actually help to estimate the effect of multiphoton emission on the density matrix? We address the matter using a probability-based model to estimate how multiphoton emission affects the measurements of $g^{(2)}(0)$ and ρ.

Our simple probabilistic model Eq. (5.10), readily explains why the degree of entanglement does not oscillate with pump power as visible in the $g^{(2)}(0)$. The density matrix is proportional to p_m and thus the entered $g^{(2)}(0)$ values have to be normalized to η_{prep}. Plugging in the numbers measured from the previous experiment, Figure 5.8. Moreover, the quantitative multiphoton contribution appears negligible, as the level of multiphoton emission estimated at maximum source brightness (π-pulse area) is $p_m = (5.6 \pm 0.6) \cdot 10^{-4}$, corresponding to an absolute value $p_2 = (1.5 \pm 0.3) \cdot 10^{-4}$. These values applied to an ideal Bell state would result in a concurrence of 99.8 %. The lower concurrence measured in our experiment has to be attributed to another physical reason, arguably cross-dephasing mechanisms in the bright exciton state for this particular *QD* [151]. Ultimately, using Eq. (5.10) in combination with Eq. (5.12), where ρ_0 is the density matrix measured at minimum excitation power, we obtain an excellent agreement between our model and the experimental data for the concurrence reported in Figure 5.11.

5.1.5 Discussion

We demonstrate that excitation conditions and measurement settings are important aspects and can induce deceiving multiphoton contributions in the assessment of bipartite entanglement. Consequently, great care has to be taken when performing $g^{(2)}(0)$ measurements without polarization compensation. Several steps can be applied to remove instrument related errors, such as afterpulsing of the detectors. Additionally, the excitation laser needs to be thoroughly removed, in our case in excitation as well as in collection. Depending on the application, moderate spectral filtering gives another option to access the intrinsic $g^{(2)}(0)$ from the photon pair generation process. The ratio between the signal coming from the radiative cascade and background emission is an important factor, which can be especially relevant when the photon pair generation is less efficient, and the excitation power is higher. This matches the case for resonant excitation at 2π-pulse area,

which benefits from a spectral selection of the *XX* line closer to its value of emission bandwidth. Overall, we have shown that strong antibunching with a $g^{(2)}(0)$ value of $2.4 \pm 0.1 \times 10^{-3}$ can be observed without the need of polarization suppression, thus in a scenario compatible with quantum polarization-state tomography of the photon pairs emitted from the *QD* source.

These results enabled the demonstration that the effect of multiphoton emission on the degree of entanglement of photons emitted by resonantly-driven *QDs* is negligible and, contrarily with the behavior reported for single-photon generation in 2LS [170], does not vary significantly with pump power. This occurs despite we observe oscillations in the $g^{(2)}(0)$ by more than one order of magnitude. We illustrate that these variations are not necessarily related to the variation of the multiphoton emission probability, but rather to variations of the preparation fidelity of the excited state. With the support of a probability-based model, we identify the actual contribution of the relative multiphoton emission p_m, as estimated from the $g^{(2)}(0)$, which enters the simulation of the quantum tomography results and successfully reproduces the experimental data.
This work thus tackles a fundamental obstacle for state-of-the-art entangled photon sources based on SPDC: the relationship between pump power, brightness, and entanglement quality. Even though the absence of a trade-off between brightness and entanglement due to the multiphoton emission has long been a motivation for developing *QD*-based sources, we finally provide a thorough experimental study demonstrating that multiphoton emission is negligible and does not negatively affect the generated entangled states across a wide range of excitation powers in *TPE*. The result strengthens the case for *QDs* providing highly entangled photons for complex quantum information protocols. The entanglement fidelity reported in this work was yet below unity, an evidence attributed to residual decoherence mechanisms between the bright exciton states [37]. This effect can be significantly lower in selected *QDs* [37], and could potentially be reduced with the help of photonic cavities to shorten the lifetime of the optical transition [29, 30]. However, shortening the lifetime, especially the closer they get to the excitation laser pulse length, the higher is the laser-induced Stark effect. This effect of the excitation laser pulse length on entanglement is discussed in the following section.

5.2 Entanglement degradation due to optical Stark effect

One factor that was always ignored so far is an excitation laser-induced Stark effect. Recently, Seidelmann et al. [156] demonstrated theoretically that the pulsed excitation laser in *TPE* during its presence induces an energy splitting due to the Stark effect. The magnitude of the energy splitting E_S of the pulsed excitation laser can be approximated with the formula:

$$E_S = \frac{\hbar\pi}{\Delta\tau_L} \tag{5.13}$$

where $\Delta\tau_L$ the is the pulse length of the laser. Using a commonly set excitation pulse length for *TPE* of 10 ps, the energy splitting accounts to 200 μeV. This is two orders of magnitude higher than potential intrinsic *FSS*. But, contrary to *FSS*, this Stark shift and the resulting splitting of energy

levels is only present during the presence of the excitation laser. Hence, it only affects photons that are emitted during the presence of the excitation process, and the other photons are not afflicted. Consequently, this excitation laser-induced splitting depends both on the biexciton state lifetime and the laser pulse length, more specifically on the ratio between those two. The shorter the biexciton lifetime, the more photons emitted by the *QD* experience this laser-induced Stark shift. When using photonic cavities exhibiting Purcell enhancement to lower dephasing effects, the lifetime of the biexciton and exciton states are shortened, which exposes more emitted photons to the laser-induced Stark effect.
We can estimate the laser-induced Stark effect on the concurrence considering typical lifetimes of GaAs/AlGaAs *QDs* (roughly 200 ps and 100 ps for the X and XX), and a typical set laser pulse length (10 ps). Assuming that there are no other *QD* intrinsic entanglement detrimental effects and we only look at the laser-induced Stark effect, we can use the following formula [156]:

$$C = 1 - 2\frac{\gamma_B FWHM}{8}\exp[-\frac{\gamma_B FWHM}{4}] \tag{5.14}$$

γ_B is the biexciton decay rate.
Using the values from before we estimate a concurrence of 0.976, which is close to the maximally measured value of 0.97(1) for GaAs/AlGaAs *QDs* [37]. This result raises the question if the *QD* potentially had perfect entanglement and only a laser-induced Stark shift was limiting this claim. To answer this question, a thorough investigation is needed. But first, the effect of an excitation laser-induced Stark shift splitting would need to be demonstrated experimentally.

In order to visualize the effect we can extract from Eq. (5.14) two setscrews, the excitation pulse length and the lifetime of the XX transition. By changing one of these two and fixing the other we should see an effect on the entanglement. Despite the simple concept that the concurrence changes with the pulse length of the excitation laser, it is not so easily performed experimentally. Let's start with discussing the first idea, changing the laser pulse length.
In our experimental setup the excitation laser, a fs pulsed laser from Coherent, is sent to a custom made 4f-pulse shaper to increase the pulse length to roughly 10 ps for optimal excitation conditions. To achieve this, the laser is sent to a grating, dispersing the light in its different wavelength components. The dispersed light is then focused on a slit, which can be moved laterally to select a certain wavelength and the slit size can be adjust to create a certain pulse length. Note, the slit size is inverse proportional to the resulting pulse length. With the current experimental setup we can change the pulse length of the laser from 2 ps to 24 ps by closing the slit from 700 μm to 0 μm. Taking now the two extreme slit size settings and typical lifetimes of GaAs/AlGaAs *QDs* from before, we can estimate the effect of entanglement we would expect from our measurements using Eq. (5.14). The expected concurrence drops from 0.9950 to 0.9457 for a 2 ps pulse length to 24 ps pulse length. This drop is only minimal and considering entanglement values of as-grown *QDs* of roughly 0.94 [95], this investigation may not give conclusive results.
For this reason we need the help of the second approach, lowering the lifetime of the source. A shorter lifetime would let our largest experimentally achievable pulse length have a more significant effect. For example, let's consider a Purcell factor of 10, which means shortening the lifetime of the

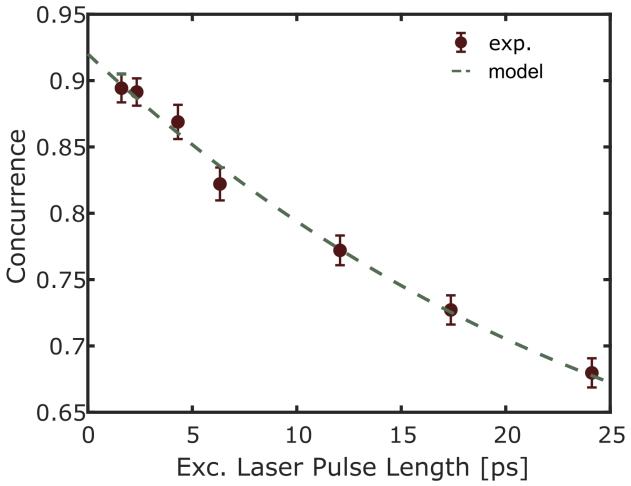

Figure 5.12. Concurrence vs. excitation laser pulse length. Increasing the pulse length from 2 ps to 24 ps decreases the concurrence of the emitted entangled photon pair. The experimental drop follows the theoretical predictions of a laser-induced Stark effect in Ref. [156].

transitions by a factor 10. When we estimate the concurrence again using the same pulse length extrema, but the shortened lifetimes, we get a concurrence drop from 0.9524 to 0.6764 by increasing the pulse length from 2 ps to 24 ps. Using these shortened lifetimes results in a significant drop of the concurrence, which can potentially be visible in an experimental condition. The only challenge now is that we need a GaAs/AlGaAs *QD* having a Purcell factor of 10, or comparable. Second-order Bragg gratings are compatible with the broadband emission of the GaAs/AlGaAs *QD* and have been demonstrated with Purcell factors up to 11.3 on InGaAs *QDs*. On the same sample also the highest entanglement fidelity of 0.90(1) has been measured. In collaboration with teams at the University of Linz (Austria) and Würzburg (Germany), my colleague fabricated a source that has a Purcell factor of 4.7, with resulting (measured) lifetimes of 53 ps and 35 ps for the X and XX states, respectively. We used this source and perform quantum state tomography on the entangled photons under resonant *TPE* for different excitation laser pulse lengths within the range stated before.

As visible in Figure 5.12 we can verify experimentally that the concurrence is degrading with longer pulse duration. The lower experimental starting point of the concurrence is accounted to dephasing effects, potential non-measurable (below 0.5 μeV) *FSS*, and the finite excitation pulse length. This lower starting point due to *FSS* and dephasing effects, can be accounted for in the model (Eq. (5.14)) by a multiplicative factor. Using this extension and modeling the expected concurrence, we can even demonstrate that the degradation of the measured concurrence due to increasing pulse length follows the theoretical prediction of Ref. [156].

By reverse engineering this idea of degrading the entanglement with longer pulse lengths, it should be possible to increase the concurrence by using shorter excitation pulses. Using this trick, and slightly shorten the pulse length to 2.3 ps (compared to our typical setting of 10 ps) by increasing the slit size to 450 μm, we could measure the highest entanglement value of a *QD* in a

second-order Bragg grating. This was performed on a different *QD* with lifetimes of 41 ps and 22 ps for X and XX state, where the fidelity (concurrence) reached 0.9504(5) (0.908(1)), which are corrected for an increased multiphoton contribution. It has to be mentioned that lowering the excitation laser pulse length, means increasing its spectral width. This makes it difficult to properly remove the laser for these particular wavelengths, which might cause potential clicks at the detectors, which are uncorrelated to the signal. Additionally, increasing the spectral width towards the 2 nm boundary set by the binding energy enhances the potential to directly excite the unwanted X state. Hence, in experimental conditions with pulse lengths shorter than 2-3 ps becomes the *TPE* scheme inadequate [156].

In conclusion with these preliminary measurements we could demonstrate an effect of the excitation laser pulse length on entanglement. More precisely, the effect follows the theoretical prediction of an induced Stark effect, underlining the theoretical expectations. To prove the full impact of this excitation laser-induced Stark shift calls for further, more in-depth investigations, as excitation polarization and power dependencies. However, these preliminary measurements demonstrate the validity of this theory and point out that this entanglement degradation should be taken into account when measuring the entanglement of GaAs/AlGaAs *QDs* under resonant *TPE*. More importantly, it can be mitigated by adjusting to the optimal pulse length.

Chapter 6

Quantum key distribution using GaAs/AlGaAs quantum dots

Quantum key distribution has some fundamental advantage over our current classical encryption techniques, the possibility of theoretical full security, which has been discussed in detail in Section 2.1. *QKD* protocols based on entanglement, in particular, exhibit the advantage, that even though the transmission rate is theoretically the same as for single qubit protocols, the communication distance is twice compared to the single photon case, because the entangled photon source can be placed in between the communicating parties. Additionally, entangled photons bring the advantage that there are concepts to build up quantum networks with entangled photons as the core element. These quantum networks use an entangled photon source as a node and transform the information to the next node using an operation called entanglement swapping. This brings us already to the last advantageous part of entanglement-based *QKD*, the possibility of device independence. Device independence is the process when the security is guaranteed even in presence of an untrustworthy entanglement source or detection equipment. This is a parameter very important not having to make the nodes trusted and consequently protected, granting even stricter security standards. Current standard-bearers of *QKD* would not place full device independence in real world applications, underlying the potential of entanglement-based *QKD*.

In this chapter, I presents the successful implementation of an in-fiber and free-space link *QKD* experiment, based on entangled photons from a GaAs *QD*. The results even demonstrate continuous key exchange over the course of three days, exposing the key distribution to real-life environment including sunlight and mild rain. This emphasizes that *QDs* have the potential to be core elements of quantum communication. First, I will introduce the implemented protocol with their figures of merit and the characteristics of the used entangled photon source. Then the experimental setup is explained step-by-step. Especially the free-space optical link tags along new challenges, as stabilization or higher background light, which are disassembled and each briefly discussed. Afterwards an overview on the data acquisition and the consecutive post processing steps on the data to extract the final secret key is explained. As in the optical system, approaching real-life settings like free-space links request new solutions as synchronizing the two acquisition

components. All these chapters should provide the foundation to understand the experimental results presented in the next two sections. The results contain, the first demonstration of free-space entanglement-based communication with GaAs *QDs*, and the follow-up experiment, a continuous 3-day key exchange dealing with more severe environmental effects as sunlight and mild rain. At the end I briefly give an outlook on suggested improvements to the setup and acquisition, to enhance the figures of merit.

6.1 Protocol

We use a protocol derived from the Ekert91 protocol, the asymmetric Ekert91 protocol proposed by A. Acín and coworkers. This scheme has the advantage that it reduces the number of measurement bases and can be extended to device-independent operations [55].
The scheme works the following way: Alice and Bob both receive one photon from an entangled photon pair and perform a measurement on a basis randomly chosen from a given measurement bases set. For polarization entangled photons in the $|\phi^+\rangle = \frac{1}{\sqrt{2}}(|HH\rangle + |VV\rangle)$ the sets of bases are $\{A_k, A_0, A_1\} = \{H/V, -22.5°/67.5°, -67.5°/22.5°\}$ and $\{B_0, B_1\} = \{H/V, -45°/45°\}$. H/V are horizontal and vertical linear polarization in the laboratory frame of reference. The other basis are given as angles with respect to H. When Alice and Bob measure the same basis ($\{A_k, B_0\}$) the result gets added to the key. By collecting the correlations between the channels we can check the important parameters for the success of the protocol, for example the Bell parameter and the Quantum Bit Error Rate.

Bell parameter: The Bell parameter gives the information for eavesdropping attempts, based on the check of the violation of the Bell inequality $\mid S \mid \leq 2$. We can extract the parameter S from the Clauser-Horne-Shimony-Holt (CHSH) definition [53]:

$$S = E(A_0, B_0) + E(A_0, B_1) - E(A_1, B_0) + E(A_1, B_1) \tag{6.1}$$

where $E(A_i, B_j)$ is the correlation coefficient for the measured basis A_i, B_j. The expectation value is extracted from the coincidences $n_{i,j}$ recorded for all possible combinations of $\{i, \bar{i}, j, \bar{j}\}$,:

$$E(A_i, B_j) = \frac{n_{i,j} + n_{\bar{i},\bar{j}} - n_{\bar{i},j} - n_{i,\bar{j}}}{n_{i,j} + n_{\bar{i},\bar{j}} + n_{\bar{i},j} + n_{i,\bar{j}}} \tag{6.2}$$

with $\bar{i}$ ($\bar{j}$) being the perpendicular basis to i (j).

Quantum Bit Error Rate: The expected differences of the raw key rates can be estimated by the Quantum Bit Error Rate (*QBER*). Here, we look at the discrepancy of the key channel ($E(A_k, B_0)$) from ideal operation, which corresponds to 1.

$$QBER = \frac{1 - E(A_k, B_0)}{2} \tag{6.3}$$

FSS	$g_X^{(2)}(0)$	$g_{XX}^{(2)}(0)$	Fidelity	Preparation fidelity	on-time fraction
QD First field QKD - Free-space link					
0.35	0.0040(4)	0.0045(4)	0.958	0.943(3)	0.22
QD First field QKD - Fiber-based link					
0.85	0.0034(2)	0.0041(3)	0.941(10)	0.90(1)	0.26
Daylight QKD - Free-space link					
1.0(5)	0.022(2)	0.013(1)	0.942(1.3)	0.86	0.26

Table 6.1. QD parameters from the different *QKD* experiments. Note, the $g^{(2)}(0)$ values are dominated by incomplete suppression of the laser light and after-pulsing of the detectors [164]. One reason for the lower entanglement fidelity is the reported *FSS* of the *QDs*.

6.2 Source

The polarization-entangled photon source used for the *QKD* experiments in this thesis is a single GaAs/AlGaAs *QD*, which is placed at the middle of a planar *DBR* cavity. The geometry of the cavity is designed to enhance the emission in the collection direction, so the top of the sample. A detailed explanation on the sample structure is provided in Section 3.2. Additionally, a zirconia Weierstrass solid immersion lens is placed on top to reach an over all extraction efficiency of 10 %. The final sample assembly is depicted in Figure 3.7. The selected *QD* in the sample emits entangled photons via the *XX*-*X* cascade. Since a different *QD* was used for each experiment, the relevant *QD* values for *QKD* are reported in Table 6.1.

6.3 Experimental setup

The experimental setup imitates potential future communication solutions. On the one hand, in an urban environment a fiber-based communication solution is favorable, since they are scalable and only exhibit moderate losses for short distance. On the other hand, over long distances, losses would prohibit the advantage of using fibers, and a free-space link represents the best choice for communication, because of its low-signal attenuation [154]. Additionally, free-space links provide the possibility of sending complex states, such as the orbital angular momentum of light.
These two communication infrastructure concepts are comprised in two urban communication scenarios within the campus of Sapienza University of Rome, namely, a single-mode fiber of 250 m between two laboratories and a free-space link covering a distance of approximately 270 m between two buildings. The latter is illustrated in Figure 6.1.

The *QD* is placed in a 4 K low-vibration closed-cycle He cryostat in one of the two buildings. A Ti:Sapphire femtosecond laser with 320 MHz and 200 μeV spectral linewidth – adapted with delay lines and a custom-built pulse shaper – drives the source via resonant two-photon absorption. The excitation/detection path is the same as explained in Section 4.1, with the difference of using an aspheric lens with a numerical aperture of 0.5 to focus the laser and collect the emitted *QD* signal.

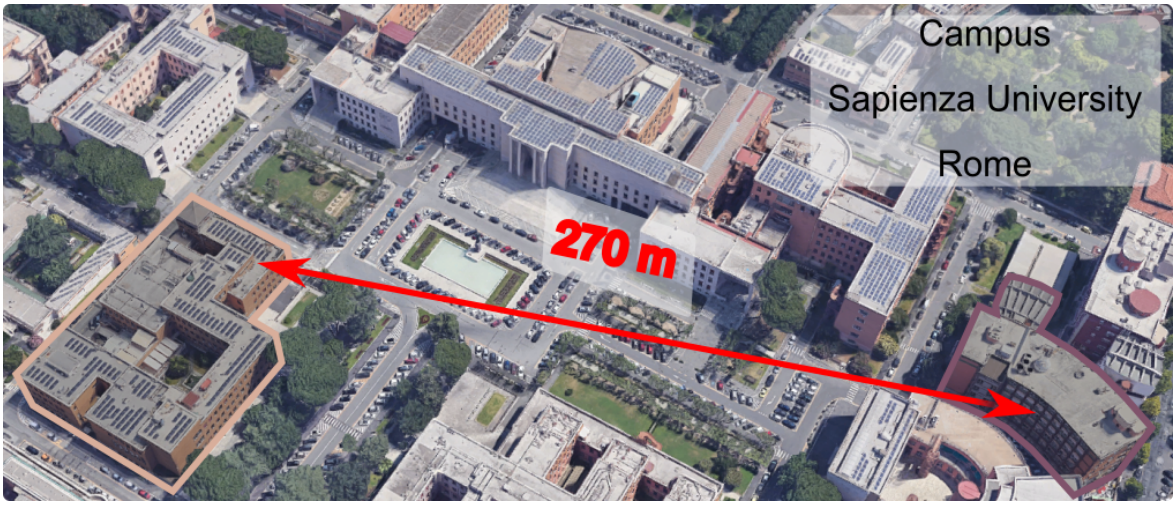

Figure 6.1. Image of Sapienza's free-space *QKD* link. The two physics buildings are connected via a direct 270 m free-space link, illustrated by the red line.

The X and XX signal of the *QD* is sent to the analyzing setup with two *NF* in reflection. The X photons are sent to Bob's (Alice's) analyzer, which is placed in the same laboratory. The XX photons are sent to Alice's (Bob's) analyzer in the other laboratory via a fiber-based system or the free-space link to a different building. Please note, for the first *QKD* experiment, Bob was on the sender's side and Alice on the receiver's side. Alice and Bob were exchanged in the demonstration of daylight *QKD*, written in parentheses.

Alice Alice´s analyzer is composed of a bulk 50:50 beam splitter for the random basis choice, zero-order half-wave plates and polarizing beam splitters for the polarization selection, see Figure 6.2. Additionally, a set of three wave plates (quarter-, half-, quarter-waveplate) is placed to compensate for setup-induced polarization changes [154]. The correct angles of the waveplates are set by optimizing the Bell parameter in a laboratory measurement set.

Bob Bob´s analzyer is composited of an in-fiber 50:50 beam splitter, where every output port is connected to an in-fiber polarizing beam splitter. The connecting fibers are passed through bat-ear polarization controllers for fibers. The bat-ear polarization controllers are set to keep the same polarization reference frame for Alice and Bob.

A sketch of the analyzing bases is shown in Figure 6.2.

6.3.1 Fiber-based communication channel

The main drawback for fiber-based *QKD* systems are the losses introduced due to absorption in the fiber. This limits the transmission length, by scaling exponentially for the raw key rate. Wavelength dispersion, on the contrary, exhibits less impact on the transmission length. But, when working with polarization encoded *qubits*, the fiber-induced polarization effects have to be accounted for

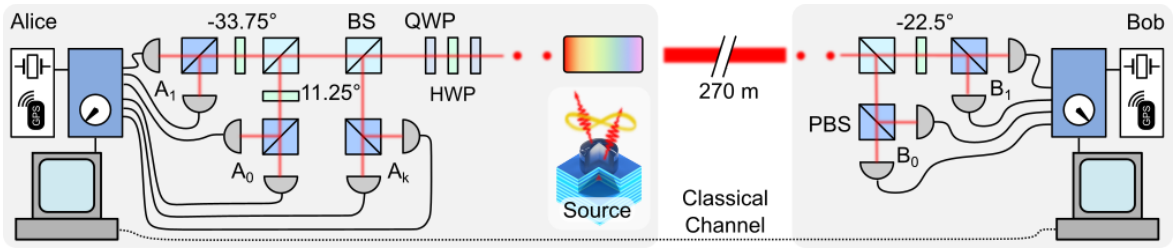

Figure 6.2. Sketch of Alice and Bob´s analyzing setup. In the implemented protocol Alice analyzes the bases $\{A_k, A_0, A_1\} = \{H/V, -22.5°/67.5°, -67.5°/22.5°\}$, whereas Bob analyzes the bases $\{B_0, B_1\} = \{H/V, -45°/45°\}$. Both systems are placed on the same frame of reference by a set of two quarter-wave plates (QWP) and a half-wave plate (HWP). The signals collected by the *APDs* are directly recorded by independent time-to-digital converters, which are synchronized by GPS-disciplined oscillators.

[4]. The fiber-induced unitary evolution of the polarization and also polarization changes due to non-perfect optics is compensated with a set of wave-plates or bat-ear polarization controllers for fibers, to keep the same frame of reference for all analyzer parts. This is an important preparation step to ensure measuring the correct polarization bases and consequently, generating a correct key as well as estimating the error correctly.

6.3.2 Free-space communication channel

Free-space systems have the advantage of low losses over distance [88], compared to fiber-based systems. However, the free-space environment brings along new challenges such as atmospheric absorption, turbulence, bright background, beam wander and weather conditions [171]. Sunlight, for example, increases the background noise, especially in the infrared, and temperature changes affect the stability of the system, evident for the coupling into the single-mode fiber. These effects contribute significantly to optical instabilities and noise. For our implementation the air-distance is roughly 270 m, and we can ensure non-stop operation of the communication by adding spatial and wavelength filters, and active feedback systems, in a wide range of weather conditions.

Absorption and scattering losses in the atmosphere are unavoidable. Signal stability due to beam wander, on the contrary, can be improved in multiple ways. The first thing is to pick the optimal choice of the beam waist. The goal is to minimize fluctuations and maximize collimation, with the challenge to achieve the best trade-off. A small beam waist decreases random oscillations within the beam waist, but it reduces the Rayleigh collimation range.
We decided to expand the beam to a diameter of 22 mm ($1/e^2$ intensity level). This size maintains collimation of the ∼785 nm signal-wavelength for almost 2 km, which is more than enough for our air travel distance of 270 m. The beam wander for this beam diameter is still small with an estimated maximum shift inside of 0.5 cm for a strong turbulence regime.

At the receiver side the signal is sent through a clear aperture, with a similar dimension of the first collecting optical elements of 4 inches. This reduces the noise from the diffused light. Then the signal beam is reduced and passes through a spectral filter with a bandwidth of 3 nm to filter out wavelengths clearly different from the quantum signal. Note, narrower filters are compatible

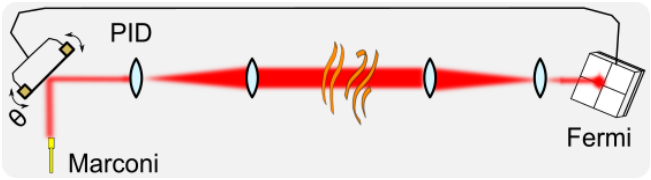

Figure 6.3. Sketch of the slow-drift stabilization system. Two tip-tilt mirrors (PM) compensate for slow temperature drifts of the free-space optics link. The angles of the mirror are determined by the offset of the reference laser to the center position of the camera.

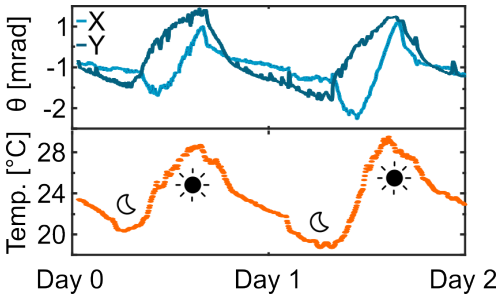

Figure 6.4. Temperature changes during day and night operation lead to a slow drift in the free-space optics. The tip-tilt mirrors compensate every 10 s for the drift enabling non-stop key distribution. Adapted from Ref. [172]

with a signal from a *QD*.

Slow-drift stabilization system: In the course of the first experiment we noticed slow drifts over the acquisition channel. For this reason we added for the second experiment, for the continuous 3-day operation, an active feedback pointing system consisting of a piezoelectric mirror connected to a 4-quadrant detector, which is placed at the receiver side, see Figure 6.3. A laser beacon, which is coupled into the common transmission path via a dichroic mirror on the sender side, is centered onto the 4-quadrant detector, by splitting the laser from the *QD* signal via a dichroic mirror. The proportional-integral-derivative controller is setup to keep the pointing laser always in the center of the camera. One feedback loop is chosen to be 10 s long, to average over fast beam wandering due to atmospheric turbulence. We now look at the angular motion of the mirror in tip-tilt direction and compare it with the outdoor temperature during a two-day test period. Figure 6.4 shows that the angular mirror motion and the outdoor temperature are correlated. So the pointing direction depends on the outside temperature, which suggests attributions due to thermal effects on the optical elements of the free-space system. During the test, the beam always falls within the 4-quadrant detection, as shown by the reading histogram of the camera, see Figure 6.5. The offset from the zero position of the detector readings is most likely due to wind-up, which is compensated for by the receiver stabilization system, which is implemented for the stabilization of fast fluctuations.

Fast-fluctuation stabilization system: Additionally to slow thermal drifts in real-world applications, the free-space *QKD* system also needs to compensate for mechanical vibrations and atmospheric turbulence. This is done by a fast-steering stabilization system. This stabilization

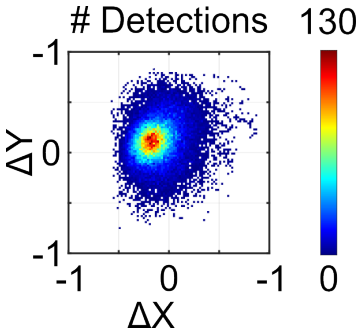

Figure 6.5. Histogram of the spot position on the stabilization camera. The values of displacement are relative to the size of the sensor. The tip-tilt mirrors keep the beam spot inside of the camera chip. Adapted from Ref. [172]

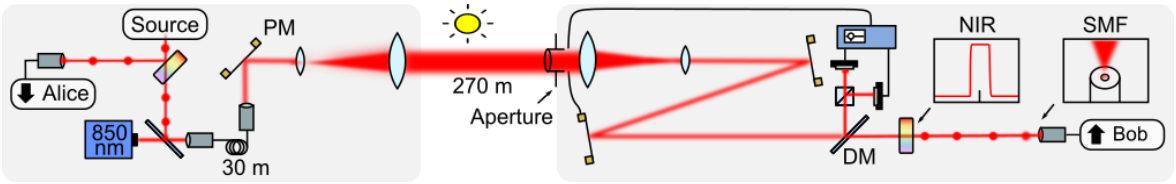

Figure 6.6. Sketch of the fast stabilization system. Two fast-steering mirrors at the receiver with a closed-loop frequency of 200 Hz compensate for atmospheric turbulence. The closed-loop feedback system keeps the 850 nm reference laser at the center position of two position-sensitive detectors.

system was implemented in both experiments. The implementation requires a laser to create an active feedback loop. We utilize the same laser as the one for the slow-drift compensation. Both the *QD* signal and the control laser at 850 nm are coupled in the same fiber at the sender side, to ensure that both are traveling the exact same path and ensure the same fluctuations while traveling through the overall channel. The 850 nm wavelength is chosen to be close to the signal wavelength of 785 nm to ensure a similar propagation through air as well as similar wavelength-dependent aberrations. On the contrary, we would like to separate the control laser from the signal, which is easy using a dichroic mirror. During operation we try to minimize the power of the control laser to lower the background introduced in the signal channel. Figure 6.6 shows the sender/receiver platform with the fast stabilization system.

The beam, that is directed to the receiver, is sent onto a 200 Hz closed-loop tip-tilt stabilization system on the receiver side. This active beam stabilization system (MRC Systems GmbH) consisting of fast-steering mirrors and position-sensitive detectors that compensate for most of the instabilities introduced by air turbulence. The stabilization process is tested using a 785 nm laser. Since the test laser signal at 785 nm and the stabilization laser at 850 nm are exiting the same fiber coupler at the sender side, it experiences the same perturbation as the signal. On the receiver side the 850 nm laser is used for the closed-loop control, whereas the test laser is coupled into a single-mode fiber. The coupling power is measured for the two scenarios, with the stabilization system on and off. The differences of the coupled power with and without the stabilization system is shown in Figure 6.7. The stabilization laser power is chosen to be roughly 100 μW, which guarantees good performances of the MRC system. This approach leads to an average single-mode fiber coupling

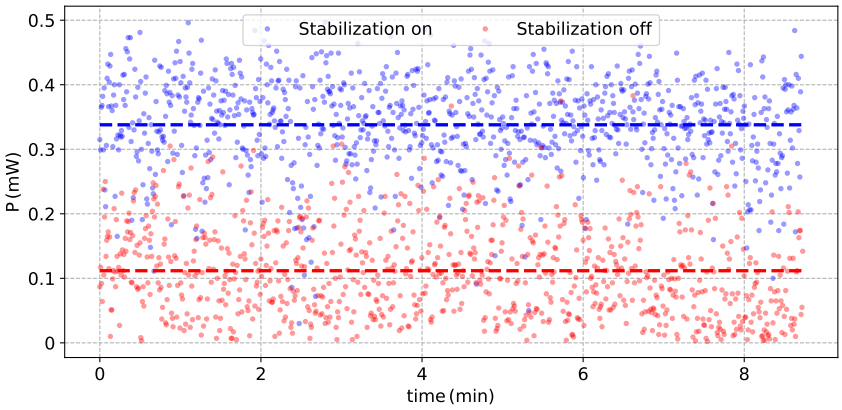

Figure 6.7. Test of the fast stabilization system. The coupled laser power of the test laser at 785 nm vs. the test period. The red dots correspond to the scenario where the MRC-laser beam stabilization system is off, whereas the blue dots are measured when the system is on. The dashed lines are the corresponding coupled mean values for the two configurations. Without stabilization the coupled laser power is 70 % less. Each measurement point corresponds to an acquisition of 10 s. From Supplementary of Ref. [23]

efficiency of 40 - 50 %. This result proves that the fast stabilization system lets us compensate for air turbulence to continuously couple the signal in a single-mode fiber. However, the coupling efficiency fluctuates in time and could be further increased. We expect the efficiency to improve when additionally adding an adaptive optics element, such as a deformable mirror. The deformable mirror could compensate for aberration modes beyond tip-tilt, which is introduced from the optics and in particular air turbulence.

The overall efficiency of the free-space link is 10 %. This includes optical losses on the sender and receiver platforms, attenuation in the free-space channel (around 10 % at this wavelength for a 270 m distance), and single-mode fiber coupling efficiency.

6.4 Data acquisition and post processing

During the experiment we register the timestamps of the photon arrivals at all the single-photon detectors with two time-to-digital converters with a timing resolution of 81 ps. In a next step two-fold coincidences for different channels, for example the simultaneous arrival of a photon at the key channel of Alice and Bob, are extracted. In order to generate these two-fold coincidences multiple processing steps are necessary because both parties, sender and receiver, have their own independent time-to-digital converter device and therefore a common time reference between the two devices needs to be established. To solve this problem a synchronization procedure between the two individual time-to-digital converters is implemented.

6.4.1 Synchronization

The two time-to-digital converters are synchronized via an external clock signal. This external clock signal is produced by a GPS-driven oscillator, which is connected to one of each time-to-digital con-

verter on Alice and Bob's side. To coarsely synchronize the two different GPS-oscillators, they are fed every second a GPS signal. This is needed to partially correct for device-dependent drifts inside the oscillator. Then the oscillator outputs a 10 kHz TTL signal, which is used for generating a common clock to perform a coarse timestamp correction between the sender and receiver time-to-digital converter. Using this external clock, a synchronization of the individual channels in the range of 10-20 ns is achieved.
To fine-tune the synchronization we look directly at coincidences between different channels. We can take advantage of the fact that the protocol publicly discloses bases to estimate the Bell parameter. Hence, we can choose a pair of those disclosed bases, which are cross-polarized. Knowing that our source does not create coincidences in these bases we expect a clear minimum in the coincidences when we look at simultaneously emitted photons in these two bases. We choose channel A_1^1 and B_1^0 and compute the histogram for relative time delays within 40 ns, which is around the channel delay from the coarse synchronization. The time delay between the channels given from the histograms is extracted and additionally applied to the time delay of the coarse synchronization step.

6.4.2 Data acquisition

Given the exact time delays we can record coincidences with a time window of ± 0.8 ns. The time window is chosen so to exclude as many dark counts as possible without significantly cutting the QD signal.

We collect the timestamps for the different channels for an exposure time of 1.2 s. The timestamps with the information on the corresponding measurement basis is compressed and shared between sender and receiver. Note, during this step no information on the measurement outcome for the key channels is exchanged. After data exchange, a new acquisition setting is started, and we again collect timestamps for the coincidence channels for 1.2 s. We point out that this method of sequentially collecting and exchanging data exhibits room for improvements. By parallelizing the data acquisition and data exchange, the redundant stop during data exchange is removed. This would enhance the overall efficiency of the key exchange.

6.4.3 Figures of merit and secure key extraction

Raw key rate and key sifting: From the exchanged timestamps, the raw key can be extracted by looking at the coincidences of the key channels. However, due to different losses in the channels discrepancies between the two arrays of key strings (detected timestamps on the key channel of Alice and Bob) exist. These have to be made the same size in order to estimate the correct figures of merits in the later step.
To do so, the bit string size between the sender and receiver is adjusted, by checking if the timestamps for the different key elements match. For example, if there is a missing key value in one of the two channels, the other key value related to this timestamp is deleted. After this process we refer to the bit string of the key channel as sifted keys. Since we matched the timestamps, both sifted keys should have the same length. However, the sifted key might still be erroneous due to

imperfections of the source, or measurement equipment, and a potential eavesdropper might have tampered with the communication to gain some information on the raw key.

Secret key extraction: In order to make the key fully secret, two steps, called error correction and privacy amplification, are carried out. This is necessary to determine if the key is below the error threshold of the protocol, remove the errors in the key and eliminate any information a potential eavesdropper might have.

The first step is to correct for errors in the raw key, which an eavesdropper or measurement imperfections introduced in the raw key, and are not explicitly corrected for in the key sifting process. But before conducting this step, the protocol checks if the collected parameters are correct. For this we check the Bell parameter for each measurement set of 5x1.2 s acquisitions using Eq. (6.1). If the Bell parameter for each measurement set is below the classical Bell limit this measurement set is discarded, since security cannot be guaranteed. In case it is above, the measurement set is kept and processed further. From the kept measurement sets we disclose 30 % of the key on the public channel. With these shared key results we test for the error in the sifted key, determining the *QBER* using Eq. (6.3). The error is needed to successfully perform the error correction with the CASCADE algorithm [173]. The algorithm first splits the sifted key into blocks of bit strings. The block size is given by the *QBER* and set so that each block has on average one erroneous bit. After bundling the sifted key into these blocks we can start the error correction by comparing the blocks of the sifted key with *XOR* operations. If the parity of the sub-block of Alice and sub-block of Bob matches, there is no evidence of an erroneous bit in the sub-blocks, and the sub-blocks are not modified. In case the parity does not match, the block is split again and the parity within the new (smaller) sub-blocks is again compared. This is continued until the faulty bit is determined. When detected, the faulty bit is either flipped or discarded. This procedure is applied multiple times to successively reduce the errors, as double errors, might have gotten undetected during the first round. Note that minimizing the error goes hand in hand with minimizing the secure bit length. During the error correction procedure, Alice and Bob share information about the key, the parity of the block, on a public channel, accessible to an eavesdropper. Even though no information about the concrete value of a single bit is shared publicly, the eavesdropper gains information about the key during this process. The information leakage of this procedure can be estimated by the binary Shannon entropy

$$h(\epsilon) = -\epsilon \cdot log_2(\epsilon) - (1-\epsilon) \cdot log_2(1-\epsilon) \tag{6.4}$$

where ϵ is the *QBER*. This information leakages needs to be accounted for in the next step, privacy amplification.

The second step is a specific post processing on the error corrected key to make sure that any information that might have been leaked to a potential eavesdropper is eliminated. The information leakage is composed by the bits openly disclosed during error correction plus the information that an eavesdropper could have obtained assuming that all errors are results of her tampering. For this

a so-called hash function is applied [174]. This hash function is a non-reversible classical algorithm that maps an array of a given size in another array of smaller size. The latter is compressed by an amount given by the information leak an can be estimated using again the Shannon entropy from Eq. (6.4) with $\epsilon = Q + \frac{S}{2\sqrt{2}}$. The applied hash function in our case is a Trevisan extractor [175]. When the hash-function is applied on the error corrected key it is reduced to a secure key length.

The key resulting from the privacy amplification step is called the secure key. The secure key r_{sec} can be estimated from the sifted key rate r_{sift} by subtracting the discarded key due to error correction and privacy amplification. The extend of the key reduction for both steps is given by $h(Q)$ and $h(Q + \frac{S}{2\sqrt{2}})$ from before. Hence, we can write for the secure key rate:

$$r_{sec} = r_{sift}(1 - f_{EC}h(Q) - h(Q + \frac{S}{2\sqrt{2}})) \tag{6.5}$$

where f_{EC} is the efficiency of the error correction and is for the CASCADE algorithm theoretically around 1.2 [176]. This extracted secure key can now be applied to the message that we want to send secretly. We take the message, convert it to the binary system and perform a simple XOR operation to encrypt the message. After this encryption step, the message can be sent via a public channel, with the advantage that for any eavesdropper this message resembles to be random. In order to ensure that no information can be extracted the *OTP* procedure is applied. This considers that the secure key is as long as the message to be encrypted and the secure key is only applied once.

6.5 First field quantum key distribution using entangled photons from a quantum dot

As previously discussed, optical communication links rely on fiber transmission in the C-Band (1530-1565 nm) or on free-space transmission in one of the atmospheric windows, such as 775-785 nm. GaAs *QDs* provide a sub-Poissonian light source suitable for both wavelength regimes. With a wavelength range of 770-790 nm depending on the growth parameter, GaAs *QDs* can either directly or indirectly—proovia frequency conversion—provide *qubits* for both applications. GaAs *QDs* under resonant-two photon excitation are close to on-demand entangled photon emitters, which offers a solution to number splitting [177] or beam splitting attacks [178], which take advantage of a non-perfect single-photon distribution of the emitter. At the same time the antibunched nature of the light emitted by the *QD* improves the communication security in the presence of losses [168], allowing longer communication channels.

Up to our experiment [23] one pioneering demonstration of entanglement-based protocol has been realized using an entangled light-emitting diode [179]. With a BBM92 protocol a sifted bit rate of 0.17 bps and a *QBER* of 9.8 % was achieved. It demonstrated the proof of concept to use entangled photons from *QDs* for *QKD*, but the sifted bit rate is rather low and the *QBER* is close to the 11 % threshold of the most common error correction algorithms [3]. Hence, going towards a

free-space implementation would be rather challenging.

In our first *QKD* experiment we demonstrate the proof of principle that entanglement based *QKD* is also applicable for as-grown *QDs*. We performed *QKD* with the adapted Ekert91 protocol proposed by Acín et al. across the fiber and free-space channels previously described in Section 6.1 and Section 6.3. I want to point out that Schimpf et al. [149] simultaneously performed a similar experiment using the same entangled photon source, GaAs/AlGaAs *QDs*, using a different protocol, the BBM92, and demonstrating a key exchange in a 350 m fiber system.

For this measurement set we placed Bob on the side of the entangled photon source and Alice after the free-space channel. Also for this measurement set only the fast-steering stabilization system was implemented. The security of the transmitted key is checked by testing the Bell parameter during data acquisition. With the data acquisition process as explained in Section 6.4 we exchange a key for 4 hours. Using this approach we achieved a sifted key rate of 60 bps resulting in a total key string of 34.589 kB shared via the free-space communication link. The sifted key rate is plotted in Figure 6.8. It is noticeable that the key rate is fluctuating over time, which we account to multiple factors. First, changing atmospheric turbulence influences the coupling to the single-mode fiber on the receiver side. Different turbulences introduce different aberrations, rendering the beam non-Gaussian and hence influencing the coupling efficiency to the single-mode fiber on the receiver side. Using an aberration correction module could potentially restore the wavefront and keep the coupling efficiency constant. Additionally, we noticed a slow drift lowering the key rate over the whole experiment. This indicates a potential misalignment of the optics system indicating that the fast-steering stabilization system is not able to compensate for all free-space link challenges.
We simultaneously record the Bell parameter for the whole key exchange. As visible in Figure 6.9, the Bell parameter is always above the classical limit of 2. The average Bell parameter during the whole 4 hours of acquisition is S_S =2.37(10). The error bars for the Bell parameter are calculated from a Gaussian error propagation assuming a Poisson distribution for the coincidence counts. It is noticeable that the Bell parameter is not as high as the quantum limit of $2\sqrt{2}$. One reason for this is the imperfection in the entangled photon source (fidelity of 0.958). One other challenge, leading to a lower Bell parameter, is the accuracy of polarization compensation between the two analyzing setups. Optical elements alter the polarization state of a photon due to their imperfections. In order to correlate the correct bases in the measurement, we need to bring the two analyzing setups (Alice and Bob) to the same frame of reference. Hence, we need to align the two polarization analyzing setups to measure the same polarization. Currently, this is achieved by sending the signal in two specific sets of commonly agreed polarizations, namely H/V and D/A in an initial link start-up procedure before taking the measurement set. Performing a full tomography of the free-space link might give more insights into the polarization effects on the free-space link. Also, finding a way to continuously account for polarization changes would potentially improve the Bell parameter, bringing it closer to the quantum limit.
The *QBER* is the last parameter extracted from the measurement set. Figure 6.10 shows that the *QBER* is well below the error correction protocol limit of 11 % during the whole measurement pe-

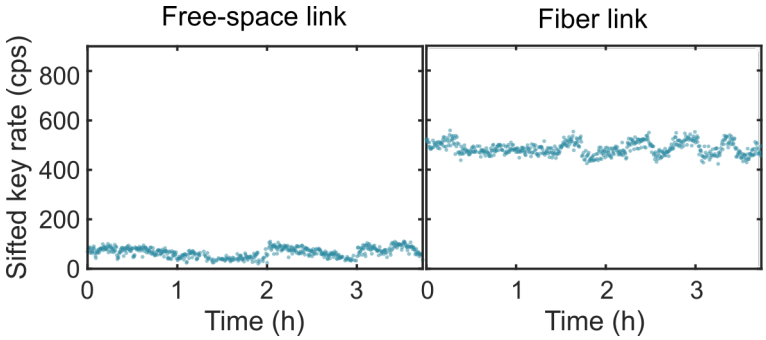

Figure 6.8. Sifted key rate shared through the free-space optical link and fiber link over four hours. The average sifted key rate throughout the exchange is 60 bps for the free-space link (486 bps for the fiber link). Every data point corresponds to five acquisitions of 1.2 s. Adapted from Ref. [23]

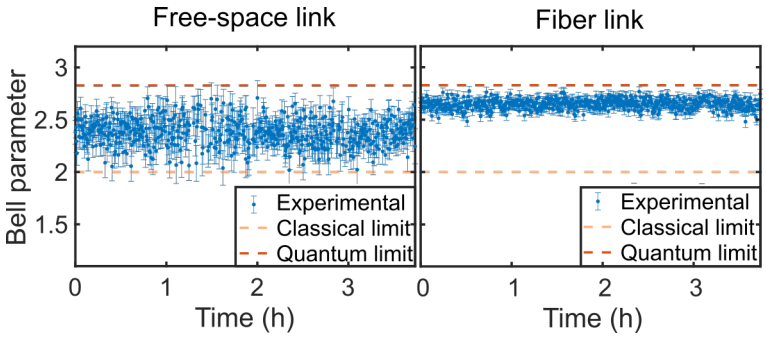

Figure 6.9. The Bell parameter achieved in the free-space optical link and fiber link over four hours. During key exchange the Bell parameter is always above the classical limit with an average over the acquisition period of 2.37(10) for the free-space link (2.647(2) for the fiber link). Every data point corresponds to five acquisitions of 1.2 s. The error bars are calculated by a Gaussian error propagation assuming a Poissonian distribution for the coincidence counts. Adapted from Ref. [23]

riod. The rise at the end of the experiment is due to increased background light from the approach of dawn. The average *QBER* is Q_S =4.0(2) %, which we attribute to the non-perfect entanglement fidelity of the source, background light, and inaccuracies in the synchronization.

We also perform a key exchange using the same protocol in a fiber-based link. This offers a comparison to the free-space link, by having reduced technical challenges. The main technical hurdle in the fiber-based link are polarization effects introduced due to the optics and fibers. Both effects, though, are static and well studied.
With a *QD* with similar figures of merits compared to the free-space demonstration, using the same protocol and the same measurement procedure, we achieve an average Bell parameter of $S_F = 2.647(2)$, a *QBER* of $Q_F = 3.37(2)$ % and a sifted key rate of 486 bps (see Figures 6.8, 6.9, 6.10). The total shared key is 217.76 kB. It is noticeable that for the measurement set of the fiber-based link better results are achieved for all figures of merits. This raises questions on how to optimize the free-space link. The slow drift in the free-space link, which is not present in the fiber link, would suggest the implementation of an additional stabilization systems for slow drifts. We implemented this slow-drift stabilization system for the second measurement set presented in the next section. Another point that potentially improves the figures of merits of the free-space

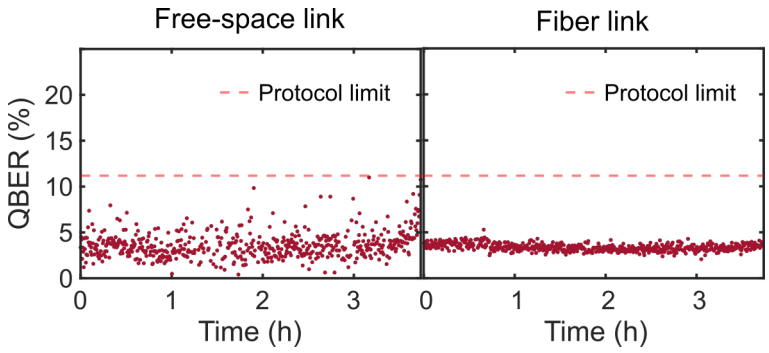

Figure 6.10. The *QBER* over four hour key exchange in the free-space optical link and fiber link. The average *QBER* amounts to 4.0(2) for the free-space link (3.37(2) for the fiber link) and stays well below the protocol threshold of 11 % during the whole measurement period. The rise at the end of the experiment in the free-space link is due to increased background light from the approach of dawn. Adapted from Ref. [23]

link is continuously compensating for aberrations using an active feedback system consisting of a wavefront sensor and a deformable mirror/lens. The last point, that would improve both, the fiber-based link and the free-space link, is a parallelization of the data acquisition and data exchange. This would increase the total transmitted key in both measurement conditions.

6.6 Daylight quantum key distribution using entangled photons from a quantum dot

Most free-space quantum communication experiments have been demonstrated under favorable conditions. The absence of sunlight, which is a massive source of background in infrared radiation, and good weather conditions as well as post-selected short periods of total key-exchange times avoid drops in performance related to high background noise and misalignment of the optical system. But, to ensure real-life quantum communication based on free-space channels, these challenges need to be addressed.
Many experiments have been conducted tackling these challenges with active stabilization systems [180], and adapting the optics system with spatial, temporal and wavelength filters [181–183]. However, this was proven mainly using prepare and measure protocols [181, 182]. Up to now only one experiment accepted the challenge for entanglement-based *QKD* using a *SPDC* source with bandwidth filtering [183].

We, for the first time, take on the task and demonstrate 3 days continuous key distribution using a *QD* as entangled-photon source. During the performance of the experiment the key exchange was exposed to different weather conditions as sun and even mild rain. We demonstrate that this system is alignment-free and stable to show minimal variability in performances during the different atmospheric conditions.

To perform this experiment, we place Alice on the side of the entangled photon source and Bob after the free-space channel. Compared to the first *QKD* experiment discussed in the previous

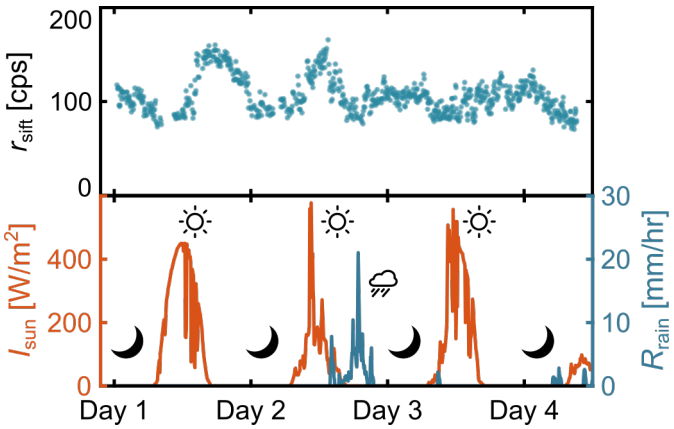

Figure 6.11. The sifted key rate over three and a half days of continuous operation. Each data point is an average over 100 acquisitions of 1.2 s. The weather data for the same measurement period is provided by a nearby meteorological station (CNR Sede Centrale). Adapted from Ref. [172]

chapter we improved our free-space optical link. First, we added the slow-drift stabilization system to compensate for misalignment due to temperature. This is detrimental to keep the alignment in the free-space link for the temperature changes during night and day. We also shielded the entrance to the receiver system with an aperture, close to the optics size (4 inch) and added a mild spectral filter to eliminate direct sun light.

With these adaptions to the setup, we are able to exchange 106 bps sifted key rate averaged over all the different weather scenarios. When comparing the sifted key rate with the irradiation of the sun, see Figure 6.11, we can see that there is no visible correlation between these two. In fact, the sifted key rate is fluctuating due to oscillations in the coupling efficiency at the receiver. We attribute the oscillating coupling efficiency to air turbulence, which an additional adaptive optics kit could stabilize and potentially improve the free-space link [184]. The averaged Bell parameter over the whole measurement period results to 2.409(2). Figure 6.12 shows that the Bell parameter is always significantly above the classical limit during the whole measurement set. The error bars are calculated by a Gaussian error propagation assuming a Poissonian distribution for the coincidence counts. Comparing the Bell parameter with the weather data (irradiation of the sun and rain rate) collected by a weather station close to the link location, we can see that the rain rate has no visible effects on the *QKD* parameters. The *QBER* averaged over the whole measurement period is 7.16(2) % and is rather stable during the whole experiment. The fact that the figures of merit remain rather stable and well within the thresholds of the *QKD* protocol, reassures us on the stability of the free-space link. But, having a close look at Figure 6.12 we see that the Bell parameter and the *QBER* slightly decrease/increase with higher level of sunlight. Further investigations showed that the change in the parameters is consistent with the level of background detection events due to incomplete filtering of the external light. We could minimize this problem by using narrower spectral filters, which would be compatible with our source. Rain, on the other hand, does not show a significant impact on the Bell parameter and *QBER*. At least this is the case for the levels of rainfall with peaks of 20 mm/hr during the experiment.

Overall the experimental results demonstrate that the aperture, the spectral filtering and the

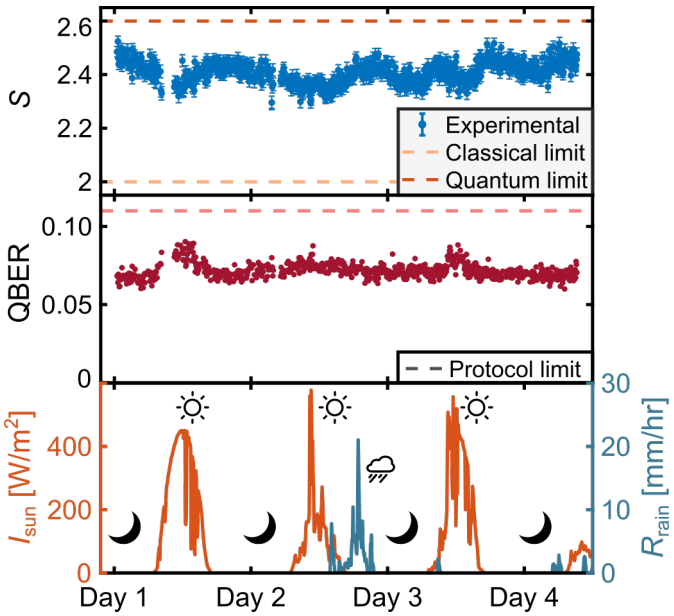

Figure 6.12. The Bell parameter and the *QBER* over three and a half days of continuous operation. Each data point is an average over 100 acquisitions of 1.2 s. The weather data for the same measurement period is provided by a nearby metrological station (CNR Sede Centrale). The error bars in the Bell parameter are calculated by a Gaussian error propagation assuming a Poissonian distribution for the coincidence counts. Both, the Bell parameter and the *QBER* slightly vary with the sun level. Adapted from Ref. [172]

slow- and fast-stabilization system allowed us to exchange a secret key over the whole duration of 3 days with an average shared secure key rate of 12 bps.

6.7 Conclusion

We could demonstrate for the first time *QKD* over a 270 m free-space channel with a *QD* as source of entangled photons. This first proof of principle using *QDs* is an important milestone for future applications of *QDs* and for entanglement-based *QKD*-systems [23]. The first demonstration made us confident to go one step further towards real-life applications, the continuous key exchange over multiple days. By adjusting the free-space link we achieved a continuous key exchange for a total of 82 hours, withstanding daytime and even moderate rain. Both applications are crucial requirements for the use of such technology in real-life applications.

The achieved efficiencies and key rates of both experiments are undoubtedly moderate and leave room for improvements. First, the setup efficiency (ca. 0.2) and free-space link transmission (ca. 0.1) should be increased before follow-up experiments. But also the characteristics of the *QD*-sources should be improved. The brightness of the *QDs*, for example, is mainly limited due to the extraction efficiency of the sample structure (ca. 0.1) and the blinking (ca. 0.3). This leads to an estimate of extracted photon pairs per excitation cycle to $0.1^2 \cdot 0.3 = 0.003$. This can be increased, when switching to a different sample structure based on advanced cavities, as the

second-order Bragg grating. They achieve pair-extraction efficiencies of 0.65(4) and entanglement values of 0.88(2) [29]. This source could provide 200x more extracted photon pairs with respect to the used sample. Additionally, these cavities have the advantage that they show a mild Purcell enhancement. The Purcell effect would shorten the lifetimes of the transition and consequently, might allow for a faster pumping rate. Hence, implanting GaAs/AlGaAs *QDs* inside second-order Bragg gratings, hold great promise for high secure key rates. These might even have the potential to supersede current probabilistic sources [185]. These predictions seem positive that *QDs* potentially be implemented for future out-of-the-lab secure communication systems.
One might still argue, though, that for real-life applications the operation temperature of *QDs* is quite challenging, especially considering applications where the sources are mounted on a satellite node. Building cooling equipment for an operation temperature below 10 K, as is the case in our experiments, is indeed a tremendous expense. But cryo-coolers for temperatures up to 30 K become less bulky [186]. For this reason, operating GaAs/AlGaAs *QDs* at higher temperatures is an interesting goal for real-life applications. In theory, GaAs/AlGaAs *QDs* can be operated at higher temperatures, however, the higher the temperature, the more noise is added to the environment, for example above 10 K phonon side-bands start to be populated. Consequently, the higher the temperature, the lower the entanglement of the emitted photons. Recent results create hope for the usage of *QDs* at higher temperatures in *QKD* applications. Schimpf et al. [147] demonstrated *QKD* using the BBM92 (entanglement-based) protocol with a GaAs *QD* at 20 K. Additionally, they managed to stabilize charges with a p-i-n diode, to fully eliminate blinking at 20 K. The extraction efficiency, on the contrary, was not improved on that device. Hence, the achieved raw key rate exchange amounts to 54.8 bps with a resulting average secure key rate of 14.2 bps over their 350 m fiber system. They also pointed out that the same p-i-n diode can be used to tune the emission wavelength within 0.2 nm. All the achievements, no blinking, low noise at 20 K and wavelength tuning, bundled in one source, is a major step towards the goal of real-life applications of *QKD*, but also quantum networks. The latter especially benefit from precise wavelength matching of multiple emitters and high transmission rates given by no blinking. Further studies on geometries and different material choice for the *QD* could help to raise this temperature threshold to 30 K. But also ultra-efficient superconducting nanowire detectors or quantum memories are currently relying on cryo-cooling.

Overall, these experiments demonstrate that *QDs* are applicable for *QKD*, but there is still room for improvements. The source should be upgraded to make the most of the fast transitions and possible repetition rates to generate entangled photon pairs. Also technological challenges, as operation at higher temperatures and scalability, need to be further addressed. One of the next big steps would be demonstrating *QD* advantage. This means, demonstrating that the achievable key rates using *QD* as entangled-photon source are superior to other entanglement-based systems, as *SPDC*. Combining the new cavity design, which increases the extraction efficiency and simultaneously having low Purcell enhancement, with a charge tunable device to reduce blinking as well as allow the emission lines to be fine-tuned, might suffice to show the advantage of non-classical light emitters, as *QDs*, over the probabilistic entangled-photon technology, *SPDC*. Theoretical forecasts

predict that the goal is achievable [185]. However, fabricating a device that fulfills all the requirements simultaneously is a tremendous challenge. But I am optimistic that one of the many research groups that are currently working on improving the source will succeed and higher secure key rates using *QDs* as entangled photon sources are to come.

Chapter 7

Discussion and outlook

7.1 Discussion

In the course of this thesis I could work on multiple projects all related to increase the understanding of GaAs/AlGaAs *QDs* as entangled photon sources for potential quantum networks.

The first part of this thesis discussed entanglement degrading effects in GaAs *QDs*, which have not been fully addressed in the literature before. Multiphoton emission, for example, is a tremendous limitation for entangled photon sources, limiting their applicability in *QKD* [22, 23] and scalability for multiple photon experiments [20]. During the work on this thesis I could demonstrate that the entanglement of GaAs *QDs* under resonant *TPE*, the excitation scheme typically applied to generate almost on-demand entangled photons [25], does not suffer from multiphoton contributions. This was shown experimentally and underlined by a simple theoretical model [95]. The result that entanglement is unchanged regardless of the driving strength of these *QDs* emphasizes the single photon pair capability of the source. Additionally, the results are a positive remark for real-life applications since drifts and misalignment of the optical excitation might vary the driving strength. However, the measurements show that this does not impair the entanglement and consequently, security is preserved regardless of possible fluctuations in brightness of the source.
The second entanglement degradation effect studied in this thesis has been discussed theoretically only very recently. Seidelmann et al. point out that the short pulses of the excitation laser for resonant *TPE* excitation induce an optical Stark shift which splits the energy levels of the *QD* and thus lowers entanglement. In this thesis the degradation due to the excitation laser pulse has been verified for the first time in an experiment. It validates the degradation of entanglement by the excitation laser and also confirms that this effect follows the theoretical prediction of a splitting induced by the optical Stark effect. However, the measurements taken in the course of this thesis are only preliminary. To understand the full extend of this effect a more detailed investigation is necessary. For example, theoretical predictions would suggest a dependence of the splitting on the polarization of the excitation laser. During the measurements also power dependencies were observed. Both need to be examined to fully understand the extend of the laser-induced Stark effect. Regardless, the results demonstrate that this effect has to be taken into account when measuring entanglement under *TPE*, more precisely, when extracting the entanglement value for

photon pairs emitted by a GaAs *QD*. The results potentially initiate research for changes in the current excitation method or even for alternative approaches.

The second part of my thesis involved two applications of the highly entangled photons emitted by GaAs *QDs*. The high entanglement values achieved with these *QDs* allowed the demonstration of entanglement-based *QKD*, which allows in theory full secure communication. In the course of this thesis a quantum key is shared via two communication scenarios, fiber and free-space, using an asymmetric Ekert91 protocol [23]. The first experiment validates the proof of concept for both communication infrastructures. A follow up study, the second experiment, presents the continuous sharing of a quantum key over 3 days [172]. This experiment included new challenges, as the exposure to sunlight and mild rain. The achieved figures of merit are undoubtedly moderate. But these numbers are expected to be improved by using better suited *QDs* (higher entanglement, brighter) and combining them with new cavity designs, as the second-order Bragg grating cavity. The next milestone is demonstrating that the achievable key rates using *QD* as the entangled-photon source are superior to other entanglement-based systems, as *SPDC*. Combining the new cavity design, which increases the extraction efficiency, with a charge tunable device, to reduce blinking as well as fine-tune the emission lines, might suffice to show a *QD* advantage. Theoretical calculations predict that the goal is achievable. However, fabricating a device that fulfills all the requirements simultaneously is a real challenge. But I am optimistic that one of the many research groups currently working on improving the source will succeed and higher secure key rates using *QDs* as entangled photon sources are to come. This proof might start a transition to *QDs* as the favored platform for secure communication.

With these two main topics, studying and applying GaAs *QDs* as entangled photon sources, I contributed to an improved understanding of the entanglement generation process and proved that as-grown GaAs *QDs* are already at a level for first applications in secure communication. I truly hope that the experiments conducted in this thesis are going to be a foundation for further research questions on related topics.

7.2 Towards quantum networks - Remote quantum teleportation

At last in this thesis I would like to propose an additional experiment that would allow GaAs/AlGaAs *QDs* to go beyond two-party communication and to be entangled photon sources for real-life quantum networks.

Quantum networks enable to share quantum information between different parties linked by quantum nodes. The nodes, due to the no-cloning theorem, cannot simply share information between them by copy-and-repeat [5]. Hence, linking quantum network nodes and transferring information between them at large distances requires the implementation of entanglement swapping [16] and quantum teleportation protocols [187].

The idea of quantum teleportation is already introduced in Section 2.3. In a nutshell, the teleportation dynamics is a Bell state measurement, which is performed on the photon we want to teleport (photon 1) and one photon of an entangled photon source (photon 2), and the detection of the state of the second photon from the entangled photon source (photon 3). When an arbitrary input state in the (H, V) basis is chosen, we demonstrated mathematically that the combined wavefunction of the three-photon experiment is Eq.(2.13). The four outputs of the four Bell states have equal probability. Most experimental approaches resort to detecting the $|\psi^-\rangle$ state to verify the teleportation operation. This state can easily be distinguished from the other emerging Bell states upon its explicit quantum interference behavior. As can be extracted from Eq. (2.18), the $|\psi^-\rangle$ state exclusively yields a single photon at each of the output ports of the interfering beam splitter and hence causes a click event on both photodetectors. These simultaneous clicks at the photodetectors are used to confirm that the Bell state measurement is successful. When this probing for the $|\psi^-\rangle$ state is successful and the sent input state of photon 1 is $(\alpha\,|1\rangle_1 + \beta\,|0\rangle_1)$, Eq. (2.13) provides us that the state of the second photon from the entangled photon pair (photon 3) is in state $(\alpha\,|1\rangle_3 - \beta\,|0\rangle_3)$. The transferred state on photon 3 can then be brought to the initial state $(\alpha\,|1\rangle_3 + \beta\,|0\rangle_3)$ by applying the σ_y Pauli matrix, see Eq. (2.15).

To verify the success of the teleportation protocol, the fidelity of the transferred state to the initial state, averaged over all the possible inputs, has to violate the classical limit of $\frac{2}{3}$ [188]. In order to demonstrate this, it is sufficient to calculate the average protocol fidelity over a set of so-called mutually unbiased states, i.e., {(H,V),(D,A),(R,L)}. Because when performing quantum teleportation with classically correlated photons, it is not possible to overcome the classical limit for the complete set. Hence, it uncovers the failure of the quantum teleportation operation [33].
We can estimate the teleportation fidelity from normalized detection probabilities (rectlinear (H,V), diagonal (D,A), and circular (R,L)) of the co- and cross-polarized threefold correlations. In detail, it implies correlating the photons from the *BSM* with the analysis of the transferred state, the state of photon 3. This can be explained looking at the conceptual idea of the experiment. For simplicity lets consider that we only analyze photons that correspond to a $|\psi^-\rangle$ measurement, which occurs in 25 % of the cases, and the polarization of photon 1 is D. If the detectors at the two output ports of the beam splitter for the *BSM* detect a photon at the same time, we account this event to have measured the $|\psi^-\rangle$ state. In that case we know from Eq. (2.13) that the polarization of photon 3 is D. Now we analyze the polarization of photon 3 by rotating the half-waveplate by 22.5°so that the polarization is rotated by $+45°$ and selecting D and A polarization with a polarizing beam splitter. To demonstrate that the teleportation was successful, only the detector at the D output of the polarizing beam splitter should register a detection once both the detectors from the *BSM* registered detections (detected the $|\psi^-\rangle$ state). The detector at the A output of the polarizing beam splitter, on the other hand, should not detect a photon. Hence, recording a three-fold coincidence between the two *BSM* detectors and the D detector together with the absence of a three-fold coincidence between the two *BSM* detectors and the A detector proofs that the polarization of photon 1 has been transferred onto photon 3. The fidelity of teleportation can

then be extracted by the three-fold coincidences for the corresponding analysis basis:

$$f_T^{diagonal} = \frac{g^{(3)}_{|A\rangle}(0)}{g^{(3)}_{|A\rangle}(0) + g^{(3)}_{|D\rangle}(0)} \tag{7.1}$$

The overall teleportation fidelity is then the average of the teleportation fidelities for the different polarization bases, which has to surpass the classical limit.

Following this strategy, quantum teleportation was demonstrated successfully on different platforms [33, 121, 189]. Quantum teleportation with a GaAs *QD* by letting interfere two photons from the same *QD* (just from different excitation cycles with a spacing of 2 ns) resulted in an average teleportation fidelity of 0.75(2) [33]. Similar teleportation fidelities were verified on multiple *QDs*. The two most important parameters for a successful teleportation is the *HOM* visibility of the two interfering photons and the initial entanglement fidelity to the expected $|\phi^+\rangle$ state from the entangled photon source. However, it has to be emphasized that the prior has a stronger impact on the success of the teleportation success. Note, the same entangled photon source, a GaAs *QD* exploiting the same approach of repetitively exciting the *QD* and performing a *BSM* on two consecutive photons led to the first demonstrations of entanglement swapping [35, 75], the underlying procedure to link the nodes in quantum networks.

These experiments visualize that *QDs* have the potential to be the core of a quantum repeater node. However, all the discussed experiments so far were performed on the same *QD*, which simplifies the experimental demonstration in several ways. First, the setup complexity is heavily reduced. In the before mentioned experiments only one cryostat is needed to cool the source. Also the excitation laser is the same and only its repetition time is extended via matched delay lines. The only experimental difficulty is to match the delay line of the excitation laser with the delay for the two-photon interference in the *BSM*. Second, the achieved *HOM* visibility is most likely higher because the emitter is the same. The same emitter experiences the same environmental effects, which is even stronger when performing interference between two subsequently emitted photons, minimizing dephasing mechanisms. Consequently, these experiments completely neglect sample variations and different environmental effects, which are present in real-life applications. In a real-life quantum network, for example, we would like to have two separate quantum repeaters at different locations. Each quantum repeater has its own entangled photon source, which should perform quantum teleportation or entanglement swapping. Hence, the actual experiment we are interested in is remote quantum teleportation or remote entanglement swapping. This would exactly mirror the potential application of linking or transferring information between the nodes (at different locations) in a network.

Based on the existing literature, I propose the following experiment for remote quantum teleportation using GaAs *QDs*, sketched in Figure 7.1: One *QD* (QD2) is placed in a cryostat, preferably closed-loop, and excited with a Ti:Sapphire laser in phonon-assisted two-photon excitation. The *X* photon is spectrally filtered out and the *XX* photon is sent towards the interference setup. A

second *QD* (QD1) is placed in a different cryostat, preferably also closed-loop, and is operated as an entangled photon source. The entangled photon pair is generated via phonon-assisted two-photon excitation, using the same Ti:Sapphire laser. To do so, the Ti:Sapphire laser is coupled into a single-mode fiber and split using a fiber beam splitter, with two output modes. One output fiber is installed to excite QD2 and the second QD1. The broad wavelength acceptance window of phonon-assisted two-photon excitation and the power insensitivity of the excitation to prepare the biexciton state allows for simultaneous excitation of two remote *QDs*. Small differences in excitation powers for the two *QDs* can be regulated by gradual neutral density filters. The photons from QD2, in case the emission is polarized, are selected in a polarization state and then coupled into a common detection path with the entangled photon source (QD1). An adjustable delay line (Δt) allows to overlap the photon from QD1 with a photon from QD2 at the fiber beam splitter. The common path is aligned so that the photons of QD2 and QD1 travel the same optics path, but in parallel. This is important for a common linewidth filtering of the two *XX* photons via an etalon filter to increase the *HOM* visibility. Now the *X* and *XX* photons are spectrally selected using *VBGs* in reflection. The *X* photon from the entangled photon pair (QD1) is sent to an analyzing setup consisting of half- and quarter-waveplate (HWP, QWP) and a polarizing beam splitter (PBS). Both *XX* photons are sent through an etalon filter and then to the interference setup, where they are separated again. The *XX* photon from QD2—using a combination of linear polarizer, HWP and QWP—is now prepared in the polarization state as teleportation input. Then the two *XX* photons, one prepared in the polarization state as teleportation input (QD2) and the other from the entangled photon source (QD1), are sent into an in-fiber beam splitter for two-photon interference. Each output port has a polarizing beam splitter to allow for a 50 % efficiency *BSM*. We collect three-fold coincidences between the detectors where the analyzing detections (in the *X* path) are triggered by the detection of the correct basis in the *BSM* (in the *XX* path). These three-fold coincidences are collected for all the different analyzing bases on the *X* photon $\{(H,V),(D,A),(R,L)\}$ for the input states $\{H,D,R\}$. This assumes that the polarization bases are consistently aligned to each other in the different parts of the setup. The success of the teleportation operation is then determined calculating the averaged teleportation fidelity from the analyzing basis set. If it is above the classical limit of $\frac{2}{3}$, the demonstration of quantum teleportation was successful.

Why has the experiment not been performed so far? Conceptually the experiment seems very easy to conduct. One sends two photons, one from a single photon source, one from an entangled photon source onto a beam splitter, lets them interfere and measure three-fold coincidences between the *APDs*.
In order to get a successful teleportation two parameters need to be considered, the *HOM* visibility and the entanglement of the *QD*. First, we need a high *HOM* visibility. The visibility is, as discussed before, already intrinsically lowered due to the broadened linewidth of the *QD*. But this is even more challenging for remote emitters, because now we need two photon sources, two *QDs*, in different samples with matching wavelengths and with close to Fourier-limited linewidths. Additionally, one of the two *QDs* has to emit highly entangled photons.
Since the *QD* fabrication is random and each results in a slightly different emission wavelength, the

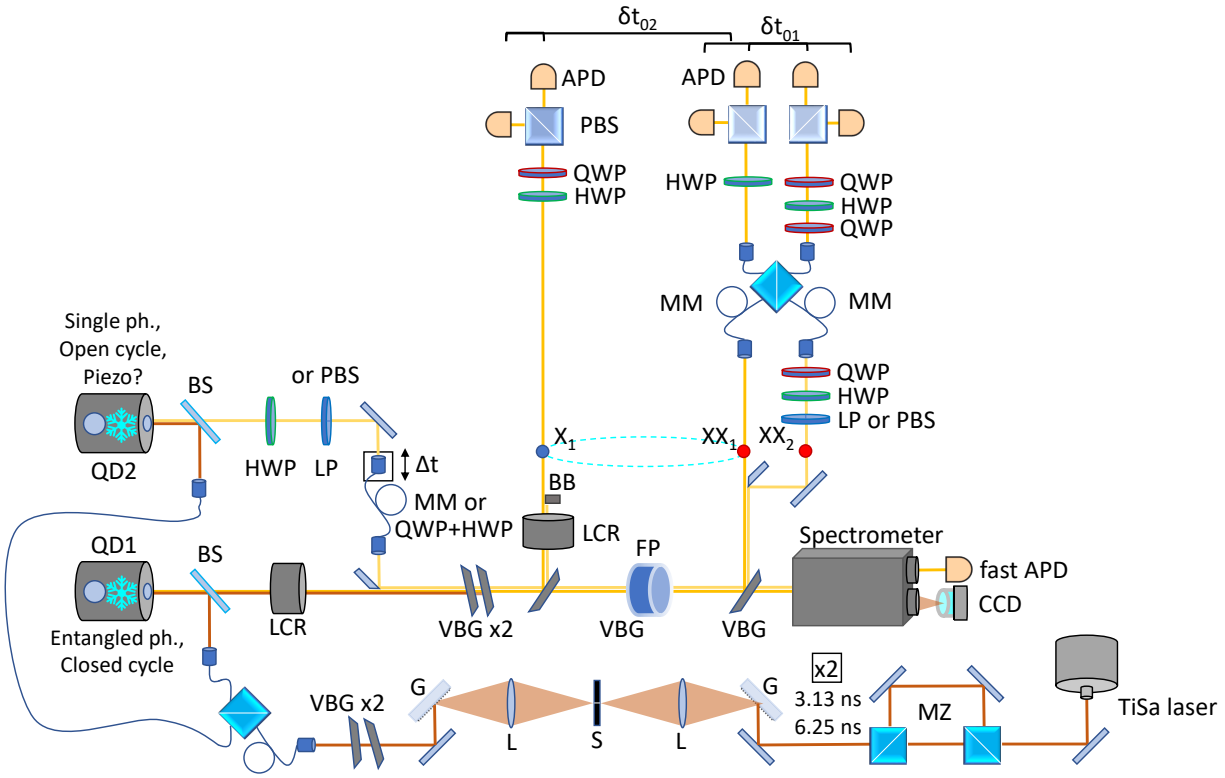

Figure 7.1. Proposed teleportation setup. The repetition rate of the excitation laser (Ti:Sapphire) is increased to 320 MHz by multiple delay lines. Afterwards the laser is split and sent to two individual cryostats, which contain a GaAs *QD* sample each. QD1 is used as an entangled photon source, QD2 as a single photon source. The emitted photons from QD2, in case polarized, are selected in a particular polarization using a half-waveplate (HWP) and a linear polarizer (LP) and coupled into a common detection path with QD1. An adjustable delay line (Δt) allows to overlap the photon from QD1 with a photon from QD2 at the fiber-beam splitter. The X and XX signal are spectrally selected using *VBGs* in reflection. The XX of QD1 and QD2 are sent into a *BSM*. The XX of QD2 is now prepared in the polarization state as input to be teleported, using a combination of linear polarizer, HWP and QWP. Note, the other waveplates on this path are only for polarization compensation due to polarization mismatches between the different optical paths. Then both XX are sent into the fiber-beam splitter for interference. The polarizing beam splitters (PBSs) at the output port of the beam splitter allow for a 50 % efficiency *BSM*. When one of the two Bell states is measured, also the X signal from QD1 belonging to the same cascade as the XX photon from the successful *BSM* is analyzed. The QWP and HWP in this detection path allow for the measurement in different bases, which is necessary to prove the success of the teleportation by surpassing the classical limit for the average teleportation fidelity.

two interfering photons would be distinguishable already in terms of wavelength. For this reason a strategy to tune the energy is needed. We can resort to piezo-electric tuning, electric or magnetic fields, which have the ability to fine-tune the emission energy. Regardless of the method, this increases the complexity of either the sample or the setup.
The wavelength, however, is not the only differing parameter between two *QDs*. Each *QD* is surrounded by a different environment (defects, interfering electrons) causing dephasing, which is individual for each *QD* and, consequently, lowers the interference visibility. To achieve an average teleportation fidelity of 75 %, which would allow us to overcome the boundary for error resistant *QKD* protocols with some error margin [190], we would need a visibility of around 25 % [34]. But, in order to use regular *QKD* protocols [3] we would need a higher visibility because, the higher the visibility the better the achieved average teleportation fidelity. Achieving a good remote interference visibility is one of the main challenges. First tests on remote *HOM* visibilities assured us that for the current state-of-the-art as-grown *QDs* spectral filtering will be crucial. Hence, we propose to use an etalon filter, which transmits only a certain bandwidth, reducing the linewidth before interference. Reducing the linewidth has been demonstrated to increase the average teleportation fidelity [34]. But the filter bandwidth has to be selected with great care. On the one hand, the narrower the bandwidth the higher the expected visibility. On the other hand, the narrower the bandwidth, the higher the losses. Previous teleportation implementations had rather low count rates (1.2 MHz for 320 MHz excitation rate [34]), which would be even lowered when adding a spectral filter. But, a decent signal is crucial for the experiment because three-fold coincidences are collected. For this reason, a good trade-off between linewidth filtering and signal loss has to be selected.
To sum up, we are currently investigating samples that have nearly Fourier-limited linewidths, high count rates and good entanglement. Switching from the current sample structure as explained in Section 3.5.3 (GaAs *QDs* in DBR + solid immersion lens) to GaAs *QDs* in second-order Bragg grating cavities might conclude the search. These cavities would shorten the lifetimes and enhance the extraction efficiency [30, 191], two key parameters for high *HOM* visibility and acceptable count rates, which are currently limiting the experimental validation.

State-of-the-art GaAs *QDs* seem to be on the verge of demonstrating their viability as core elements of quantum repeaters. The proposed quantum teleportation is currently limited by the variance in the fabrication process. However, suggestions for improvements, as switching to samples using second-order Bragg grating cavities, have already been proposed and currently no fundamental limits seem to restrict their development. Also, preliminary estimations predict that state-of-the-art *QDs* even without spectral filtering and considering a realistic engineering of Purcell enhancement could achieve an entanglement swapping fidelity of above 93 % [154]. Combining this fidelity with a quantum memory that is compatible with the bandwidth of semiconductor *QDs*, i.e., an atomic-frequency-comb memory with a fidelity of 95 % and a bandwidth of 1.5 GHz [192], a total swapping fidelity above 84 % is expected [73]. This total fidelity would allow a significant violation of Bell's inequality and would even be high enough for implementing common quantum key distribution protocols [3]. These estimations are quite promising that, when combining the

best technologies, the proof of principle of GaAs *QDs* as cores of quantum repeater nodes is within reach.

Bibliography

[1] R. Impagliazzo and M. Luby. One-way functions are essential for complexity based cryptography. In *30th Annual Symposium on Foundations of Computer Science*, pages 230–235, October 1989. doi: 10.1109/SFCS.1989.63483.

[2] Peter W. Shor. Polynomial-Time Algorithms for Prime Factorization and Discrete Logarithms on a Quantum Computer. *SIAM Journal on Computing*, 26(5):1484–1509, October 1997. ISSN 0097-5397. doi: 10.1137/S0097539795293172. URL https://epubs.siam.org/doi/10.1137/S0097539795293172.

[3] Peter W. Shor and John Preskill. Simple Proof of Security of the BB84 Quantum Key Distribution Protocol. *Physical Review Letters*, 85(2):441–444, July 2000. doi: 10.1103/PhysRevLett.85.441. URL https://link.aps.org/doi/10.1103/PhysRevLett.85.441.

[4] Nicolas Gisin, Grégoire Ribordy, Wolfgang Tittel, and Hugo Zbinden. Quantum cryptography. *Reviews of Modern Physics*, 74(1):145–195, March 2002. ISSN 0034-6861, 1539-0756. doi: 10.1103/RevModPhys.74.145. URL https://link.aps.org/doi/10.1103/RevModPhys.74.145.

[5] W. K. Wootters and W. H. Zurek. A single quantum cannot be cloned. *Nature*, 299(5886):802–803, October 1982. ISSN 0028-0836, 1476-4687. doi: 10.1038/299802a0. URL http://www.nature.com/articles/299802a0.

[6] Sylvain Hermelin, Shintaro Takada, Michihisa Yamamoto, Seigo Tarucha, Andreas D. Wieck, Laurent Saminadayar, Christopher Bäuerle, and Tristan Meunier. Electrons surfing on a sound wave as a platform for quantum optics with flying electrons. *Nature*, 477(7365):435–438, September 2011. ISSN 1476-4687. doi: 10.1038/nature10416. URL https://www.nature.com/articles/nature10416.

[7] R. P. G. McNeil, M. Kataoka, C. J. B. Ford, C. H. W. Barnes, D. Anderson, G. a. C. Jones, I. Farrer, and D. A. Ritchie. On-demand single-electron transfer between distant quantum dots. *Nature*, 477(7365):439–442, September 2011. ISSN 1476-4687. doi: 10.1038/nature10444. URL https://www.nature.com/articles/nature10444.

[8] G. Wendin. Quantum information processing with superconducting circuits: a review. *Reports on Progress in Physics*, 80(10):106001, September 2017. ISSN 0034-4885. doi: 10.1088/1361-6633/aa7e1a. URL https://doi.org/10.1088/1361-6633/aa7e1a.

[9] Jeremy L. O'Brien, Akira Furusawa, and Jelena Vučković. Photonic quantum technologies. *Nature Photonics*, 3(12):687–695, December 2009. ISSN 1749-4893. doi: 10.1038/nphoton.2009.229. URL https://www.nature.com/articles/nphoton.2009.229.

[10] Fulvio Flamini, Nicolò Spagnolo, and Fabio Sciarrino. Photonic quantum information processing: a review. *Reports on Progress in Physics*, 82(1):016001, November 2018. ISSN 0034-4885. doi: 10.1088/1361-6633/aad5b2. URL https://doi.org/10.1088/1361-6633/aad5b2.

[11] Stefano Pirandola, Riccardo Laurenza, Carlo Ottaviani, and Leonardo Banchi. Fundamental limits of repeaterless quantum communications. *Nature Communications*, 8(1):15043, April 2017. ISSN 2041-1723. doi: 10.1038/ncomms15043. URL https://www.nature.com/articles/ncomms15043.

[12] Cristian Antonelli, Mark Shtaif, and Misha Brodsky. Sudden Death of Entanglement Induced by Polarization Mode Dispersion. *Physical Review Letters*, 106(8):080404, February 2011. doi: 10.1103/PhysRevLett.106.080404. URL https://link.aps.org/doi/10.1103/PhysRevLett.106.080404.

[13] W. J. Munro, A. M. Stephens, S. J. Devitt, K. A. Harrison, and Kae Nemoto. Quantum communication without the necessity of quantum memories. *Nature Photonics*, 6(11):777–781, November 2012. ISSN 1749-4893. doi: 10.1038/nphoton.2012.243. URL https://www.nature.com/articles/nphoton.2012.243.

[14] Johannes Borregaard, Hannes Pichler, Tim Schröder, Mikhail D. Lukin, Peter Lodahl, and Anders S. Sørensen. One-Way Quantum Repeater Based on Near-Deterministic Photon-Emitter Interfaces. *Physical Review X*, 10(2):021071, June 2020. doi: 10.1103/PhysRevX.10.021071. URL https://link.aps.org/doi/10.1103/PhysRevX.10.021071.

[15] Nicolas Sangouard, Christoph Simon, Hugues de Riedmatten, and Nicolas Gisin. Quantum repeaters based on atomic ensembles and linear optics. *Reviews of Modern Physics*, 83(1):33–80, March 2011. doi: 10.1103/RevModPhys.83.33. URL https://link.aps.org/doi/10.1103/RevModPhys.83.33.

[16] M. Żukowski, A. Zeilinger, M. A. Horne, and A. K. Ekert. "Event-ready-detectors" Bell experiment via entanglement swapping. *Physical Review Letters*, 71(26):4287–4290, December 1993. ISSN 0031-9007. doi: 10.1103/PhysRevLett.71.4287. URL https://link.aps.org/doi/10.1103/PhysRevLett.71.4287.

[17] H.-J. Briegel, W. Dür, J. I. Cirac, and P. Zoller. Quantum Repeaters: The Role of Imperfect Local Operations in Quantum Communication. *Physical Review Letters*, 81(26):5932–5935, December 1998. ISSN 0031-9007, 1079-7114. doi: 10.1103/PhysRevLett.81.5932. URL https://link.aps.org/doi/10.1103/PhysRevLett.81.5932.

[18] Jian-Wei Pan, Dik Bouwmeester, Harald Weinfurter, and Anton Zeilinger. Experimental entanglement swapping: entangling photons that never interacted. *Physical Review Letters*, 80(18):3891–3894, May 1998.

[19] Paul G. Kwiat, Klaus Mattle, Harald Weinfurter, Anton Zeilinger, Alexander V. Sergienko, and Yanhua Shih. New High-Intensity Source of Polarization-Entangled Photon Pairs. *Physical Review Letters*, 75(24):4337–4341, December 1995. doi: 10.1103/PhysRevLett.75.4337. URL `https://link.aps.org/doi/10.1103/PhysRevLett.75.4337`.

[20] Han-Sen Zhong, Yuan Li, Wei Li, Li-Chao Peng, Zu-En Su, Yi Hu, Yu-Ming He, Xing Ding, Weijun Zhang, Hao Li, Lu Zhang, Zhen Wang, Lixing You, Xi-Lin Wang, Xiao Jiang, Li Li, Yu-Ao Chen, Nai-Le Liu, Chao-Yang Lu, and Jian-Wei Pan. 12-Photon Entanglement and Scalable Scattershot Boson Sampling with Optimal Entangled-Photon Pairs from Parametric Down-Conversion. *Physical Review Letters*, 121(25):250505, December 2018. doi: 10.1103/PhysRevLett.121.250505. URL `https://link.aps.org/doi/10.1103/PhysRevLett.121.250505`.

[21] Masahiro Takeoka, Rui-Bo Jin, and Masahide Sasaki. Full analysis of multi-photon pair effects in spontaneous parametric down conversion based photonic quantum information processing. *New Journal of Physics*, 17(4):043030, April 2015. ISSN 1367-2630. doi: 10.1088/1367-2630/17/4/043030. URL `https://doi.org/10.1088/1367-2630/17/4/043030`.

[22] Radim Hošák, Ivo Straka, Ana Predojević, Radim Filip, and Miroslav Ježek. Effect of source statistics on utilizing photon entanglement in quantum key distribution. *Physical Review A*, 103(4):042411, April 2021. doi: 10.1103/PhysRevA.103.042411. URL `https://link.aps.org/doi/10.1103/PhysRevA.103.042411`. Publisher: American Physical Society.

[23] Francesco Basso Basset, Mauro Valeri, Emanuele Roccia, Valerio Muredda, Davide Poderini, Julia Neuwirth, Nicolò Spagnolo, Michele B. Rota, Gonzalo Carvacho, Fabio Sciarrino, and Rinaldo Trotta. Quantum key distribution with entangled photons generated on demand by a quantum dot. *Science Advances*, 7(12):eabe6379, March 2021. doi: 10.1126/sciadv.abe6379. URL `https://www.science.org/doi/10.1126/sciadv.abe6379`.

[24] V. Scarani, H. de Riedmatten, I. Marcikic, H. Zbinden, and N. Gisin. Four-photon correction in two-photon Bell experiments. *The European Physical Journal D*, 32(1):129–138, January 2005. ISSN 1434-6060, 1434-6079. doi: 10.1140/epjd/e2004-00170-7. URL `https://epjd.epj.org/articles/epjd/abs/2005/01/d04209/d04209.html`.

[25] M. Müller, S. Bounouar, K. D. Jöns, M. Glässl, and P. Michler. On-demand generation of indistinguishable polarization-entangled photon pairs. *Nature Photonics*, 8(3):224–228, March 2014. ISSN 1749-4885, 1749-4893. doi: 10.1038/nphoton.2013.377. URL `http://www.nature.com/articles/nphoton.2013.377`.

[26] Oliver Benson, Charles Santori, Matthew Pelton, and Yoshihisa Yamamoto. Regulated and Entangled Photons from a Single Quantum Dot. *Physical Review Letters*, 84(11):2513–2516, March 2000. ISSN 0031-9007, 1079-7114. doi: 10.1103/PhysRevLett.84.2513. URL `https://link.aps.org/doi/10.1103/PhysRevLett.84.2513`.

[27] Lukas Hanschke, Kevin A. Fischer, Stefan Appel, Daniil Lukin, Jakob Wierzbowski, Shuo Sun, Rahul Trivedi, Jelena Vučković, Jonathan J. Finley, and Kai Müller. Quantum dot

single-photon sources with ultra-low multi-photon probability. *npj Quantum Information*, 4(1):43, December 2018. ISSN 2056-6387. doi: 10.1038/s41534-018-0092-0. URL `http://www.nature.com/articles/s41534-018-0092-0`.

[28] Lucas Schweickert, Klaus D. Jöns, Katharina D. Zeuner, Saimon Filipe Covre da Silva, Huiying Huang, Thomas Lettner, Marcus Reindl, Julien Zichi, Rinaldo Trotta, Armando Rastelli, and Val Zwiller. On-demand generation of background-free single photons from a solid-state source. *Applied Physics Letters*, 112(9):093106, February 2018. ISSN 0003-6951, 1077-3118. doi: 10.1063/1.5020038. URL `http://aip.scitation.org/doi/10.1063/1.5020038`.

[29] Jin Liu, Rongbin Su, Yuming Wei, Beimeng Yao, Saimon Filipe Covre da Silva, Ying Yu, Jake Iles-Smith, Kartik Srinivasan, Armando Rastelli, Juntao Li, and Xuehua Wang. A solid-state source of strongly entangled photon pairs with high brightness and indistinguishability. *Nature Nanotechnology*, 14(6):586–593, June 2019. ISSN 1748-3395. doi: 10.1038/s41565-019-0435-9. URL `https://www.nature.com/articles/s41565-019-0435-9`.

[30] Hui Wang, Hai Hu, T.-H. Chung, Jian Qin, Xiaoxia Yang, J.-P. Li, R.-Z. Liu, H.-S. Zhong, Y.-M. He, Xing Ding, Y.-H. Deng, Qing Dai, Y.-H. Huo, Sven Höfling, Chao-Yang Lu, and Jian-Wei Pan. On-Demand Semiconductor Source of Entangled Photons Which Simultaneously Has High Fidelity, Efficiency, and Indistinguishability. *Physical Review Letters*, 122(11): 113602, March 2019. ISSN 0031-9007, 1079-7114. doi: 10.1103/PhysRevLett.122.113602. URL `https://link.aps.org/doi/10.1103/PhysRevLett.122.113602`.

[31] Rinaldo Trotta, Javier Martín-Sánchez, Istvan Daruka, Carmine Ortix, and Armando Rastelli. Energy-Tunable Sources of Entangled Photons: A Viable Concept for Solid-State-Based Quantum Relays. *Physical Review Letters*, 114(15):150502, April 2015. doi: 10.1103/PhysRevLett.114.150502. URL `https://link.aps.org/doi/10.1103/PhysRevLett.114.150502`.

[32] Rinaldo Trotta, Javier Martín-Sánchez, Johannes S. Wildmann, Giovanni Piredda, Marcus Reindl, Christian Schimpf, Eugenio Zallo, Sandra Stroj, Johannes Edlinger, and Armando Rastelli. Wavelength-tunable sources of entangled photons interfaced with atomic vapours. *Nature Communications*, 7:10375, January 2016. ISSN 2041-1723. doi: 10.1038/ncomms10375. URL `http://www.nature.com/doifinder/10.1038/ncomms10375`.

[33] Marcus Reindl, Daniel Huber, Christian Schimpf, Saimon F. Covre da Silva, Michele B. Rota, Huiying Huang, Val Zwiller, Klaus D. Jöns, Armando Rastelli, and Rinaldo Trotta. All-photonic quantum teleportation using on-demand solid-state quantum emitters. *Science Advances*, 4(12):eaau1255, December 2018. ISSN 2375-2548. doi: 10.1126/sciadv.aau1255. URL `https://advances.sciencemag.org/content/4/12/eaau1255`.

[34] F. Basso Basset, F. Salusti, L. Schweickert, M. B. Rota, D. Tedeschi, S. F. Covre da Silva, E. Roccia, V. Zwiller, K. D. Jöns, A. Rastelli, and R. Trotta. Quantum teleportation with imperfect quantum dots. *npj Quantum Information*, 7(1):1–9, January 2021. ISSN

2056-6387. doi: 10.1038/s41534-020-00356-0. URL https://www.nature.com/articles/s41534-020-00356-0.

[35] F. Basso Basset, M. B. Rota, C. Schimpf, D. Tedeschi, K. D. Zeuner, S. F. Covre da Silva, M. Reindl, V. Zwiller, K. D. Jöns, A. Rastelli, and R. Trotta. Entanglement Swapping with Photons Generated on Demand by a Quantum Dot. *Physical Review Letters*, 123(16):160501, October 2019. doi: 10.1103/PhysRevLett.123.160501. URL https://link.aps.org/doi/10.1103/PhysRevLett.123.160501.

[36] Saimon Filipe Covre da Silva, Gabriel Undeutsch, Barbara Lehner, Santanu Manna, Tobias M. Krieger, Marcus Reindl, Christian Schimpf, Rinaldo Trotta, and Armando Rastelli. GaAs quantum dots grown by droplet etching epitaxy as quantum light sources. *Applied Physics Letters*, 119(12):120502, September 2021. ISSN 0003-6951. doi: 10.1063/5.0057070. URL https://aip.scitation.org/doi/10.1063/5.0057070.

[37] Daniel Huber, Marcus Reindl, Saimon Filipe Covre da Silva, Christian Schimpf, Javier Martín-Sánchez, Huiying Huang, Giovanni Piredda, Johannes Edlinger, Armando Rastelli, and Rinaldo Trotta. Strain-Tunable GaAs Quantum Dot: A Nearly Dephasing-Free Source of Entangled Photon Pairs on Demand. *Physical Review Letters*, 121(3):0033902, July 2018. ISSN 0031-9007, 1079-7114. doi: 10.1103/PhysRevLett.121.033902. URL https://link.aps.org/doi/10.1103/PhysRevLett.121.033902.

[38] Michael A. Nielsen and Isaac L. Chuang. *Quantum computation and quantum information*. Cambridge University Press, Cambridge ; New York, 2000. ISBN 978-0-521-63235-5 978-0-521-63503-5.

[39] Rainer Blatt and David Wineland. Entangled states of trapped atomic ions. *Nature*, 453 (7198):1008–1015, June 2008. ISSN 1476-4687. doi: 10.1038/nature07125. URL https://www.nature.com/articles/nature07125.

[40] B. E. Kane. A silicon-based nuclear spin quantum computer. *Nature*, 393(6681):133–137, May 1998. ISSN 1476-4687. doi: 10.1038/30156. URL https://www.nature.com/articles/30156.

[41] Andrea Morello, Jarryd J. Pla, Floris A. Zwanenburg, Kok W. Chan, Kuan Y. Tan, Hans Huebl, Mikko Möttönen, Christopher D. Nugroho, Changyi Yang, Jessica A. van Donkelaar, Andrew D. C. Alves, David N. Jamieson, Christopher C. Escott, Lloyd C. L. Hollenberg, Robert G. Clark, and Andrew S. Dzurak. Single-shot readout of an electron spin in silicon. *Nature*, 467(7316):687–691, October 2010. ISSN 1476-4687. doi: 10.1038/nature09392. URL https://www.nature.com/articles/nature09392.

[42] Richard J. Warburton. Single spins in self-assembled quantum dots. *Nature Materials*, 12(6): 483–493, June 2013. ISSN 1476-4660. doi: 10.1038/nmat3585. URL https://www.nature.com/articles/nmat3585.

[43] John Clarke and Frank K. Wilhelm. Superconducting quantum bits. *Nature*, 453(7198):1031–1042, June 2008. ISSN 1476-4687. doi: 10.1038/nature07128. URL https://www.nature.com/articles/nature07128.

[44] J. C. Loredo, C. Antón, B. Reznychenko, P. Hilaire, A. Harouri, C. Millet, H. Ollivier, N. Somaschi, L. De Santis, A. Lemaître, I. Sagnes, L. Lanco, A. Auffèves, O. Krebs, and P. Senellart. Generation of non-classical light in a photon-number superposition. *Nature Photonics*, 13(11):803–808, November 2019. ISSN 1749-4893. doi: 10.1038/s41566-019-0506-3. URL https://www.nature.com/articles/s41566-019-0506-3.

[45] J. Brendel, N. Gisin, W. Tittel, and H. Zbinden. Pulsed Energy-Time Entangled Twin-Photon Source for Quantum Communication. *Physical Review Letters*, 82(12):2594–2597, March 1999. doi: 10.1103/PhysRevLett.82.2594. URL https://link.aps.org/doi/10.1103/PhysRevLett.82.2594.

[46] Manuel Erhard, Robert Fickler, Mario Krenn, and Anton Zeilinger. Twisted photons: new quantum perspectives in high dimensions. *Light: Science & Applications*, 7(3):17146–17146, March 2018. ISSN 2047-7538. doi: 10.1038/lsa.2017.146. URL https://www.nature.com/articles/lsa2017146.

[47] Pieter Kok, W. J. Munro, Kae Nemoto, T. C. Ralph, Jonathan P. Dowling, and G. J. Milburn. Linear optical quantum computing with photonic qubits. *Reviews of Modern Physics*, 79(1):135–174, January 2007. doi: 10.1103/RevModPhys.79.135. URL https://link.aps.org/doi/10.1103/RevModPhys.79.135.

[48] S. Pirandola, S. Pirandola, U. L. Andersen, L. Banchi, M. Berta, D. Bunandar, R. Colbeck, D. Englund, T. Gehring, C. Lupo, C. Ottaviani, J. L. Pereira, M. Razavi, J. Shamsul Shaari, J. Shamsul Shaari, M. Tomamichel, M. Tomamichel, V. C. Usenko, G. Vallone, P. Villoresi, and P. Wallden. Advances in quantum cryptography. *Advances in Optics and Photonics*, 12(4):1012–1236, December 2020. ISSN 1943-8206. doi: 10.1364/AOP.361502. URL https://www.osapublishing.org/aop/abstract.cfm?uri=aop-12-4-1012.

[49] Charles H. Bennett and Gilles Brassard. Quantum cryptography: Public key distribution and coin tossing. *Theoretical Computer Science*, 560:7–11, December 2014. ISSN 03043975. doi: 10.1016/j.tcs.2014.05.025. URL https://linkinghub.elsevier.com/retrieve/pii/S0304397514004241.

[50] Artur K. Ekert. Quantum cryptography based on Bell's theorem. *Physical Review Letters*, 67(6):661–663, August 1991. ISSN 0031-9007. doi: 10.1103/PhysRevLett.67.661.

[51] A. Einstein, B. Podolsky, and N. Rosen. Can Quantum-Mechanical Description of Physical Reality Be Considered Complete? *Physical Review*, 47(10):777–780, May 1935. doi: 10.1103/PhysRev.47.777. URL https://link.aps.org/doi/10.1103/PhysRev.47.777.

[52] J. S. Bell. On the Einstein Podolsky Rosen paradox. *Physics Physique Fizika*, 1(3):195–200, November 1964. doi: 10.1103/PhysicsPhysiqueFizika.1.195. URL https://link.aps.org/doi/10.1103/PhysicsPhysiqueFizika.1.195.

[53] John F. Clauser, Michael A. Horne, Abner Shimony, and Richard A. Holt. Proposed Experiment to Test Local Hidden-Variable Theories. *Physical Review Letters*, 23(15):880–884, October 1969. doi: 10.1103/PhysRevLett.23.880. URL https://link.aps.org/doi/10.1103/PhysRevLett.23.880.

[54] Miralem Mehic, Marcin Niemiec, Harun Siljak, and Miroslav Voznak. Error Reconciliation in Quantum Key Distribution Protocols. In Irek Ulidowski, Ivan Lanese, Ulrik Pagh Schultz, and Carla Ferreira, editors, *Reversible Computation: Extending Horizons of Computing: Selected Results of the COST Action IC1405*, Lecture Notes in Computer Science, pages 222–236. Springer International Publishing, Cham, 2020. ISBN 978-3-030-47361-7. doi: 10.1007/978-3-030-47361-7_11. URL https://doi.org/10.1007/978-3-030-47361-7_11.

[55] Antonio Acín, Nicolas Brunner, Nicolas Gisin, Serge Massar, Stefano Pironio, and Valerio Scarani. Device-Independent Security of Quantum Cryptography against Collective Attacks. *Physical Review Letters*, 98(23):230501, June 2007. doi: 10.1103/PhysRevLett.98.230501. URL https://link.aps.org/doi/10.1103/PhysRevLett.98.230501.

[56] L. Trevisan. Extractors and pseudorandom generators. *Journal of the ACM*, 48(4):860–879, July 2001. ISSN 0004-5411. doi: 10.1145/502090.502099. URL https://doi.org/10.1145/502090.502099.

[57] C. E. Shannon. Communication theory of secrecy systems. *The Bell System Technical Journal*, 28(4):656–715, October 1949. ISSN 0005-8580. doi: 10.1002/j.1538-7305.1949.tb00928.x. Conference Name: The Bell System Technical Journal.

[58] Daniel A. Vajner, Lucas Rickert, Timm Gao, Koray Kaymazlar, and Tobias Heindel. Quantum Communication Using Semiconductor Quantum Dots. *Advanced Quantum Technologies*, 5(7):2100116, 2022. ISSN 2511-9044. doi: 10.1002/qute.202100116. URL https://onlinelibrary.wiley.com/doi/abs/10.1002/qute.202100116.

[59] Alberto Boaron, Gianluca Boso, Davide Rusca, Cédric Vulliez, Claire Autebert, Misael Caloz, Matthieu Perrenoud, Gaëtan Gras, Félix Bussières, Ming-Jun Li, Daniel Nolan, Anthony Martin, and Hugo Zbinden. Secure Quantum Key Distribution over 421 km of Optical Fiber. *Physical Review Letters*, 121(19):190502, November 2018. doi: 10.1103/PhysRevLett.121.190502. URL https://link.aps.org/doi/10.1103/PhysRevLett.121.190502.

[60] S. Lloyd, M. S. Shahriar, J. H. Shapiro, and P. R. Hemmer. Long Distance, Unconditional Teleportation of Atomic States via Complete Bell State Measurements. *Physical Review Letters*, 87(16), September 2001. ISSN 0031-9007, 1079-7114. doi: 10.1103/PhysRevLett.87.167903. URL https://link.aps.org/doi/10.1103/PhysRevLett.87.167903.

[61] Peter van Loock, Wolfgang Alt, Christoph Becher, Oliver Benson, Holger Boche, Christian Deppe, Jürgen Eschner, Sven Höfling, Dieter Meschede, Peter Michler, Frank Schmidt, and Harald Weinfurter. Extending Quantum Links: Modules for Fiber- and Memory-Based Quantum Repeaters. *Advanced Quantum Technologies*, 3(11):1900141, 2020. ISSN 2511-9044. doi: https://doi.org/10.1002/qute.201900141. URL `https://onlinelibrary.wiley.com/doi/abs/10.1002/qute.201900141`.

[62] Johannes Borregaard, Anders Søndberg Sørensen, and Peter Lodahl. Quantum Networks with Deterministic Spin–Photon Interfaces. *Advanced Quantum Technologies*, 2(5-6):1800091, 2019. ISSN 2511-9044. doi: https://doi.org/10.1002/qute.201800091. URL `https://onlinelibrary.wiley.com/doi/abs/10.1002/qute.201800091`.

[63] R. Stockill, C. Le Gall, C. Matthiesen, L. Huthmacher, E. Clarke, M. Hugues, and M. Atatüre. Quantum dot spin coherence governed by a strained nuclear environment. *Nature Communications*, 7(1):12745, September 2016. ISSN 2041-1723. doi: 10.1038/ncomms12745. URL `https://www.nature.com/articles/ncomms12745`.

[64] Dan Cogan, Oded Kenneth, Netanel H. Lindner, Giora Peniakov, Caspar Hopfmann, Dan Dalacu, Philip J. Poole, Pawel Hawrylak, and David Gershoni. Depolarization of Electronic Spin Qubits Confined in Semiconductor Quantum Dots. *Physical Review X*, 8(4):041050, December 2018. doi: 10.1103/PhysRevX.8.041050. URL `https://link.aps.org/doi/10.1103/PhysRevX.8.041050`.

[65] Koji Azuma, Kiyoshi Tamaki, and Hoi-Kwong Lo. All-photonic quantum repeaters. *Nature Communications*, 6(1):6787, November 2015. ISSN 2041-1723. doi: 10.1038/ncomms7787. URL `http://www.nature.com/articles/ncomms7787`.

[66] Robert Raussendorf and Hans J. Briegel. A One-Way Quantum Computer. *Physical Review Letters*, 86(22):5188–5191, May 2001. doi: 10.1103/PhysRevLett.86.5188. URL `https://link.aps.org/doi/10.1103/PhysRevLett.86.5188`.

[67] I. Schwartz, D. Cogan, E. R. Schmidgall, Y. Don, L. Gantz, O. Kenneth, N. H. Lindner, and D. Gershoni. Deterministic generation of a cluster state of entangled photons. *Science*, 354 (6311):434–437, October 2016. ISSN 0036-8075, 1095-9203. doi: 10.1126/science.aah4758. URL `http://www.sciencemag.org/cgi/doi/10.1126/science.aah4758`.

[68] Zheng-Da Li, Rui Zhang, Xu-Fei Yin, Li-Zheng Liu, Yi Hu, Yu-Qiang Fang, Yue-Yang Fei, Xiao Jiang, Jun Zhang, Li Li, Nai-Le Liu, Feihu Xu, Yu-Ao Chen, and Jian-Wei Pan. Experimental quantum repeater without quantum memory. *Nature Photonics*, June 2019. ISSN 1749-4885, 1749-4893. doi: 10.1038/s41566-019-0468-5. URL `http://www.nature.com/articles/s41566-019-0468-5`.

[69] Jinxian Guo, Xiaotian Feng, Peiyu Yang, Zhifei Yu, L. Q. Chen, Chun-Hua Yuan, and Weiping Zhang. High-performance Raman quantum memory with optimal control in room temperature atoms. *Nature Communications*, 10(1):148, January 2019. ISSN

2041-1723. doi: 10.1038/s41467-018-08118-5. URL https://www.nature.com/articles/s41467-018-08118-5.

[70] Frédéric Grosshans and Philippe Grangier. Quantum cloning and teleportation criteria for continuous quantum variables. *Physical Review A*, 64(1):010301, June 2001. doi: 10.1103/PhysRevA.64.010301. URL https://link.aps.org/doi/10.1103/PhysRevA.64.010301.

[71] G. T. Campbell, K. R. Ferguson, M. J. Sellars, B. C. Buchler, and P. K. Lam. Echo-Based Quantum Memory. In *Quantum Information*, pages 723–740. John Wiley & Sons, Ltd, 2016. ISBN 978-3-527-80578-5. doi: 10.1002/9783527805785.ch32. URL https://onlinelibrary.wiley.com/doi/abs/10.1002/9783527805785.ch32. Section: 32 _eprint: https://onlinelibrary.wiley.com/doi/pdf/10.1002/9783527805785.ch32.

[72] G. T. Campbell, K. R. Ferguson, M. J. Sellars, B. C. Buchler, and P. K. Lam. Echo-Based Quantum Memory. *arXiv:1902.04313 [physics, physics:quant-ph]*, February 2019. URL http://arxiv.org/abs/1902.04313. arXiv: 1902.04313.

[73] Julia Neuwirth, Francesco Basso Basset, Michele B. Rota, Emanuele Roccia, Christian Schimpf, Klaus D. Jöns, Armando Rastelli, and Rinaldo Trotta. Quantum dot technology for quantum repeaters: from entangled photon generation toward the integration with quantum memories. *Materials for Quantum Technology*, 1(4):043001, December 2021. ISSN 2633-4356. doi: 10.1088/2633-4356/ac3d14. URL https://doi.org/10.1088/2633-4356/ac3d14.

[74] J. Nilsson, R. M. Stevenson, K. H. A. Chan, J. Skiba-Szymanska, M. Lucamarini, M. B. Ward, A. J. Bennett, C. L. Salter, I. Farrer, D. A. Ritchie, and A. J. Shields. Quantum teleportation using a light-emitting diode. *Nature Photonics*, 7(4):311–315, April 2013. ISSN 1749-4885, 1749-4893. doi: 10.1038/nphoton.2013.10. URL http://www.nature.com/articles/nphoton.2013.10.

[75] Michael Zopf, Robert Keil, Yan Chen, Jingzhong Yang, Disheng Chen, Fei Ding, and Oliver G. Schmidt. Entanglement Swapping with Semiconductor-Generated Photons Violates Bell's Inequality. *Physical Review Letters*, 123(16):160502, October 2019. doi: 10.1103/PhysRevLett.123.160502. URL https://link.aps.org/doi/10.1103/PhysRevLett.123.160502.

[76] C. K. Hong, Z. Y. Ou, and L. Mandel. Measurement of subpicosecond time intervals between two photons by interference. *Physical Review Letters*, 59(18):2044–2046, November 1987. doi: 10.1103/PhysRevLett.59.2044. URL https://link.aps.org/doi/10.1103/PhysRevLett.59.2044.

[77] Yoon-Ho Kim, Sergei P. Kulik, and Yanhua Shih. Quantum Teleportation of a Polarization State with a Complete Bell State Measurement. *Physical Review Letters*, 86(7):1370–1373, February 2001. ISSN 0031-9007, 1079-7114. doi: 10.1103/PhysRevLett.86.1370. URL https://link.aps.org/doi/10.1103/PhysRevLett.86.1370.

[78] Juan Yin, Yuan Cao, Yu-Huai Li, Sheng-Kai Liao, Liang Zhang, Ji-Gang Ren, Wen-Qi Cai, Wei-Yue Liu, Bo Li, Hui Dai, Guang-Bing Li, Qi-Ming Lu, Yun-Hong Gong, Yu Xu, Shuang-

Lin Li, Feng-Zhi Li, Ya-Yun Yin, Zi-Qing Jiang, Ming Li, Jian-Jun Jia, Ge Ren, Dong He, Yi-Lin Zhou, Xiao-Xiang Zhang, Na Wang, Xiang Chang, Zhen-Cai Zhu, Nai-Le Liu, Yu-Ao Chen, Chao-Yang Lu, Rong Shu, Cheng-Zhi Peng, Jian-Yu Wang, and Jian-Wei Pan. Satellite-based entanglement distribution over 1200 kilometers. *Science*, 356(6343):1140–1144, June 2017. ISSN 0036-8075, 1095-9203. doi: 10.1126/science.aan3211. URL `http://www.sciencemag.org/lookup/doi/10.1126/science.aan3211`.

[79] James Schneeloch, Samuel H. Knarr, Daniela F. Bogorin, Mackenzie L. Levangie, Christopher C. Tison, Rebecca Frank, Gregory A. Howland, Michael L. Fanto, and Paul M. Alsing. Introduction to the absolute brightness and number statistics in spontaneous parametric down-conversion. *Journal of Optics*, 21(4):043501, February 2019. ISSN 2040-8986. doi: 10.1088/2040-8986/ab05a8. URL `https://doi.org/10.1088/2040-8986/ab05a8`.

[80] Daniel Huber, Marcus Reindl, Yongheng Huo, Huiying Huang, Johannes S. Wildmann, Oliver G. Schmidt, Armando Rastelli, and Rinaldo Trotta. Highly indistinguishable and strongly entangled photons from symmetric GaAs quantum dots. *Nature Communications*, 8:15506, May 2017. ISSN 2041-1723. doi: 10.1038/ncomms15506. URL `http://www.nature.com/doifinder/10.1038/ncomms15506`.

[81] D. Leonard, M. Krishnamurthy, C. M. Reaves, S. P. Denbaars, and P. M. Petroff. Direct formation of quantum-sized dots from uniform coherent islands of InGaAs on GaAs surfaces. *Applied Physics Letters*, 63(23):3203–3205, December 1993. ISSN 0003-6951. doi: 10.1063/1.110199. URL `https://aip.scitation.org/doi/10.1063/1.110199`.

[82] R. K. Singha, S. Manna, R. Bar, S. Das, and S. K. Ray. Surface potential, charging and local current transport of individual Ge quantum dots grown by molecular beam epitaxy. *Applied Surface Science*, 407:418–426, June 2017. ISSN 0169-4332. doi: 10.1016/j.apsusc.2017.02.212. URL `https://www.sciencedirect.com/science/article/pii/S0169433217305858`.

[83] A. Stemmann, T. Köppen, M. Grave, S. Wildfang, S. Mendach, W. Hansen, and Ch. Heyn. Local etching of nanoholes and quantum rings with InxGa1-x droplets. *Journal of Applied Physics*, 106(6):064315, September 2009. ISSN 0021-8979. doi: 10.1063/1.3225759. URL `https://aip.scitation.org/doi/10.1063/1.3225759`.

[84] Masahiro Watanabe Masahiro Watanabe, Toshiyuki Funayama Toshiyuki Funayama, Taishi Teraji Taishi Teraji, and Naoto Sakamaki Naoto Sakamaki. CaF2/CdF2 Double-Barrier Resonant Tunneling Diode with High Room-Temperature Peak-to-Valley Ratio. *Japanese Journal of Applied Physics*, 39(7B):L716, July 2000. ISSN 1347-4065. doi: 10.1143/JJAP.39.L716. URL `https://iopscience.iop.org/article/10.1143/JJAP.39.L716/meta`.

[85] Massimo Gurioli, Zhiming Wang, Armando Rastelli, Takashi Kuroda, and Stefano Sanguinetti. Droplet epitaxy of semiconductor nanostructures for quantum photonic devices. *Nature Materials*, 18(8):799–810, August 2019. ISSN 1476-4660. doi: 10.1038/s41563-019-0355-y. URL `https://www.nature.com/articles/s41563-019-0355-y`.

[86] Y. H. Huo, A. Rastelli, and O. G. Schmidt. Ultra-small excitonic fine structure splitting in highly symmetric quantum dots on GaAs (001) substrate. *Applied Physics Letters*, 102 (15):152105, April 2013. ISSN 0003-6951, 1077-3118. doi: 10.1063/1.4802088. URL `http://aip.scitation.org/doi/10.1063/1.4802088`.

[87] P. Atkinson, E. Zallo, and O. G. Schmidt. Independent wavelength and density control of uniform GaAs/AlGaAs quantum dots grown by infilling self-assembled nanoholes. *Journal of Applied Physics*, 112(5):054303, September 2012. ISSN 0021-8979. doi: 10.1063/1.4748183. URL `https://aip.scitation.org/doi/10.1063/1.4748183`.

[88] J.-P. Bourgoin, E. Meyer-Scott, B. L. Higgins, B. Helou, C. Erven, H. Hübel, B. Kumar, D. Hudson, I. D'Souza, R. Girard, R. Laflamme, and T. Jennewein. A comprehensive design and performance analysis of low Earth orbit satellite quantum communication. *New Journal of Physics*, 15(2):023006, February 2013. ISSN 1367-2630. doi: 10.1088/1367-2630/15/2/023006. URL `https://doi.org/10.1088/1367-2630/15/2/023006`.

[89] H. Benisty, H. De Neve, and C. Weisbuch. Impact of planar microcavity effects on light extraction-Part I: basic concepts and analytical trends. *IEEE Journal of Quantum Electronics*, 34(9):1612–1631, September 1998. ISSN 00189197. doi: 10.1109/3.709578. URL `http://ieeexplore.ieee.org/document/709578/`.

[90] W. L. Barnes, G. Björk, J. M. Gérard, P. Jonsson, J. a. E. Wasey, P. T. Worthing, and V. Zwiller. Solid-state single photon sources: light collection strategies. *The European Physical Journal D*, 18(2):197–210, February 2002. ISSN 1434-6060, 1434-6079. doi: 10.1140/epjd/e20020024. URL `https://epjd.epj.org/articles/epjd/abs/2002/02/d01174/d01174.html`.

[91] J. H Davies. *The physics of low-dimensional semiconductors: an introduction*. Cambridge University Press, Cambridge, U.K.; New York, NY, USA, 1998. ISBN 978-0-521-48148-9 978-0-521-48491-6. OCLC: 36259752.

[92] Lorenzo Pavesi and Mario Guzzi. Photoluminescence of AlxGa1-xAs alloys. *Journal of Applied Physics*, 75(10):4779–4842, May 1994. ISSN 0021-8979. doi: 10.1063/1.355769. URL `https://aip.scitation.org/doi/10.1063/1.355769`.

[93] R. J. Warburton, B. T. Miller, C. S. Dürr, C. Bödefeld, K. Karrai, J. P. Kotthaus, G. Medeiros-Ribeiro, P. M. Petroff, and S. Huant. Coulomb interactions in small charge-tunable quantum dots: A simple model. *Physical Review B*, 58(24):16221–16231, December 1998. doi: 10.1103/PhysRevB.58.16221. URL `https://link.aps.org/doi/10.1103/PhysRevB.58.16221`.

[94] A. S. Bracker, E. A. Stinaff, D. Gammon, M. E. Ware, J. G. Tischler, D. Park, D. Gershoni, A. V. Filinov, M. Bonitz, F. Peeters, and C. Riva. Binding energies of positive and negative trions: From quantum wells to quantum dots. *Physical Review B*, 72(3):035332, July 2005. doi: 10.1103/PhysRevB.72.035332. URL `https://link.aps.org/doi/10.1103/PhysRevB.72.035332`.

[95] Julia Neuwirth, Francesco Basso Basset, Michele B. Rota, Jan-Gabriel Hartel, Marc Sartison, Saimon F. Covre da Silva, Klaus D. Jöns, Armando Rastelli, and Rinaldo Trotta. A multipair-free source of entangled photons in the solid state, March 2022. URL `http://arxiv.org/abs/2203.17077`. arXiv:2203.17077 [to be published on Phys. Rev. B].

[96] G. Juska, E. Murray, V. Dimastrodonato, T. H. Chung, S. T. Moroni, A. Gocalinska, and E. Pelucchi. Conditions for entangled photon emission from (111)B site-controlled pyramidal quantum dots. *Journal of Applied Physics*, 117(13):134302, April 2015. ISSN 0021-8979. doi: 10.1063/1.4916705. URL `https://aip.scitation.org/doi/10.1063/1.4916705`.

[97] Y. Kodriano, E. Poem, N. H. Lindner, C. Tradonsky, B. D. Gerardot, P. M. Petroff, J. E. Avron, and D. Gershoni. Radiative cascade from quantum dot metastable spin-blockaded biexciton. *Physical Review B*, 82(15):155329, October 2010. doi: 10.1103/PhysRevB.82.155329. URL `https://link.aps.org/doi/10.1103/PhysRevB.82.155329`.

[98] Armando Rastelli, Mathieu Stoffel, Angelo Malachias, Tsvetelina Merdzhanova, Georgios Katsaros, Klaus Kern, Till H. Metzger, and Oliver G. Schmidt. Three-Dimensional Composition Profiles of Single Quantum Dots Determined by Scanning-Probe-Microscopy-Based Nanotomography. *Nano Letters*, 8(5):1404–1409, May 2008. ISSN 1530-6984. doi: 10.1021/nl080290y. URL `https://doi.org/10.1021/nl080290y`.

[99] M. Bayer, G. Ortner, O. Stern, A. Kuther, A. A. Gorbunov, A. Forchel, P. Hawrylak, S. Fafard, K. Hinzer, T. L. Reinecke, S. N. Walck, J. P. Reithmaier, F. Klopf, and F. Schäfer. Fine structure of neutral and charged excitons in self-assembled In(Ga)As/(Al)GaAs quantum dots. *Physical Review B*, 65(19), May 2002. ISSN 0163-1829, 1095-3795. doi: 10.1103/PhysRevB.65.195315. URL `https://link.aps.org/doi/10.1103/PhysRevB.65.195315`.

[100] A. J. Hudson, R. M. Stevenson, A. J. Bennett, R. J. Young, C. A. Nicoll, P. Atkinson, K. Cooper, D. A. Ritchie, and A. J. Shields. Coherence of an Entangled Exciton-Photon State. *Physical Review Letters*, 99(26):266802, December 2007. ISSN 0031-9007, 1079-7114. doi: 10.1103/PhysRevLett.99.266802. URL `https://link.aps.org/doi/10.1103/PhysRevLett.99.266802`.

[101] Robert Keil, Michael Zopf, Yan Chen, Bianca Höfer, Jiaxiang Zhang, Fei Ding, and Oliver G. Schmidt. Solid-state ensemble of highly entangled photon sources at rubidium atomic transitions. *Nature Communications*, 8(1):15501, May 2017. ISSN 2041-1723. doi: 10.1038/ncomms15501. URL `https://www.nature.com/articles/ncomms15501`.

[102] Marcus Reindl, Klaus D. Jöns, Daniel Huber, Christian Schimpf, Yongheng Huo, Val Zwiller, Armando Rastelli, and Rinaldo Trotta. Phonon-Assisted Two-Photon Interference from Remote Quantum Emitters. *Nano Letters*, 17(7):4090–4095, July 2017. ISSN 1530-6984. doi: 10.1021/acs.nanolett.7b00777. URL `https://doi.org/10.1021/acs.nanolett.7b00777`.

[103] R. Mark Stevenson, Andrew J. Hudson, Anthony J. Bennett, Robert J. Young, Christine A. Nicoll, David A. Ritchie, and Andrew J. Shields. Evolution of Entanglement

Between Distinguishable Light States. *Physical Review Letters*, 101(17):170501, October 2008. ISSN 0031-9007, 1079-7114. doi: 10.1103/PhysRevLett.101.170501. URL https://link.aps.org/doi/10.1103/PhysRevLett.101.170501.

[104] J. Huwer, R. M. Stevenson, J. Skiba-Szymanska, M. B. Ward, A. J. Shields, M. Felle, I. Farrer, D. A. Ritchie, and R. V. Penty. Quantum-Dot-Based Telecommunication-Wavelength Quantum Relay. *Physical Review Applied*, 8(2):024007, August 2017. ISSN 2331-7019. doi: 10.1103/PhysRevApplied.8.024007. URL https://link.aps.org/doi/10.1103/PhysRevApplied.8.024007.

[105] N. Akopian, N. H. Lindner, E. Poem, Y. Berlatzky, J. Avron, D. Gershoni, B. D. Gerardot, and P. M. Petroff. Entangled Photon Pairs from Semiconductor Quantum Dots. *Physical Review Letters*, 96(13), April 2006. ISSN 0031-9007, 1079-7114. doi: 10.1103/PhysRevLett.96.130501. URL https://link.aps.org/doi/10.1103/PhysRevLett.96.130501.

[106] Johannes David Plumhof, Rinaldo Trotta, Armando Rastelli, and Oliver G Schmidt. Experimental methods of post-growth tuning of the excitonic fine structure splitting in semiconductor quantum dots. *Nanoscale Research Letters*, 7(1):336, December 2012. ISSN 1556-276X. doi: 10.1186/1556-276X-7-336. URL https://nanoscalereslett.springeropen.com/articles/10.1186/1556-276X-7-336.

[107] A. J. Bennett, M. A. Pooley, R. M. Stevenson, M. B. Ward, R. B. Patel, A. Boyer de la Giroday, N. Sköld, I. Farrer, C. A. Nicoll, D. A. Ritchie, and A. J. Shields. Electric-field-induced coherent coupling of the exciton states in a single quantum dot. *Nature Physics*, 6(12):947–950, December 2010. ISSN 1745-2481. doi: 10.1038/nphys1780. URL https://www.nature.com/articles/nphys1780.

[108] J. D. Plumhof, V. Křápek, F. Ding, K. D. Jöns, R. Hafenbrak, P. Klenovský, A. Herklotz, K. Dörr, P. Michler, A. Rastelli, and O. G. Schmidt. Strain-induced anticrossing of bright exciton levels in single self-assembled GaAs/AlxGa1-xAs and InxGa1-xAs/GaAs quantum dots. *Physical Review B*, 83(12):121302, March 2011. doi: 10.1103/PhysRevB.83.121302. URL https://link.aps.org/doi/10.1103/PhysRevB.83.121302. Publisher: American Physical Society.

[109] Peter Michler. *Single Semiconductor Quantum Dots*. NanoScience and Technology. Springer, 1 edition, 2009. ISBN 978-3-540-87446-1.

[110] M. Grundmann and D. Bimberg. Theory of random population for quantum dots. *Physical Review B*, 55(15):9740–9745, April 1997. doi: 10.1103/PhysRevB.55.9740. URL https://link.aps.org/doi/10.1103/PhysRevB.55.9740.

[111] S. Stufler, P. Machnikowski, P. Ester, M. Bichler, V. M. Axt, T. Kuhn, and A. Zrenner. Two-photon Rabi oscillations in a single In x Ga 1 - x As \Ga As quantum dot. *Physical Review B*, 73(12):125304, March 2006. ISSN 1098-0121, 1550-235X. doi: 10.1103/PhysRevB.73.125304. URL https://link.aps.org/doi/10.1103/PhysRevB.73.125304.

[112] K. Brunner, G. Abstreiter, G. Böhm, G. Tränkle, and G. Weimann. Sharp-Line Photoluminescence and Two-Photon Absorption of Zero-Dimensional Biexcitons in a GaAs/AlGaAs Structure. *Physical Review Letters*, 73(8):1138–1141, August 1994. doi: 10.1103/PhysRevLett.73.1138. URL https://link.aps.org/doi/10.1103/PhysRevLett.73.1138.

[113] S. Bounouar, M. Müller, A. M. Barth, M. Glässl, V. M. Axt, and P. Michler. Phonon-assisted robust and deterministic two-photon biexciton preparation in a quantum dot. *Physical Review B*, 91(16):161302, April 2015. doi: 10.1103/PhysRevB.91.161302. URL https://link.aps.org/doi/10.1103/PhysRevB.91.161302.

[114] Harishankar Jayakumar, Ana Predojević, Tobias Huber, Thomas Kauten, Glenn S. Solomon, and Gregor Weihs. Deterministic Photon Pairs and Coherent Optical Control of a Single Quantum Dot. *Physical Review Letters*, 110(13):135505, March 2013. doi: 10.1103/PhysRevLett.110.135505. URL https://link.aps.org/doi/10.1103/PhysRevLett.110.135505. Publisher: American Physical Society.

[115] Pascale Senellart, Glenn Solomon, and Andrew White. High-performance semiconductor quantum-dot single-photon sources. *Nature Nanotechnology*, 12(11):1026–1039, November 2017. ISSN 1748-3387, 1748-3395. doi: 10.1038/nnano.2017.218. URL http://www.nature.com/doifinder/10.1038/nnano.2017.218.

[116] Caspar Hopfmann, Weijie Nie, Nand Lal Sharma, Carmen Weigelt, Fei Ding, and Oliver G. Schmidt. Maximally entangled and gigahertz-clocked on-demand photon pair source. *Physical Review B*, 103(7):075413, February 2021. doi: 10.1103/PhysRevB.103.075413. URL https://link.aps.org/doi/10.1103/PhysRevB.103.075413.

[117] Yan Chen, Michael Zopf, Robert Keil, Fei Ding, and Oliver G. Schmidt. Highly-efficient extraction of entangled photons from quantum dots using a broadband optical antenna. *Nature Communications*, 9(1):2994, July 2018. ISSN 2041-1723. doi: 10.1038/s41467-018-05456-2. URL https://www.nature.com/articles/s41467-018-05456-2.

[118] O. Gazzano, S. Michaelis de Vasconcellos, C. Arnold, A. Nowak, E. Galopin, I. Sagnes, L. Lanco, A. Lemaître, and P. Senellart. Bright solid-state sources of indistinguishable single photons. *Nature Communications*, 4(1):1425, December 2013. ISSN 2041-1723. doi: 10.1038/ncomms2434. URL http://www.nature.com/articles/ncomms2434.

[119] Luca Sapienza, Marcelo Davanço, Antonio Badolato, and Kartik Srinivasan. Nanoscale optical positioning of single quantum dots for bright and pure single-photon emission. *Nature Communications*, 6(1):7833, July 2015. ISSN 2041-1723. doi: 10.1038/ncomms8833. URL https://www.nature.com/articles/ncomms8833.

[120] N. Lütkenhaus, J. Calsamiglia, and K.-A. Suominen. Bell measurements for teleportation. *Physical Review A*, 59(5):3295–3300, May 1999. ISSN 1050-2947, 1094-1622. doi: 10.1103/PhysRevA.59.3295. URL https://link.aps.org/doi/10.1103/PhysRevA.59.3295.

[121] Dik Bouwmeester, Jian-Wei Pan, Klaus Mattle, Klaus Mattle, Harald Weinfurter, and Anton Zeilinger. Experimental quantum teleportation. *Nature*, 390:575–579, December 1997.

[122] Y. H. Shih and C. O. Alley. New Type of Einstein-Podolsky-Rosen-Bohm Experiment Using Pairs of Light Quanta Produced by Optical Parametric Down Conversion. *Physical Review Letters*, 61(26):2921–2924, December 1988. doi: 10.1103/PhysRevLett.61.2921. URL `https://link.aps.org/doi/10.1103/PhysRevLett.61.2921`.

[123] E. Knill, R. Laflamme, and G. J. Milburn. A scheme for efficient quantum computation with linear optics. *Nature*, 409(6816):46–52, January 2001. ISSN 1476-4687. doi: 10.1038/35051009. URL `https://www.nature.com/articles/35051009`.

[124] Hui Wang, Jian Qin, Xing Ding, Ming-Cheng Chen, Si Chen, Xiang You, Yu-Ming He, Xiao Jiang, L. You, Z. Wang, C. Schneider, Jelmer J. Renema, Sven Höfling, Chao-Yang Lu, and Jian-Wei Pan. Boson Sampling with 20 Input Photons and a 60-Mode Interferometer in a 10^14-Dimensional Hilbert Space. *Physical Review Letters*, 123(25):250503, December 2019. doi: 10.1103/PhysRevLett.123.250503. URL `https://link.aps.org/doi/10.1103/PhysRevLett.123.250503`.

[125] T. Legero, T. Wilk, A. Kuhn, and G. Rempe. Time-resolved two-photon quantum interference. *Applied Physics B*, 77(8):797–802, December 2003. ISSN 0946-2171, 1432-0649. doi: 10.1007/s00340-003-1337-x. URL `http://link.springer.com/10.1007/s00340-003-1337-x`.

[126] Eva Schöll, Lukas Hanschke, Lucas Schweickert, Katharina D. Zeuner, Marcus Reindl, Saimon Filipe Covre da Silva, Thomas Lettner, Rinaldo Trotta, Jonathan J. Finley, Kai Müller, Armando Rastelli, Val Zwiller, and Klaus D. Jöns. Resonance Fluorescence of GaAs Quantum Dots with Near-Unity Photon Indistinguishability. *Nano Letters*, 19(4):2404–2410, April 2019. ISSN 1530-6984. doi: 10.1021/acs.nanolett.8b05132. URL `https://doi.org/10.1021/acs.nanolett.8b05132`.

[127] Benjamin Kambs and Christoph Becher. Limitations on the indistinguishability of photons from remote solid state sources. *New Journal of Physics*, 20(11):115003, November 2018. ISSN 1367-2630. doi: 10.1088/1367-2630/aaea99. URL `http://stacks.iop.org/1367-2630/20/i=11/a=115003?key=crossref.34fae91195a6bad0de3c65be7c9458a0`.

[128] A. Kiraz, M. Atatüre, and A. Imamoğlu. Quantum-dot single-photon sources: Prospects for applications in linear optics quantum-information processing. *Physical Review A*, 69(3):032305, March 2004. doi: 10.1103/PhysRevA.69.032305. URL `https://link.aps.org/doi/10.1103/PhysRevA.69.032305`.

[129] Emil V. Denning, Jake Iles-Smith, Niels Gregersen, and Jesper Mork. Phonon effects in quantum dot single-photon sources. *Optical Materials Express*, 10(1):222–239, January 2020. ISSN 2159-3930. doi: 10.1364/OME.380601. URL `https://www.osapublishing.org/ome/abstract.cfm?uri=ome-10-1-222`.

[130] Andreas V. Kuhlmann, Julien Houel, Arne Ludwig, Lukas Greuter, Dirk Reuter, Andreas D. Wieck, Martino Poggio, and Richard J. Warburton. Charge noise and spin noise in a semiconductor quantum device. *Nature Physics*, 9(9):570–575, September 2013. ISSN 1745-2473, 1745-2481. doi: 10.1038/nphys2688. URL `http://www.nature.com/articles/nphys2688`.

[131] Hüseyin Vural, Simone L. Portalupi, and Peter Michler. Perspective of self-assembled InGaAs quantum-dots for multi-source quantum implementations. *Applied Physics Letters*, 117(3): 030501, July 2020. ISSN 0003-6951. doi: 10.1063/5.0010782. URL `https://aip.scitation.org/doi/full/10.1063/5.0010782`.

[132] Eva Schöll, Lucas Schweickert, Lukas Hanschke, Katharina D. Zeuner, Friedrich Sbresny, Thomas Lettner, Rahul Trivedi, Marcus Reindl, Saimon Filipe Covre da Silva, Rinaldo Trotta, Jonathan J. Finley, Jelena Vučković, Kai Müller, Armando Rastelli, Val Zwiller, and Klaus D. Jöns. Crux of Using the Cascaded Emission of a Three-Level Quantum Ladder System to Generate Indistinguishable Photons. *Physical Review Letters*, 125(23):233605, December 2020. ISSN 0031-9007, 1079-7114. doi: 10.1103/PhysRevLett.125.233605. URL `https://link.aps.org/doi/10.1103/PhysRevLett.125.233605`.

[133] A. J. Bennett, D. C. Unitt, A. J. Shields, P. Atkinson, and D. A. Ritchie. Influence of exciton dynamics on the interference of two photons from a microcavity single-photon source. *Optics Express*, 13(20):7772–7778, October 2005. ISSN 1094-4087. doi: 10.1364/OPEX.13.007772. URL `https://www.osapublishing.org/oe/abstract.cfm?uri=oe-13-20-7772`.

[134] S. Ates, S. M. Ulrich, S. Reitzenstein, A. Löffler, A. Forchel, and P. Michler. Post-Selected Indistinguishable Photons from the Resonance Fluorescence of a Single Quantum Dot in a Microcavity. *Physical Review Letters*, 103(16):167402, October 2009. doi: 10.1103/PhysRevLett.103.167402. URL `https://link.aps.org/doi/10.1103/PhysRevLett.103.167402`.

[135] L. Besombes, K. Kheng, L. Marsal, and H. Mariette. Acoustic phonon broadening mechanism in single quantum dot emission. *Physical Review B*, 63(15):155307, March 2001. doi: 10.1103/PhysRevB.63.155307. URL `https://link.aps.org/doi/10.1103/PhysRevB.63.155307`.

[136] Antoine Reigue, Jake Iles-Smith, Fabian Lux, Leonard Monniello, Mathieu Bernard, Florent Margaillan, Aristide Lemaitre, Anthony Martinez, Dara P. S. McCutcheon, Jesper Mork, Richard Hostein, and Valia Voliotis. Probing Electron-Phonon Interaction through Two-Photon Interference in Resonantly Driven Semiconductor Quantum Dots. *Physical Review Letters*, 118(23):233602, June 2017. doi: 10.1103/PhysRevLett.118.233602. URL `https://link.aps.org/doi/10.1103/PhysRevLett.118.233602`.

[137] Jake Iles-Smith, Dara P. S. McCutcheon, Ahsan Nazir, and Jesper Mørk. Phonon scattering inhibits simultaneous near-unity efficiency and indistinguishability in semiconductor single-photon sources. *Nature Photonics*, 11(8):521–526, August 2017. ISSN 1749-4893. doi: 10.1038/nphoton.2017.101. URL `https://www.nature.com/articles/nphoton.2017.101`.

[138] Christian Schimpf, Marcus Reindl, Petr Klenovský, Thomas Fromherz, Saimon F. Covre Da Silva, Julian Hofer, Christian Schneider, Sven Höfling, Rinaldo Trotta, and Armando

Rastelli. Resolving the temporal evolution of line broadening in single quantum emitters. *Optics Express*, 27(24):35290, November 2019. ISSN 1094-4087. doi: 10.1364/OE.27.035290. URL https://www.osapublishing.org/abstract.cfm?URI=oe-27-24-35290.

[139] Liang Zhai, Matthias C. Löbl, Giang N. Nguyen, Julian Ritzmann, Alisa Javadi, Clemens Spinnler, Andreas D. Wieck, Arne Ludwig, and Richard J. Warburton. Low-noise GaAs quantum dots for quantum photonics. *Nature Communications*, 11(1):4745, September 2020. ISSN 2041-1723. doi: 10.1038/s41467-020-18625-z. URL https://www.ncbi.nlm.nih.gov/pmc/articles/PMC7506537/.

[140] A. Thoma, P. Schnauber, M. Gschrey, M. Seifried, J. Wolters, J.-H. Schulze, A. Strittmatter, S. Rodt, A. Carmele, A. Knorr, T. Heindel, and S. Reitzenstein. Exploring Dephasing of a Solid-State Quantum Emitter via Time- and Temperature-Dependent Hong-Ou-Mandel Experiments. *Physical Review Letters*, 116(3):033601, January 2016. doi: 10.1103/PhysRevLett.116.033601. URL https://link.aps.org/doi/10.1103/PhysRevLett.116.033601.

[141] Stephen Gasiorowicz. *Quantum Physics*. Wiley, 3 edition, 2003. ISBN 978-0-471-05700-0.

[142] Reinhard F. Werner. Quantum states with Einstein-Podolsky-Rosen correlations admitting a hidden-variable model. *Physical Review A*, 40(8):4277–4281, October 1989. doi: 10.1103/PhysRevA.40.4277. URL https://link.aps.org/doi/10.1103/PhysRevA.40.4277.

[143] Daniel F. V. James, Paul G. Kwiat, William J. Munro, and Andrew G. White. Measurement of qubits. *Physical Review A*, 64(5):052312, October 2001. ISSN 1050-2947, 1094-1622. doi: 10.1103/PhysRevA.64.052312. URL https://link.aps.org/doi/10.1103/PhysRevA.64.052312.

[144] William K. Wootters. Entanglement of Formation of an Arbitrary State of Two Qubits. *Physical Review Letters*, 80(10):2245–2248, March 1998. ISSN 0031-9007, 1079-7114. doi: 10.1103/PhysRevLett.80.2245. URL https://link.aps.org/doi/10.1103/PhysRevLett.80.2245.

[145] N. Somaschi, V. Giesz, L. De Santis, J. C. Loredo, M. P. Almeida, G. Hornecker, S. L. Portalupi, T. Grange, C. Antón, J. Demory, C. Gómez, I. Sagnes, N. D. Lanzillotti-Kimura, A. Lemaítre, A. Auffeves, A. G. White, L. Lanco, and P. Senellart. Near-optimal single-photon sources in the solid state. *Nature Photonics*, 10(5):340–345, May 2016. ISSN 1749-4885, 1749-4893. doi: 10.1038/nphoton.2016.23. URL http://www.nature.com/articles/nphoton.2016.23.

[146] Stephanie Wehner, David Elkouss, and Ronald Hanson. Quantum internet: A vision for the road ahead. *Science*, 362(6412), October 2018. ISSN 0036-8075, 1095-9203. doi: 10.1126/science.aam9288. URL https://science.sciencemag.org/content/362/6412/eaam9288.

[147] Christian Schimpf, Santanu Manna, Saimon F. Covre da Silva, Maximilian Aigner, and Armando Rastelli. Entanglement-based quantum key distribution with a blinking-free quantum dot operated at a temperature up to 20 K. *Advanced Photonics*, 3(6):065001, December

2021. ISSN 2577-5421, 2577-5421. doi: 10.1117/1.AP.3.6.065001. URL https://www.spiedigitallibrary.org/journals/advanced-photonics/volume-3/issue-6/065001/Entanglement-based-quantum-key-distribution-with-a-blinking-free-quantum/10.1117/1.AP.3.6.065001.full.

[148] Mikołaj Lasota, Radim Filip, and Vladyslav C. Usenko. Sufficiency of quantum non-Gaussianity for discrete-variable quantum key distribution over noisy channels. *Physical Review A*, 96(1):012301, July 2017. ISSN 2469-9926, 2469-9934. doi: 10.1103/PhysRevA.96.012301. URL http://link.aps.org/doi/10.1103/PhysRevA.96.012301.

[149] Christian Schimpf, Marcus Reindl, Daniel Huber, Barbara Lehner, Saimon F. Covre Da Silva, Santanu Manna, Michal Vyvlecka, Philip Walther, and Armando Rastelli. Quantum cryptography with highly entangled photons from semiconductor quantum dots. *Science Advances*, 7(16):eabe8905, April 2021. ISSN 2375-2548. doi: 10.1126/sciadv.abe8905. URL https://advances.sciencemag.org/content/7/16/eabe8905.

[150] R. M. Stevenson, J. Nilsson, A. J. Bennett, J. Skiba-Szymanska, I. Farrer, D. A. Ritchie, and A. J. Shields. Quantum teleportation of laser-generated photons with an entangled-light-emitting diode. *Nature Communications*, 4(1):2859, December 2013. ISSN 2041-1723. doi: 10.1038/ncomms3859. URL https://www.nature.com/articles/ncomms3859.

[151] Michele B. Rota, Francesco Basso Basset, Davide Tedeschi, and Rinaldo Trotta. Entanglement Teleportation With Photons From Quantum Dots: Toward a Solid-State Based Quantum Network. *IEEE Journal of Selected Topics in Quantum Electronics*, 26(3):1–16, May 2020. ISSN 1558-4542. doi: 10.1109/JSTQE.2020.2985285. Conference Name: IEEE Journal of Selected Topics in Quantum Electronics.

[152] E. A. Chekhovich, M. N. Makhonin, A. I. Tartakovskii, A. Yacoby, H. Bluhm, K. C. Nowack, and L. M. K. Vandersypen. Nuclear spin effects in semiconductor quantum dots. *Nature Materials*, 12(6):494–504, June 2013. ISSN 1476-4660. doi: 10.1038/nmat3652. URL https://www.nature.com/articles/nmat3652.

[153] Daniel Huber, Barbara Ursula Lehner, Diana Csontosová, Marcus Reindl, Simon Schuler, Saimon Filipe Covre da Silva, Petr Klenovský, and Armando Rastelli. Single-particle-picture breakdown in laterally weakly confining GaAs quantum dots. *Physical Review B*, 100(23):235425, December 2019. doi: 10.1103/PhysRevB.100.235425. URL https://link.aps.org/doi/10.1103/PhysRevB.100.235425.

[154] Christian Schimpf, Marcus Reindl, Francesco Basso Basset, Klaus D. Jöns, Rinaldo Trotta, and Armando Rastelli. Quantum dots as potential sources of strongly entangled photons: Perspectives and challenges for applications in quantum networks. *Applied Physics Letters*, 118(10):100502, March 2021. ISSN 0003-6951. doi: 10.1063/5.0038729. URL https://aip.scitation.org/doi/10.1063/5.0038729.

[155] Kevin A Fischer, Lukas Hanschke, Malte Kremser, Jonathan J Finley, Kai Müller, and Jelena Vučković. Pulsed Rabi oscillations in quantum two-level systems: beyond the area

theorem. *Quantum Science and Technology*, 3(1):014006, January 2018. ISSN 2058-9565. doi: 10.1088/2058-9565/aa9269. URL https://iopscience.iop.org/article/10.1088/2058-9565/aa9269.

[156] Tim Seidelmann, Christian Schimpf, Thomas K. Bracht, Michael Cosacchi, Alexei Vagov, Armando Rastelli, Doris E. Reiter, and Vollrath Martin Axt. Two-Photon Excitation Sets Fundamental Limit to Entangled Photon Pair Generation from Quantum Emitters, May 2022. URL http://arxiv.org/abs/2205.03390. arXiv:2205.03390.

[157] Gregor Jundt, Lucio Robledo, Alexander Högele, Stefan Fält, and Atac Imamoğlu. Observation of Dressed Excitonic States in a Single Quantum Dot. *Physical Review Letters*, 100(17):177401, April 2008. doi: 10.1103/PhysRevLett.100.177401. URL https://link.aps.org/doi/10.1103/PhysRevLett.100.177401. Publisher: American Physical Society.

[158] Andreas Muller, Wei Fang, John Lawall, and Glenn S. Solomon. Creating Polarization-Entangled Photon Pairs from a Semiconductor Quantum Dot Using the Optical Stark Effect. *Physical Review Letters*, 103(21):217402, November 2009. doi: 10.1103/PhysRevLett.103.217402. URL https://link.aps.org/doi/10.1103/PhysRevLett.103.217402.

[159] Ana Predojević, Miroslav Ježek, Tobias Huber, Harishankar Jayakumar, Thomas Kauten, Glenn S. Solomon, Radim Filip, and Gregor Weihs. Efficiency vs. multi-photon contribution test for quantum dots. *Optics Express*, 22(4):4789–4798, February 2014. ISSN 1094-4087. doi: 10.1364/OE.22.004789. URL https://opg.optica.org/oe/abstract.cfm?uri=oe-22-4-4789.

[160] Adrien Dousse, Jan Suffczyński, Alexios Beveratos, Olivier Krebs, Aristide Lemaître, Isabelle Sagnes, Jacqueline Bloch, Paul Voisin, and Pascale Senellart. Ultrabright source of entangled photon pairs. *Nature*, 466(7303):217–220, July 2010. ISSN 0028-0836, 1476-4687. doi: 10.1038/nature09148. URL http://www.nature.com/articles/nature09148.

[161] Jonathan R. A. Müller, R. Mark Stevenson, Joanna Skiba-Szymanska, Ginny Shooter, Jan Huwer, Ian Farrer, David A. Ritchie, and Andrew J. Shields. Active reset of a radiative cascade for entangled-photon generation beyond the continuous-driving limit. *Physical Review Research*, 2(4):043292, November 2020. doi: 10.1103/PhysRevResearch.2.043292. URL https://link.aps.org/doi/10.1103/PhysRevResearch.2.043292.

[162] A. Fognini, A. Ahmadi, M. Zeeshan, J. T. Fokkens, S. J. Gibson, N. Sherlekar, S. J. Daley, D. Dalacu, P. J. Poole, K. D. Jöns, V. Zwiller, and M. E. Reimer. Dephasing Free Photon Entanglement with a Quantum Dot. *ACS Photonics*, 6(7):1656–1663, July 2019. ISSN 2330-4022, 2330-4022. doi: 10.1021/acsphotonics.8b01496. URL http://pubs.acs.org/doi/10.1021/acsphotonics.8b01496.

[163] Hai Son Nguyen, Gregory Sallen, Marco Abbarchi, Robson Ferreira, Christophe Voisin, Philippe Roussignol, Guillaume Cassabois, and Carole Diederichs. Photoneutralization

and slow capture of carriers in quantum dots probed by resonant excitation spectroscopy. *Physical Review B*, 87(11):115305, March 2013. doi: 10.1103/PhysRevB.87.115305. URL https://link.aps.org/doi/10.1103/PhysRevB.87.115305.

[164] Abdul Waris Ziarkash, Siddarth Koduru Joshi, Mario Stipčević, and Rupert Ursin. Comparative study of afterpulsing behavior and models in single photon counting avalanche photo diode detectors. *Scientific Reports*, 8(1):5076, March 2018. ISSN 2045-2322. doi: 10.1038/s41598-018-23398-z. URL https://www.nature.com/articles/s41598-018-23398-z.

[165] Lukas Hanschke, Lucas Schweickert, Juan Camilo López Carreño, Eva Schöll, Katharina D. Zeuner, Thomas Lettner, Eduardo Zubizarreta Casalengua, Marcus Reindl, Saimon Filipe Covre da Silva, Rinaldo Trotta, Jonathan J. Finley, Armando Rastelli, Elena del Valle, Fabrice P. Laussy, Val Zwiller, Kai Müller, and Klaus D. Jöns. Origin of Antibunching in Resonance Fluorescence. *Physical Review Letters*, 125(17):170402, October 2020. doi: 10.1103/PhysRevLett.125.170402. URL https://link.aps.org/doi/10.1103/PhysRevLett.125.170402.

[166] Jan-Philipp Jahn, Mathieu Munsch, Lucas Béguin, Andreas V. Kuhlmann, Martina Renggli, Yongheng Huo, Fei Ding, Rinaldo Trotta, Marcus Reindl, Oliver G. Schmidt, Armando Rastelli, Philipp Treutlein, and Richard J. Warburton. An artificial Rb atom in a semiconductor with lifetime-limited linewidth. *Physical Review B*, 92(24):245439, December 2015. doi: 10.1103/PhysRevB.92.245439. URL https://link.aps.org/doi/10.1103/PhysRevB.92.245439.

[167] T. Kuroda, T. Belhadj, M. Abbarchi, C. Mastrandrea, M. Gurioli, T. Mano, N. Ikeda, Y. Sugimoto, K. Asakawa, N. Koguchi, K. Sakoda, B. Urbaszek, T. Amand, and X. Marie. Bunching visibility for correlated photons from single GaAs quantum dots. *Physical Review B*, 79(3):035330, January 2009. doi: 10.1103/PhysRevB.79.035330. URL https://link.aps.org/doi/10.1103/PhysRevB.79.035330.

[168] Edo Waks, Charles Santori, and Yoshihisa Yamamoto. Security aspects of quantum key distribution with sub-Poisson light. *Physical Review A*, 66(4):042315, October 2002. doi: 10.1103/PhysRevA.66.042315. URL https://link.aps.org/doi/10.1103/PhysRevA.66.042315.

[169] P. Grünwald. Effective second-order correlation function and single-photon detection. *New Journal of Physics*, 21(9):093003, September 2019. ISSN 1367-2630. doi: 10.1088/1367-2630/ab3ae0. URL https://doi.org/10.1088/1367-2630/ab3ae0.

[170] Kevin A. Fischer, Lukas Hanschke, Jakob Wierzbowski, Tobias Simmet, Constantin Dory, Jonathan J. Finley, Jelena Vučković, and Kai Müller. Signatures of two-photon pulses from a quantum two-level system. *Nature Physics*, 13(7):649–654, July 2017. ISSN 1745-2481. doi: 10.1038/nphys4052. URL https://www.nature.com/articles/nphys4052.

[171] Olivier Bouchet, Herve Sizun, Christian Boisrobert, Frederique de Fornel, and Pierre-Noel Favennec. *Free-Space Optics: Propagation and Communication*. 91. John Wiley & Sons, 2010. ISBN 978-0-470-61209-5.

[172] Francesco Basso Basset, Mauro Valeri, Julia Neuwirth, Emanuele Polino, Michele B. Rota, Davide Poderini, Claudio Pardo, Giovanni Rodari, Emanuele Roccia, Saimon F. Covre da Silva, Giuseppe Ronco, Nicolò Spagnolo, Armando Rastelli, Gonzalo Carvacho, Fabio Sciarrino, and Rinaldo Trotta. Daylight entanglement-based quantum key distribution with a quantum dot source, June 2022. URL `http://arxiv.org/abs/2206.15360`. arXiv:2206.15360.

[173] Gilles Brassard and Louis Salvail. Secret-Key Reconciliation by Public Discussion. In Tor Helleseth, editor, *Advances in Cryptology — EUROCRYPT '93*, Lecture Notes in Computer Science, pages 410–423, Berlin, Heidelberg, 1994. Springer. ISBN 978-3-540-48285-7. doi: 10.1007/3-540-48285-7_35.

[174] Vadim Makarov, Andrey Anisimov, and Johannes Skaar. Effects of detector efficiency mismatch on security of quantum cryptosystems. *Physical Review A*, 74(2):022313, August 2006. doi: 10.1103/PhysRevA.74.022313. URL `https://link.aps.org/doi/10.1103/PhysRevA.74.022313`.

[175] Antonio Acín, Serge Massar, and Stefano Pironio. Efficient quantum key distribution secure against no-signalling eavesdroppers. 8(8):126–126, August 2006. ISSN 1367-2630. doi: 10.1088/1367-2630/8/8/126. URL `https://doi.org/10.1088/1367-2630/8/8/126`. Publisher: IOP Publishing.

[176] Jesus Martinez-Mateo, Christoph Pacher, Momtchil Peev, Alex Ciurana, and Vicente Martin. Demystifying the information reconciliation protocol cascade. *Quantum Information & Computation*, 15(5-6):453–477, April 2015. ISSN 1533-7146.

[177] Norbert Lütkenhaus and Mika Jahma. Quantum key distribution with realistic states: photon-number statistics in the photon-number splitting attack. *New Journal of Physics*, 4:44–44, July 2002. ISSN 1367-2630. doi: 10.1088/1367-2630/4/1/344. URL `https://doi.org/10.1088/1367-2630/4/1/344`.

[178] Miloslav Dušek, Ondřej Haderka, and Martin Hendrych. Generalized beam-splitting attack in quantum cryptography with dim coherent states. *Optics Communications*, 169:103–108, October 1999. ISSN 0030-4018. doi: 10.1016/S0030-4018(99)00419-8. URL `https://ui.adsabs.harvard.edu/abs/1999OptCo.169..103D`.

[179] B. Dzurnak, R. M. Stevenson, J. Nilsson, J. F. Dynes, Z. L. Yuan, J. Skiba-Szymanska, I. Farrer, D. A. Ritchie, and A. J. Shields. Quantum key distribution with an entangled light emitting diode. *Applied Physics Letters*, 107(26):261101, December 2015. ISSN 0003-6951. doi: 10.1063/1.4938502. URL `https://aip.scitation.org/doi/abs/10.1063/1.4938502`.

[180] Hua-Ying Liu, Xiao-Hui Tian, Changsheng Gu, Pengfei Fan, Xin Ni, Ran Yang, Ji-Ning Zhang, Mingzhe Hu, Jian Guo, Xun Cao, Xiaopeng Hu, Gang Zhao, Yan-Qing Lu, Yan-Xiao Gong, Zhenda Xie, and Shi-Ning Zhu. Drone-based entanglement distribution towards mobile quantum networks. *National Science Review*, 7(5):921–928, May 2020. ISSN 2095-5138. doi: 10.1093/nsr/nwz227. URL https://doi.org/10.1093/nsr/nwz227.

[181] W. T. Buttler, R. J. Hughes, S. K. Lamoreaux, G. L. Morgan, J. E. Nordholt, and C. G. Peterson. Daylight Quantum Key Distribution over 1.6 km. *Physical Review Letters*, 84(24): 5652–5655, June 2000. doi: 10.1103/PhysRevLett.84.5652. URL https://link.aps.org/doi/10.1103/PhysRevLett.84.5652.

[182] Heasin Ko, Kap-Joong Kim, Joong-Seon Choe, Byung-Seok Choi, Jong-Hoi Kim, Yong-soon Baek, and Chun Ju Youn. Experimental filtering effect on the daylight operation of a free-space quantum key distribution. *Scientific Reports*, 8(1):15315, October 2018. ISSN 2045-2322. doi: 10.1038/s41598-018-33699-y. URL https://www.nature.com/articles/s41598-018-33699-y. Number: 1 Publisher: Nature Publishing Group.

[183] Matthew P. Peloso, Ilja Gerhardt, Caleb Ho, Antía Lamas-Linares, and Christian Kurtsiefer. Daylight operation of a free space, entanglement-based quantum key distribution system. *New Journal of Physics*, 11(4):045007, April 2009. ISSN 1367-2630. doi: 10.1088/1367-2630/11/4/045007. URL https://doi.org/10.1088/1367-2630/11/4/045007.

[184] Thomas Weyrauch and Mikhail A. Vorontsov. Free-space laser communications with adaptive optics: Atmospheric compensation experiments. *Journal of Optical and Fiber Communications Reports*, 1(4):355–379, December 2004. ISSN 1619-8638. doi: 10.1007/s10297-005-0033-5. URL https://doi.org/10.1007/s10297-005-0033-5.

[185] Timm Kupko, Martin von Helversen, Lucas Rickert, Jan-Hindrik Schulze, André Strittmatter, Manuel Gschrey, Sven Rodt, Stephan Reitzenstein, and Tobias Heindel. Tools for the performance optimization of single-photon quantum key distribution. *npj Quantum Information*, 6(1):1–8, March 2020. ISSN 2056-6387. doi: 10.1038/s41534-020-0262-8. URL https://www.nature.com/articles/s41534-020-0262-8.

[186] Klaus D. Timmerhaus and Richard P. Reed. *Cryogenic Engineering*. Springer, 2007.

[187] Charles H. Bennett, Gilles Brassard, Claude Crépeau, Richard Jozsa, Asher Peres, and William K. Wootters. Teleporting an unknown quantum state via dual classical and Einstein-Podolsky-Rosen channels. *Physical Review Letters*, 70(13):1895–1899, March 1993. ISSN 0031-9007. doi: 10.1103/PhysRevLett.70.1895. URL https://link.aps.org/doi/10.1103/PhysRevLett.70.1895.

[188] S. Massar and S. Popescu. Optimal Extraction of Information from Finite Quantum Ensembles. *Physical Review Letters*, 74(8):1259–1263, February 1995. doi: 10.1103/PhysRevLett.74.1259. URL https://link.aps.org/doi/10.1103/PhysRevLett.74.1259.

[189] Seung-Woo Lee and Hyunseok Jeong. Near-deterministic quantum teleportation and resource-efficient quantum computation using linear optics and hybrid qubits. *Physical Review A*, 87 (2):022326, February 2013. doi: 10.1103/PhysRevA.87.022326. URL `https://link.aps.org/doi/10.1103/PhysRevA.87.022326`. Publisher: American Physical Society.

[190] H. F. Chau. Practical scheme to share a secret key through a quantum channel with a 27.6% bit error rate. *Physical Review A*, 66(6):060302, December 2002. doi: 10.1103/PhysRevA.66.060302. URL `https://link.aps.org/doi/10.1103/PhysRevA.66.060302`. Publisher: American Physical Society.

[191] Jin Liu, Kumarasiri Konthasinghe, Marcelo Davanço, John Lawall, Vikas Anant, Varun Verma, Richard Mirin, Sae Woo Nam, Jin Dong Song, Ben Ma, Ze Sheng Chen, Hai Qiao Ni, Zhi Chuan Niu, and Kartik Srinivasan. Single Self-Assembled InAs / GaAs Quantum Dots in Photonic Nanostructures: The Role of Nanofabrication. *Physical Review Applied*, 9(6), June 2018. ISSN 2331-7019. doi: 10.1103/PhysRevApplied.9.064019. URL `https://link.aps.org/doi/10.1103/PhysRevApplied.9.064019`.

[192] Jacob H. Davidson, Pascal Lefebvre, Jun Zhang, Daniel Oblak, and Wolfgang Tittel. Improved light-matter interaction for storage of quantum states of light in a thulium-doped crystal cavity. *Physical Review A*, 101(4):042333, April 2020. doi: 10.1103/PhysRevA.101.042333. URL `https://link.aps.org/doi/10.1103/PhysRevA.101.042333`.